SANDIA REPORT

SAND2015-1197
Unlimited Release
Printed Feb 2015

Equation of State Model Quality Study for Ti and Ti64.

Ann E. Mattsson, Jason Sanchez

Prepared by
Sandia National Laboratories
Albuquerque, New Mexico 87185 and Livermore, California 94550

Sandia National Laboratories is a multi-program laboratory managed and operated by Sandia Corporation,
a wholly owned subsidiary of Lockheed Martin Corporation, for the U.S. Department of Energy's
National Nuclear Security Administration under contract DE-AC04-94AL85000.

Sandia National Laboratories

Issued by Sandia National Laboratories, operated for the United States Department of Energy by Sandia Corporation.

Available to DOE and DOE contractors from
U.S. Department of Energy
Office of Scientific and Technical Information
P.O. Box 62
Oak Ridge, TN 37831

Telephone: (865) 576-8401
Facsimile: (865) 576-5728
E-Mail: reports@adonis.osti.gov
Online ordering: http://www.osti.gov/bridge

Available to the public from
U.S. Department of Commerce
National Technical Information Service
5285 Port Royal Rd
Springfield, VA 22161

Telephone: (800) 553-6847
Facsimile: (703) 605-6900
E-Mail: orders@ntis.fedworld.gov
Online ordering: http://www.ntis.gov/help/ordermethods.asp?loc=7-4-0#online

SAND2015-1197
Unlimited Release
Printed Feb 2015

Equation of State Model Quality Study for Ti and Ti64.

Ann E. Mattsson
Multiscale Science MS 1322
Sandia National Laboratories
P.O. Box 5800, Albuquerque, NM 87185-1322
aematts@sandia.gov

Jason Sanchez
Computational Multiphysics MS 1323
Sandia National Laboratories
P.O. Box 5800, Albuquerque, NM 87185-1323
jassanc@sandia.gov

Abstract

Titanium and the titanium alloy Ti64 (6% aluminum, 4% vanadium and the balance titanium) are materials used in many technologically important applications. To be able to computationally investigate and design these applications, accurate Equations of State (EOS) are needed and in many cases also additional constitutive relations. This report describes what data is available for constructing EOS for these two materials, and also describes some references giving data for stress-strain constitutive models. We also give some suggestions for projects to achieve improved EOS and constitutive models.

In an appendix, we present a study of the 'cloud formation' issue observed in the ALEGRA code. This issue was one of the motivating factors for this literature search of available data for constructing improved EOS for Ti and Ti64. However, the study shows that the cloud formation issue is only marginally connected to the quality of the EOS, and, in fact, is a physical behavior of the system in question. We give some suggestions for settings in, and improvements of, the ALEGRA code to address this computational difficulty.

Acknowledgment

Funding for this research was provided by the Army Research Laboratory and is gratefully acknowledged. Sandia National Laboratories is a multi-program laboratory managed and operated by Sandia Corporation, a wholly owned subsidiary of Lockheed Martin Corporation, for the U.S. Department of Energy's National Nuclear Security Administration under contract DE-AC04-94AL85000.

Contents

Appendix

List of Figures

Nomenclature

Ti Titanium. An elemental metal composed of titanium atoms (atomic number 22).

Ti64 A titanium alloy nominally composed of 6% aluminum, 4% vanadium, and 90% titanium, by weight.

EOS Equation of State. A relation providing pressure and internal energy as a function of density and temperature.

Sesame A format for tabular EOS information.[32] At a minimum the Internal Energy and the Pressure is tabulated on a rectangular grid of density and temperature.

ALEGRA The Arbitrary-Lagrangian-Eulerian General Research Applications (ALEGRA) code is a large-deformation shock physics code created by researchers at Sandia National Laboratory.

CTH CTH is a multi-material, Eulerian, large-deformation, strong shock wave, solid mechanics code developed at Sandia National Laboratories.

Hugoniot The collection of points in thermodynamic phase space describing the final states achievable by a shock from a specific initial state. The principal Hugoniot is the Hugoniot from the ambient state. Secondary Hugoniots can be obtained from preshocked states.

HEL Hugoniot Elastic Limit. The state on the Hugoniot above which a shock results in plastic deformation.

Force Fracture An algorithmic option used in ALEGRA's void insertion computational material failure method. Use of the force fracture option imposes a lower bound for material density by inserting empty volume (void material) into a discrete finite element containing the material of interest in order to maintain the lower density bound for a given material volume fraction. The insertion of empty space effectively causes fracture of the solid material.

Quantum Mechanics The most fundamental and precise theory of matter that we know of. The theory of quantum particles, such as electrons and other elementary particles.

Quantum particle While the total energy of classical particles (composed of very many elementary particles) can be distributed continuously, the total energy of quantum particles is quantized. There are two types of quantum particles, fermions, such as electrons, and bosons, such as the Helium-4 atoms. While all bosons in a collection of bosons can have the same energy and form a Bose condensate, such as Helium-4 when it is superfluid, fermions in a collection of fermions, such as in a metal, need to all have different energies.

FD Fermi-Dirac statistics: The equilibrium distribution of energies in a collection of fermions at a certain temperature. This distribution is determining many of the properties of materials.

Dirac The Dirac Equation: The relativistic quantum mechanical wave equation necessary to accurately describe the electrons in heavy materials like actinides.

SE The Schrödinger Equation: The non-relativistic limit of the Dirac Equation, sufficiently accurate to describe electrons in lighter materials.

DFT Density Functional Theory: The formally exact reformulation of the wave-function based Shrödinger and Dirac Equations in terms of density and currents.[20]

KS The Kohn-Sham Equations: A calculational approach derived from the Dirac/SE using DFT. These are the equations implemented in DFT codes.[24]

Functional A short name for an approximation for the Exchange-Correlation functional which is the only part of DFT that needs to be approximated. The functional sets the possible accuracy of DFT calculations.

LMTO Linear Muffin Tin Orbital: A calculational method used in the RSPt code (see below).

LAPW Linear Augmented Plane Wave: Another calculational method. It is considered the implementation method that gives the most accurate DFT results. Other methods are usually verified against this method.

plane-wave code A code using plane waves as a basis set. This is the computationally most effective approach because Fourier Transforms can be used. Calculations can also be systematically improved by increasing the number of basis functions used, usually specified by the so called "cut-off". However, describing core electrons accurately requires a very large cut-off, leading to expensive calculations. The plane-wave approach thus is mostly used together with pseudo-potentials (see below).

all-electron code A code treating all electrons explicitly. LMTO and LAPW codes are all-electron.

pseudo-potential code The chemically inert core electrons are treated in a collective way via pseudo potentials, which increases the computational efficiency considerably. A number of different approaches exist; all are verified by comparing to all-electron, usually LAPW, results.

PAW Projected Augmented Wave: The pseudo potential technique currently considered the most accurate.[5,28]

RSPt Relativistic Spin-Polarized test: The name of an all-electron, full potential, LMTO code developed by Dr. John M. Wills at Los Alamos National Laboratory.[1,55]

VASP Vienna *Ab-initio* Simulation Package: A plane wave, pseudo potential (PAW), DFT code.[25–27]

core electron An electron close to the nucleus. In an LMTO or LAPW treatment these electrons are considered inert and their properties only depend on the closest nuclei. In a pseudo-potential code the effect of the core electrons on the valence electrons is included via pseudo potentials.

semi-core electron An electron that is intermediate between a core and a valence electron. It has the same angular momentum quantum number as some of the valence electrons but has a lower principal quantum number (it is in a lower shell). For the heavier nuclei (or for lighter nuclei at high pressure) these electrons need to be treated as valence electrons.

valence electron The outermost electrons are valence electrons and their properties are dependent on many nuclei. These electrons are forming bonds that hold a solid or molecule together.

Chapter 1

Introduction and Motivation

The increasing use of modeling and simulation as an additional source of information to experimental work, for investigating and analyzing real world scenarios, not only requires good engineering codes that are thoroughly verified to obey appropriate conservation laws, but also require accurate descriptions of the materials involved in the calculations. The materials are each described by a number of constitutive relations and an equation of state (EOS). This report deals mainly with information needed for constructing EOS's for titanium and a titanium alloy.

The "cloud formation" issue that was one of the motivating factors for this work is studied in the Appendices. While it is shown that this specific computational issue is only loosely related to the quality of the EOS, a good quality EOS is still crucial for enabling reliable computational predictions.

An EOS is an equation describing the equilibrium state of a material. It commonly gives the pressure and internal energy as a function of density and temperature and can be delivered to the code as analytical equations or as tables. For certain applications, specifically for pure shock problems, a full EOS is not needed but an incomplete EOS giving the pressure as a function of density and internal energy is sufficient, as the Rankine-Hugoniot "jump conditions", the conservation laws governing the shock physics, do not involve temperature.

In constructing an EOS it is important to understand that the pressure, P, and the specific internal energy, E, are not independent. The fundamental thermodynamic relation derived from the first and second laws of thermodynamics is

$$dE = -PdV + TdS \ , \tag{1.1}$$

where V is the specific volume and S is the specific entropy. Writing

$$E = E(V, S) \ , \tag{1.2}$$

we see that the pressure and temperature are partial derivatives of this quantity with respect to one variable, holding the other fixed :

$$-P(V,S) = \left.\frac{\partial E(V,S)}{\partial V}\right|_S , \quad \text{and} \quad T(V,S) = \left.\frac{\partial E(V,S)}{\partial S}\right|_V \ . \tag{1.3}$$

Thus, the pressure is the derivative of the internal energy with respect to volume *along an isentrope*. However, codes usually are not equipped to use the entropy, so it is traded for temperature, T, and the energy and pressure are given as separate quantities.

In summary, it is customary to use four quantities in the code, E, P, V, and T, where only three are needed. We then have to make sure that these four quantities are *thermodynamically consistent* with each other. We need an equation relating E and P in terms of only T and V. The natural quantity to use in this case is the *Helmholtz free energy*,

$$H(V,T) = E - TS \ . \tag{1.4}$$

Differentiating this equation and using the fundamental relation in Equation 1.1 gives

$$dH = dE - TdS - SdT = -PdV - SdT \ , \tag{1.5}$$

confirming that the natural variables for the Helmholtz free energy are V and T. Similarly as above we see that

$$-P(V,T) = \left.\frac{\partial H(V,T)}{\partial V}\right|_T , \quad \text{and} \quad -S(V,T) = \left.\frac{\partial H(V,T)}{\partial T}\right|_V \ . \tag{1.6}$$

Differentiating one more time gives us

$$\frac{\partial^2 H}{\partial V \partial T} = -\left.\frac{\partial P(V,T)}{\partial T}\right|_V = -\left.\frac{\partial S(V,T)}{\partial V}\right|_T \ . \tag{1.7}$$

We now have the equations we need to arrive at a consistency relation between E, P, V, and T. Using the definition of H (Equation 1.4) together with the pressure formula in Equation 1.6 gives us

$$-P = \left.\frac{\partial E}{\partial V}\right|_T - T\left.\frac{\partial S}{\partial V}\right|_T \ . \tag{1.8}$$

Using Equation 1.7 and rearranging we arrive at

$$\left.\frac{\partial E}{\partial V}\right|_T = T\left.\frac{\partial P}{\partial T}\right|_V - P \ , \tag{1.9}$$

an equation that needs to be fulfilled if pressure and energy are given as separate quantities. Thermodynamic inconsistency is a common problem when interpolating in EOS tables given on a coarse density-temperature grid.

There are several methods for constructing an EOS. They fall in a range best described by how data (experimental or obtained from calculations) is used. At one end of the spectrum, a full EOS is constructed and then verified using the data. At the other end of the spectrum is using a set of equations with parameters, a *model*, and finding the best fit to all data available. The model is usually derived from fundamental physics by making approximations that might or might not be valid in the final situation where it is used. A multiphase model usually consists of many different sub models describing different parts of the density-temperature phase space, for example, liquid and solid models. The model can describe a class of materials by different values of the *parameters*. The model is usually similar to the EOS derived without fitting, and the main difference depends on whether the parameters are determined from physical principles or fitting. In a multiphase EOS the additional element of phase boundaries is present, and this can also be handled in several different ways.

For the last decade, at Sandia, we have worked mainly in the fitting part of the EOS construction spectrum. We see the parameters in the model as *effective parameters* that represent not only the refined physics described by the simplified model derived by well controlled but severe approximations, but also some, uncontrolled, environmental effects, such as material defects and grain size. These uncontrolled effects introduce statistics into the EOS construction and we have for the last several years developed a scheme for including this *uncertainty* information into the EOS tables we construct. In this work it has also been confirmed that the table resolution not only plays into the thermodynamic consistency described above but also that the errors introduced when going from the analytical model to a table can completely obscure the true statistical uncertainty in the model parameters in many parts of the phase space.

In summary, in our method of EOS construction data is a crucial component, and gathering of this data is an important first step in the EOS construction, see Figure 1.1.

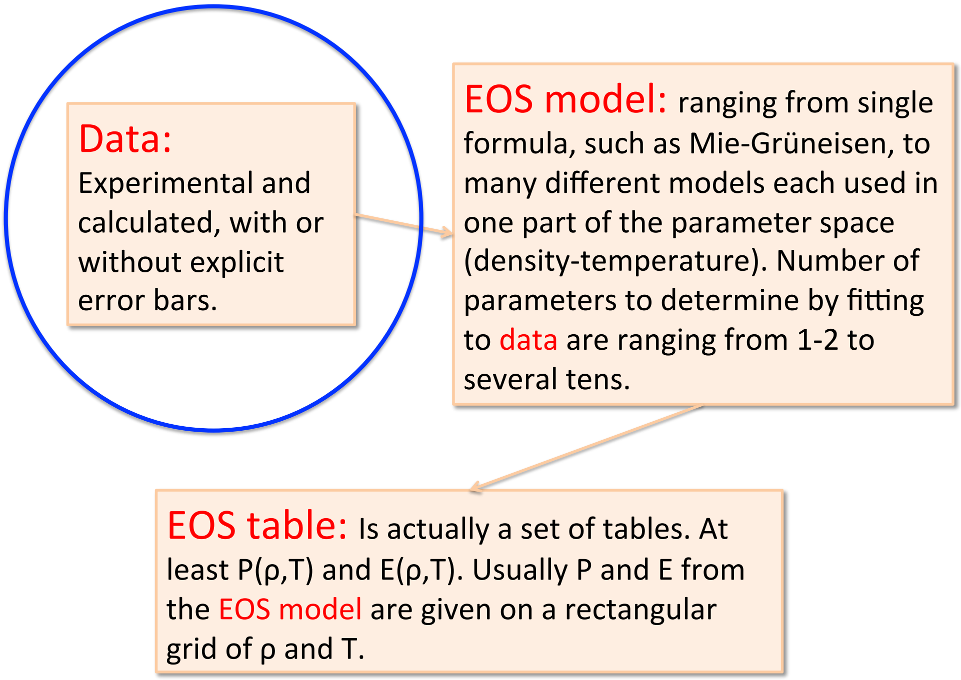

Data: Experimental and calculated, with or without explicit error bars.

EOS model: ranging from single formula, such as Mie-Grüneisen, to many different models each used in one part of the parameter space (density-temperature). Number of parameters to determine by fitting to data are ranging from 1-2 to several tens.

EOS table: Is actually a set of tables. At least P(ρ,T) and E(ρ,T). Usually P and E from the EOS model are given on a rectangular grid of ρ and T.

Figure 1.1. The first step in creating a new EOS table is to gather data.

Chapter 2

Overview

Titanium, Ti, and the Ti alloy, Ti64, composed of 90% Ti, 6% aluminum, Al, and 4% vanadium, V, by weight, are so called *d*-electron materials. The macroscopic manifestation of this type of electronic structure is a rich phase diagram with several solid phases, as illustrated with the phase diagram of pure Ti by Kerley[23] in Figure 2.1.

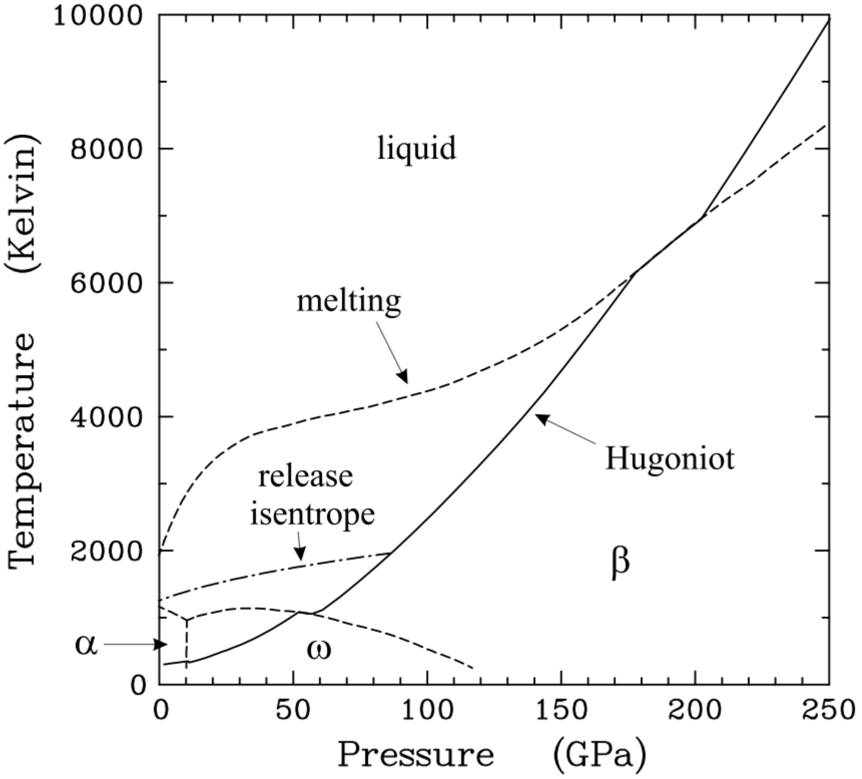

Figure 2.1. The phase diagram for pure Ti by Kerley[23] illustrating the many solid phases usually obtained in *d*-electron materials. For Ti two more phases at high pressure have been identified, the γ and δ phases.

While any reliable data is useful for the subsequent fitting procedure, see Figure 1.1, much of the focus of experiments and calculations for Ti and Ti64 has been on these solid state phase boundaries. Since most types of calculational methods, in particular so called *first principles* methods, are unable to treat alloys with their usual accuracy, much of the understanding of the phase diagram is based on studies of pure Ti.

There are a few indisputable facts about Ti: At ambient pressure, it is transformed from the room temperature stable α phase to the β phase at around 1155K and it is melting at 1941K. The α phase is in the hexagonal close packed (hcp) crystal structure, the β phase is body-centered cubic (bcc), and the ω phase is in a distorted hexagonal structure. The ω phase does not exist in Ti64, at least not at pressures on the principal Hugoniot.

In the following we will give the essential conclusions from each of the references in the reference list.

Chapter 3

Summary of references

Ti Multi-Phase Wide-range EOS (including liquid phase)

Kerley (2003): Reference 23

Reference 23: This work describes the construction of the Ti and Ti64 tables (Sesame tables numbered 2970 and 4061, respectively) currently in use in ALEGRA and CTH. No new data is presented. This publication can be seen as an opinion on which data is valid and which physics mechanisms are important. We will discuss another opinion in the next section.

The main points to note are:

- Based on arguments in Reference 2, Kerley is enforcing the appearance of the β-phase at high pressure and low temperature in Ti, even though a direct phase transition from ω to β (see Figure 2.1) has not been observed experimentally under these conditions. His argument is based on the existence of this phase transition in the similar metals zirconium and hafnium and that two high pressure intermediate phases δ (distorted hcp) and γ (distorted bcc) have been observed.[3]
- He is ignoring the two intermediate high pressure phases.
- His Ti EOS gives reasonable agreement to available data with the exception of isobaric expansion data for liquid at 0.3 GPa.
- Both the resulting Ti and Ti64 EOSs exhibit a so called *plasma phase transition* (PPT), see Figure 3.1. This is a feature that has never been demonstrated in any metal.

Pecker *et al.* (2005): Reference 43

Reference 43: This reference gives a completely different opinion on the EOS and phase diagram of Ti compared to the above presented Kerley view.

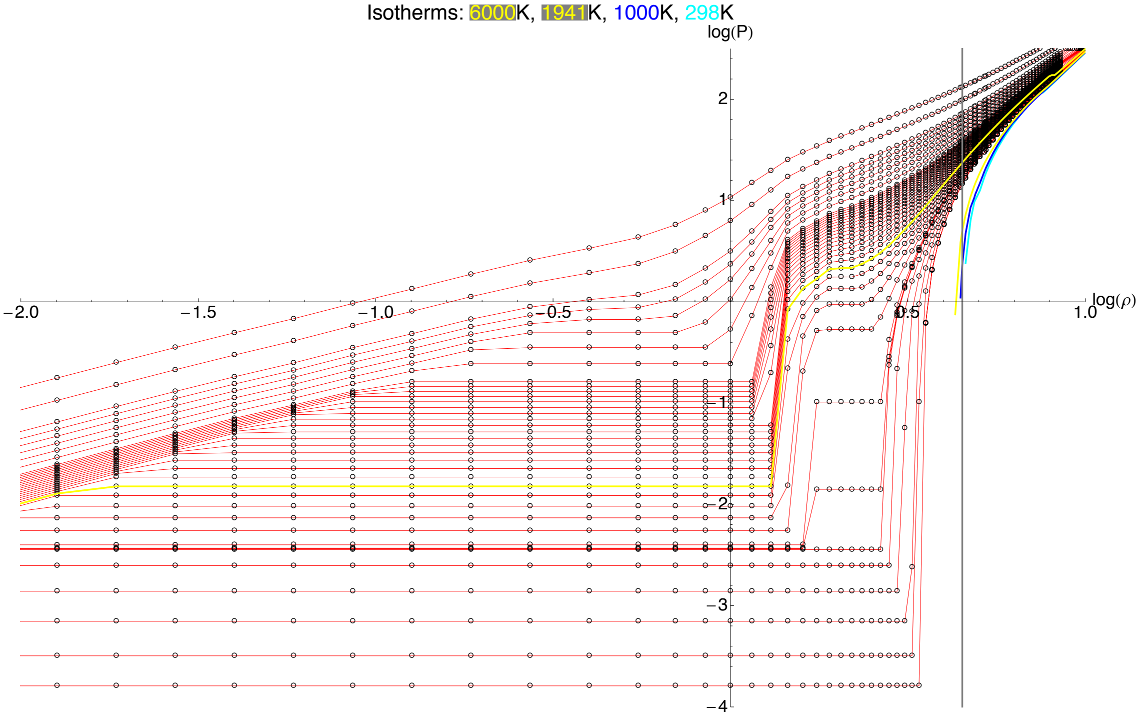

Figure 3.1. Isotherms in log density versus log pressure for Ti Sesame table 2970 (based on the Kerley model), showing the plasma phase transition to the right and the vapor dome to the left.

The main differences are:

- This phase diagram does not have the β phase at high pressures and low temperatures.
- The main differences are in the $\omega \to \beta$ phase transition and in the melting line. This melting line is based on data from Reference 13, data that has been in doubt and still is.
- This EOS gives as reasonable agreement to available data as the Kerley Ti EOS discussed above does.
- This EOS does not have the PPT.

Cox (2012): Reference 10

This Ti EOS is described later in this document. Its phase diagram is depicted in Figure 3.3.

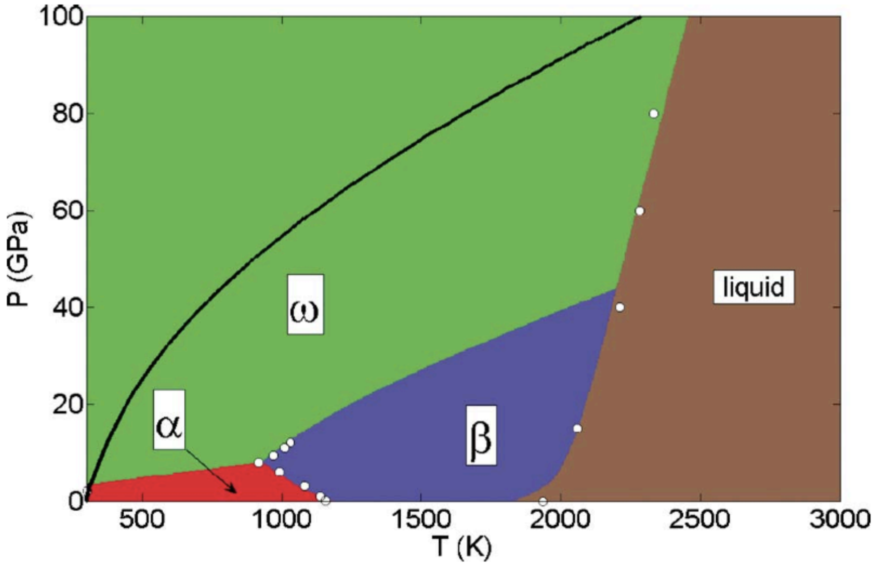

Figure 3.2. The phase diagram for pure Ti by Pecker *et al.*[43] Note that the axes are reversed compared to those in Figure 2.1. The black line is the principal Hugoniot.

Other Ti EOS

Greeff, Trinkle, and Albers (2001): Reference 15

This is the first of a series of papers by Trinkle and others, ending with Reference 19 below. See `https://dtrinkle.matse.illinois.edu/research:ti` Table I gives parameters, determined from fitting, for the free Helmholtz energy of the α and ω phases. Some comparison is made to DFT data calculated with PBE with the WIEN97 code. There is a good discussion on what choices were made and what was prioritized.

Ti experiment (sometimes with DFT calculations)

Errandonea *et al.* (2001): Reference 13

Reference 13 reports high-pressure measurements (laser-heated diamond anvil cell) for the melting curve of Ti (and other metals) in their Figure 2. These are the points on the melting line in Figure 3.2. They state: Ti, at room temperature, is known to undergo a first order transition from bcc (sic) to the ω phase at 8 GPa. The ω phase has a hexagonal lattice and remains stable to 87 GPa. The melting curve shows no indication of a phase transition. (We suspect that bcc should be hcp in this statement, see Figures 2.1 and 3.2). They also state that Ti is hcp at room temperature, but melts from bcc, which is consistent with both Figures 2.1 and 3.2 at low pressure.

The melting line data from this reference is well known to be in doubt. It is suspected to be too flat in temperature.

Errandonea *et al.* (2005): Reference 12

Reference 12 reports on a systematic study of the effects of uniaxial stress on the $\alpha \rightarrow \omega$ transition. They use different pressure media in order to study the effect of uniaxial stress on the outcome of experiments. The study seems motivated both by the effects of short term laser-heating (probably as a response to criticism of their data presented in Reference 13) and Diamond Anvil Cell (DAC) measurements of high-pressure phase transitions.

This reference should be tracked in more recent publications to investigate the status of the controversy of the DAC data at high temperature and pressure.

Zhang *et al.* PRB (2008): Reference 57

This reference provides DAC pressure-volume-temperature data for Ti. Pressures up to 8.2 GPa and temperatures up to 900K. As seen in Figure 2.1, this covers mostly the α phase, but this article also discusses the ω phase that is meta-stable in this region.

Some discussion on the issue of non hydrostatic pressure in DAC experiments.

This article also provides some high temperature unit cell volumes and c/a ratios (ratio between two different side length of the unit cell) that can serve as validation of calculational schemes, in particular the exchange-correlation functional in DFT.

Zhang *et al.* JPCS (2008): Reference 58

Reference 58 is probably mostly based on the same data as in Reference 57: The phase transformations of titanium metal have been studied at temperatures and pressures up to 973K and 8.7GPa. The focus in this article is on the region around the triple point of the α, β, and ω phases. Their Figure 6 gives a nice overview. They also discuss coexistence of α and ω phases and hysteresis.

Vohra and Spencer (2001): Reference 54

The room temperature DAC experiments detecting the γ phase for the first time. Pressure-volume curve at room temperature up to 146 GPa in Figure 3.

Akahama *et al.* (2001): Reference 3

Room temperature DAC experiments. The hcp (α) phase of Ti was transformed into the hexagonal (ω) phase with an initial compression to 7.4 GPa. The ω phase was stable up to 124 GPa. At 128 GPa, the ω phase was transformed into the high-pressure phase (γ-Ti). The second transition was completed at 130 GPa. On further loading to 140 GPa, the intermediate γ phase was transformed to a new high-pressure phase. The transition was also completed at 145 GPa. The highest-pressure phase (δ), with increasing pressure, was stable up to 216 GPa, which is the maximum pressure in the present experiments.

In this reference are also given some lattice constants at high pressure that can serve as validation for computational methods, in particular the exchange-correlation functional in DFT.

Cerrata *et al.* (2006): Reference 7

Describe room temperature ($T = 298$ K) shock and reshock experiments and their influence on the micro structure/local composition as determined by TEM and x-ray and neutron scattering.

Quoting: “The purpose of the present study is twofold: (1) to systematically investigate the effects of interstitial oxygen on the α to ω-phase transition in Ti while holding pulse duration and microstructure relatively constant and (2) to examine the influence of omega phase and peak shock stress on the post- shock reload response of high purity and commercial purity Ti.”

This paper contains a very useful discussion section about how the crystallographic structure of Ti leads to very different behavior of the pure Ti and Ti containing oxygen (alloy). This connection between pure and alloyed Ti is needed in order to be able to do a DFT-based EOS for Ti64.

All discussions are based on defects (twinning) and polycrystalline materials. This reference can provide a lot of help in how to bridge between pure single crystal properties that can be calculated and the real material. However, the usefulness is probably limited to the solid phases.

They give Debye temperatures for the α and ω phases.

Andriot *et al.* (1994): Reference 4

Gives four Hugoniot points for Ti, see below under Ti64.

Ti with DFT and/or other calculations

Sikka *et al.* (1982): Reference 49

EVERYTHING about the ω phase. Presents some early calculations on the band structure but give no direct data that has not been improved or repeated in later publications. However, in order to understand differences between Ti and Ti64 this publications should be studied more closely. Articles by Trinkle *et al.* mentioned in Reference 19 should also be studied for their view on the pathway of the $\alpha \rightarrow \omega$ transition.

Wills group (1993): Reference 2

The authors state "We have studied the crystal structures of Ti, Zr, and Hf under pressure by means of first-principles, total-energy calculations. The three metals are shown to exhibit a crystal structure sequence hcp $\rightarrow \omega \rightarrow$ bcc, with increasing pressure."

This is the main theoretical reference regarding Ti. Even though the DFT calculations would benefit from being redone with the more sophisticated codes and exchange-correlation functionals available today, the theoretical discussion and insights are still very much valid. The qualitative results are still valid while the quantitative results need to be re-evaluated.

Verma *et al.* (2007): Reference 53

The abstract says it all: "We investigate through first-principles calculations the controversial observation of the high-pressure orthorhombic (γ and δ) phases of titanium. Our calculations predict the transition sequence $\omega \rightarrow \gamma \rightarrow \beta$ under pressure, and reveal that the δ phase is elastically unstable under isotropic compression. We attribute its observation to non-hydrostatic stresses present in the diamond-anvil cell experiments. We find the γ phase to be stable in the 102-112 GPa pressure range, with the upper limit of this pressure range increasing under non-hydrostatic conditions."

Again it is noted that non-hydrostatic conditions in DAC experiments might be a problem: "– especially as it is argued that non-hydrostatic conditions in the experiments hinder the observation of the β structure."

However, even though the calculations are performed with a good code (WIEN2K) the choice of functional (PBE) is not optimal for high pressure. But more importantly, the calculations are performed at 0K temperature and might not be representative of results of experiments performed at non-zero temperature. Again, general trends captured with these calculations can probably be trusted but not the quantitative details.

Hu *et al.* (2010): Reference 21

Presents extensive 0 K, static, DFT calculations, combined with the quasi harmonic approximation from phonon spectra calculated by DFT, and the Debye model, for thermal effects. They might do some static calculations with thermal electrons (Fermi-Dirac distributed). They show a phase diagram in their Figure 7, that more supports Kerley[23] than Pecker *et al.*,[43] with a phase boundary between the ω and β phases almost independent of temperature (compare Figures 2.1 and 3.2). They calculate properties in the range $0 - 1500$ K and $0 - 20$ GPa. They obtain the ω phase as the stable phase at 0 K and 0 GPa. "The phase transition ω-Ti $\rightarrow$ α-Ti $\rightarrow$ β-Ti at zero pressure occurs at 146 K and 1143 K, respectively. The predicted triple point is at 9.78 GPa, 931 K." They calculate bulk moduli and pressure derivatives as function of temperature and pressure, they give Thermal pressure and Entropy as well, and they give $P - V - T$ relations.

The DFT calculations are made with the VASP code with a 12 electron PAW potential. The PBE exchange-correlation functional is used, which is not optimal. But the other settings seem to be adequate. If we would perform DFT calculations for Ti, we would redo some of the calculations in this paper to verify their results and to check how another functional and/or PAW potential would compare.

They reference their older work (Reference 17) as a precursor to this work. See important additional comments there.

Hao *et al.* (2008): Reference 17

DFT calculations at $T = 0$ K, PBE VASP 4-electrons PAW. Probably not good enough for high pressure, needs to be checked. Calculate $\omega \rightarrow \gamma \rightarrow \delta \rightarrow \beta$ transitions at $T = 0$ K, but I am not sure of the quality of those because of the PAW. Use the Debye model for ion thermal term. Show a $\alpha \rightarrow \omega$ phase diagram in Figure 5 substantially different from Figure 7 above,[21] which makes me doubt both... Both are made with $T = 0$ K DFT with the Debye model on top. Might need to check this out more before believing in the calculations in Reference 21.

Mei *et al.* (2009): Reference 36

More or less the same as Reference 21 but “By comparing with the experimental enthalpy of β, we found that the 0 K total energy calculated from bcc Ti is incorrect. This problem can be solved by shifting the total energy of β down by 8 kJ mol^{-1} to match the experimental value.” They base this on that they do not really do the calculations on the exact correct structure in the β phase. Their phase diagram is in Figure 11. VASP PAW (not specified which, which probably mean /Ti/) but with linear tetrahedron which would be preferred before Gaussian smearing that I think is used in References 21 and 17 (specifically mentioned in the latter).

Some good discussion on entropy and electron thermal/zero point energy contributions. This might indicate that we actually need to do DFT-MD also for the solid phases.

Hennig *et al.*(2008): Reference 19

Classical Molecular Dynamics work. The classical modified embedded atom potential is parametrized from data calculated by DFT.

Many of the discussions extends into how various pure Ti properties affect alloys, in particular Ti64.

Their phase diagram in Figure 5 shows the α, β, ω and liquid phases. The liquid phase is even less dependent on temperature than the questioned experimental data.[13] Their $\alpha \rightarrow \omega$ phase boundary is shifted up in temperature compared to basically every other study. But we shall remember that the computational studies are based on cold curve DFT data with temperature effects added on by other techniques. And the experimental data has very much hysteresis and possible non-hydrostatic compression issues. It is not at all sure that this study is less accurate. They also start their MD runs in the beta phase and see what phase they have after $\approx 1\,ns$. They would then have every possible intermediate vacancy and interstitial defect structure available that could circumvent a pure martensitic transformation. How pure is the final state?

Our main concern is this statement “The MEAM potential correctly predicts a metastable I_2 stacking fault with a high stacking fault energy (170 mJ / m^2) although not as high as in DFT (320 mJ / m^2) and experiment (300 mJ / m^2).” The experiment is from 1967. Could this lead to an too easy transformation from the α phase to the ω phase?

We would, again, do some well chosen DFT-MD calculations and compare with these calculations before pushing this technique or this specific potential further. But a good potential would probably allow us to study Ti64 explicitly.

Kutepov and Kutepova: Reference 29

Calculate the $\alpha \to \omega \to \gamma \to \delta$ transitions with PBE with their LAPW+lo code. Not too much detail but from previous work I trust their calculations to be fair. I would redo the calculations, though. Only $T = 0$ K, so not much work. They use the Debye model to get the $T = 300$ K isotherm to compare with experiment.

Ti64 Multi-Phase Wide-range EOS (including liquid phase)

Kerley (2003): Reference 23

See the same reference above.

Other Ti64 EOS

Cox (2012): Reference 10

Already in the abstract Cox points out one of the main problems with alloys: "Due to the limited data available for the alloy a multiphase EoS is first generated for pure titanium, before using a scaling method to obtain an EoS for Ti-6Al-4V."

This EOS for Ti64 is based on a mostly unpublished EOS for Ti. Apart from the short overview given in this paper, there is a poster and a very short conference paper[9] describing the construction. It seems the α and ω phases are taken as is from Kerley's Ti EOS[23] but the β phase is based on DFT calculations (VASP, PAW, PW91, calculations well described in poster). Figure 1 in the here described reference[10] is giving the final Ti phase diagram, it is reproduced in Figure 3.3, and it can be compared to the Kerley and Pecker *et al.* diagrams in Figures 2.1 and 3.2, respectively. Compared to Kerley's EOS (Figure 2.1) the melting transition on the Hugoniot is shifted down considerably towards the Pecker *et al.* transition.

A multiphase Ti64 EOS is obtained by a scaling of the Ti EOS via

$$P_{alloy}(\rho, E) = (1/\lambda) P_{Ti}(\lambda\rho, E)\,, \tag{3.1}$$

where λ is the room temperature ambient pressure density ratio (Ti over Ti64), P is pressure, E is internal energy, and ρ is density. However, the resulting EOS do not agree with available data, and as an interim solution a single phase EOS is constructed. However, this is not of large interest to us since we have Kerley's Ti64 multiphase EOS that should already be better then this single phase EOS. The multiphase EOS has a shock melting far below the one of Kerley's Ti64 EOS, which Kerley claims is already low because of Hugoniot data from

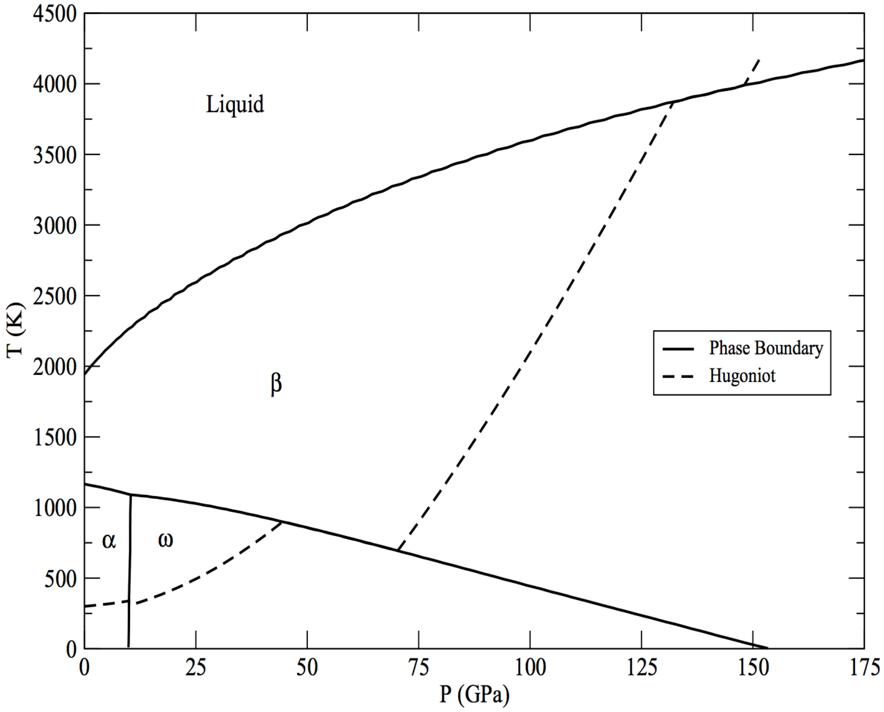

Figure 3.3. The phase diagram for pure Ti by Cox.[10] The α and ω phases are the same as in Kerley's Phase diagram, see Figure 2.1, and the Hugoniot in these regions is thus the same. The main difference from Kerley's EOS is the β phase, with consequences mainly for the melt line.

Hixon. Cox does not show the Hixon Hugoniot data in his Figure 5 since it is not published, just noted as Private communication with L. Chhabildas in Reference 56.

Hayes (1995): Reference 18

Ternary phase diagrams Ti-Al-V. Figure 7-15 show isothermal sections. Nothing about pressure, though. An interesting statement about the solid phases, that have been hinted at in other publications, is given: “No ternary phases have been reported in this system”. Of interest in our case could also be the binary Ti-Al and Ti-V diagrams in Figures 1 (Ti-Al) and 4 (Ti-V). From this data, ambient pressure phase transition temperatures for Ti can be deducted and estimated for Ti64.

Ti64 experiment (sometimes with DFT calculations)

Winfree *et al.* (2001): Reference 56

The measurement and analyses resulting in two points on the Hugoniot are described. Their Table 2 gives the results. In Kerley's EOS[23] these points are interpreted as being above (in pressure) the solid-liquid transition, thus describing a liquid state on the Hugoniot.

Dandekar *et al.*(2000): Reference 11

Compares elastic and plastic compression and spall strength between a low cost Ti64 and the 'normal' aircraft/aerospace grade Ti64 used in previous measurements (among them Reference 39 and 4). Their conclusion is that the low cost alloy behaves the same in compression but not for spall strength.

They give shock and particle velocities for 5 shock experiments in Table 1.

Andriot *et al.* (1994): Reference 4

Gives 4 Hugoniot data points for each of Ti and Ti64. In Table 1 as U_s-u_p pairs and in Table 2 as $P-\rho$ pairs. Sound speed, Poisson ratio, and Spall strength are also given.

Morris *et al.* (1988): Reference 39

VISAR Hugoniot experiments are shown in Figure 3 together with unreferenced previously measured Hugoniot data points. Some discussion on "why the Hugoniot does not extrapolate through the bulk sound speed at zero pressure". A Poisson ratio is also given.

Chesnut *et al.* (2007): Reference 8

Room temperature isotherm measurements, shown in Figure 2. They also find an $\alpha-\omega$ phase transition at 273 kbar. They give initial volume, bulk modulus, and derivative of the bulk modulus for both phases. This can be useful data for calculations. The phase transition has only a 1% volume change and they claim this is why it is not seen in dynamic experiments. They determine phases by x-ray diffraction, so this should be correct.

MacLeod *et al.* (2012): Reference 33

Room temperature isotherm is measured using DAC with structure determination by x-ray diffraction. They obtain an $\alpha \rightarrow \omega$ transition and $\omega \rightarrow \beta$ but no other phases. Figure 4 gives the isotherm data.

The transition pressures are confirmed with DFT calculations (CASTEP, PBE, OK settings). The DFT calculations also shed some light into the possible nature of the transitions. The DFT calculations are performed at $T = 0$ K with a 54 atom cells: “46 atoms of Ti, 6 atoms of Al, and 2 atoms of V; that is, 89.3 wt.% Ti, 6.6 wt.% Al, and 4.1 wt.% V.” They investigate two types of configurations: random configurations and ordered configurations with the alloying atoms as far apart as possible.

We would like to use these types of cell to do DFT-MD for the melting line.

Overall a very nice article.

Book Chapter “Titanium Alloys at Extreme Pressure Conditions” (2012): Reference 52

Gives a pretty thorough review of the Ti and Ti64 field, however, their phase digram (both Ti and Ti64) in Figure 9 doesn’t mention neither Kerley nor Cox, but only Pecker. The work they present seems to be the same as is presented in Reference 33 (their Reference Tegner et al., n.d.), however, the plots are not exactly the same but complementary. In particular we are intrigued by Figure 4, showing Pressure vs. atomic volume, since their results seems to be quite far from that of Reference 16.

Tegnér *et al.* (2011): Reference 50 and 51.

The LLNL report seems to be the first draft of the later MRS proceedings entry. Seems to be a precursor to Reference 33. Some material might be complementary but it rather seems like the later reference update, for example, the no pressure medium data. Only the ordered DFT calculations are presented in this paper.

Halevy *et al.* (2010): Reference 16

DAC experiments at room temperature targeting the $\alpha \rightarrow \omega$ phase transition. Unfortunately many spelling errors and mistakes (such as duplicate references in a reference list of only 12 references), give us doubts about the quality of this work. Figure 5 gives pressure vs volume for Ti64, while Figure 10 gives the same for Ti. We would verify the Ti data with other works before trusting the Ti64 data. Gives bulk moduli and derivative thereof extracted from a fit to the Vinet EOS, for both Ti64 and Ti.

Rosenberg *et al.* (1981): Reference 47

Give values for the HEL (Hugoniot elastic limit) for Ti and Ti64. They speculate about a phase transition around 10 GPa but need more evidence (which we think did not materialize). If the break in P vs u_p is also present in other measurements of the Hugoniot, we would think about this article again and consider their explanation (based on meta stability).

Reinhart *et al.* (2001): Reference 45

Two high pressure (≈ 250 GPa) Hugoniot points are given. The main part of the article is describing how to perform these high precision experiments. Very educational reading.

Ti64 with DFT

See Reference 33 above.

Mechanical properties of Ti64

Millet *et al.* (2008): Reference 38

This article mainly investigates the shear stresses/strength of Ti64. But in the process they get a few Hugoniot points. Their linear $U_s - u_p$ fit (their equation 4) is different than the one given in equation 11 in Reference 45.

Bourne *et al.* (2009): Reference 6

Mostly about strength. Seems to be an excellent review if one is going into the field of strength modeling. Hugoniot data in Figure 8. $U_s - u_p$ relation taken from Reference 38.

Nemat-Nasser *et al.* (2001): Reference 40

Measure and give constitutive model for flow stress as a function of strain rate and temperature for three different types of Ti64. No equilibrium data.

Niu *et al.* (2010): Reference 41

Peak flow stress as a function of strain rate and temperature. No equilibrium.

Kar *et al.* (2005): Reference 22

"This paper will discuss the development of neural network models based on a Bayesian framework to predict the yield (YS) and ultimate tensile strengths (UTS) of Ti-6Al-4V at room temperature."

Lee *et al.* (1998a): Reference 30

Stress as a function of strain, strain-rate, and temperature (Johnson-Cook).

Lee *et al.* (1998b): Reference 31

Quite some overlap with Reference 30 by the same authors. These two papers are sent in just one month apart! Give other values for the same fit as in Reference 30.

Majorell and Picu *et al.* (2002): References 34 and 44

These references are Part I and II for developing a constitutive model for Ti64 of yield stress vs strain rate and temperature for both $\alpha + \beta$ together and separately. Experiments are described in Part I and the modeling in Part II. Seems to be thorough and both parts should be read if strength modeling would be embarked upon.

Seo *et al.* (2005): Reference 48

Focused on the development of high-temperature apparatus development and use Ti64 measurements as test. High temperature is 1000 °C (they say melting at ambient pressure is 1668 °C). Comparing data in Figure 18 to corresponding figures in Lee *et al.*'s articles

(Figure 5 in Reference 30 and Figure 3 in Reference 31) shows considerable differences, and the fitting parameters in the Johnson-Cook model get yet another set of values. For 1000 °C, the true stress in Lee is about the double compared to the one in this article.

Zherebtsov *et al.* (2005): Reference 59.

The first sentence in the abstract says it all: "A comparative investigation of mechanical properties of Ti6Al4V titanium alloy with microcrystalline and submicrocrystalline structures".

Mescheryakov and Divakov (2001): Reference 37

This article describe strength experiments on another Ti alloy, VT-16, which has less aluminum and additional molybdenum compared to Ti64.

Chapter 4

Summary and Conclusion

Titanium: In addition to the two data points at the ambient pressure isochor, the $\alpha \rightarrow \beta$ phase transition temperature at 1155 K and the melting at 1941 K, there is data available for the primary shock Hugoniot and for isotherms. There is also experimental data for the melting line,[13] seen as white dots in the Pecker *et al.* phase diagram in Figure 3.2, but the accuracy of this data is in question. The articles with calculated data points mostly focus on the phase boundaries between the three solid phases. Figure 4.1, taken from Reference 21 (Figure 7), summarizes these studies.

J. Appl. Phys. **107**, 093509 (2010)

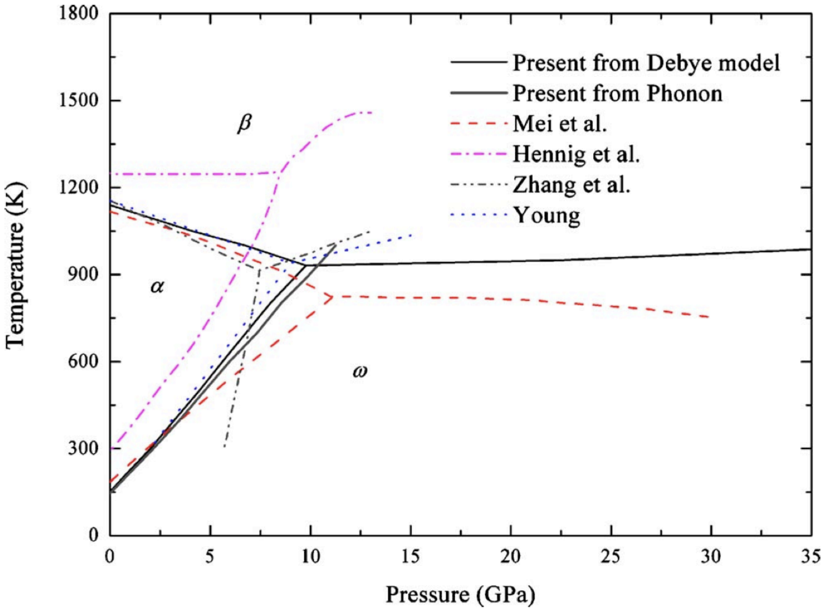

Figure 4.1. The solid phase diagram for pure Ti, taken from Reference 21 (Figure 7).

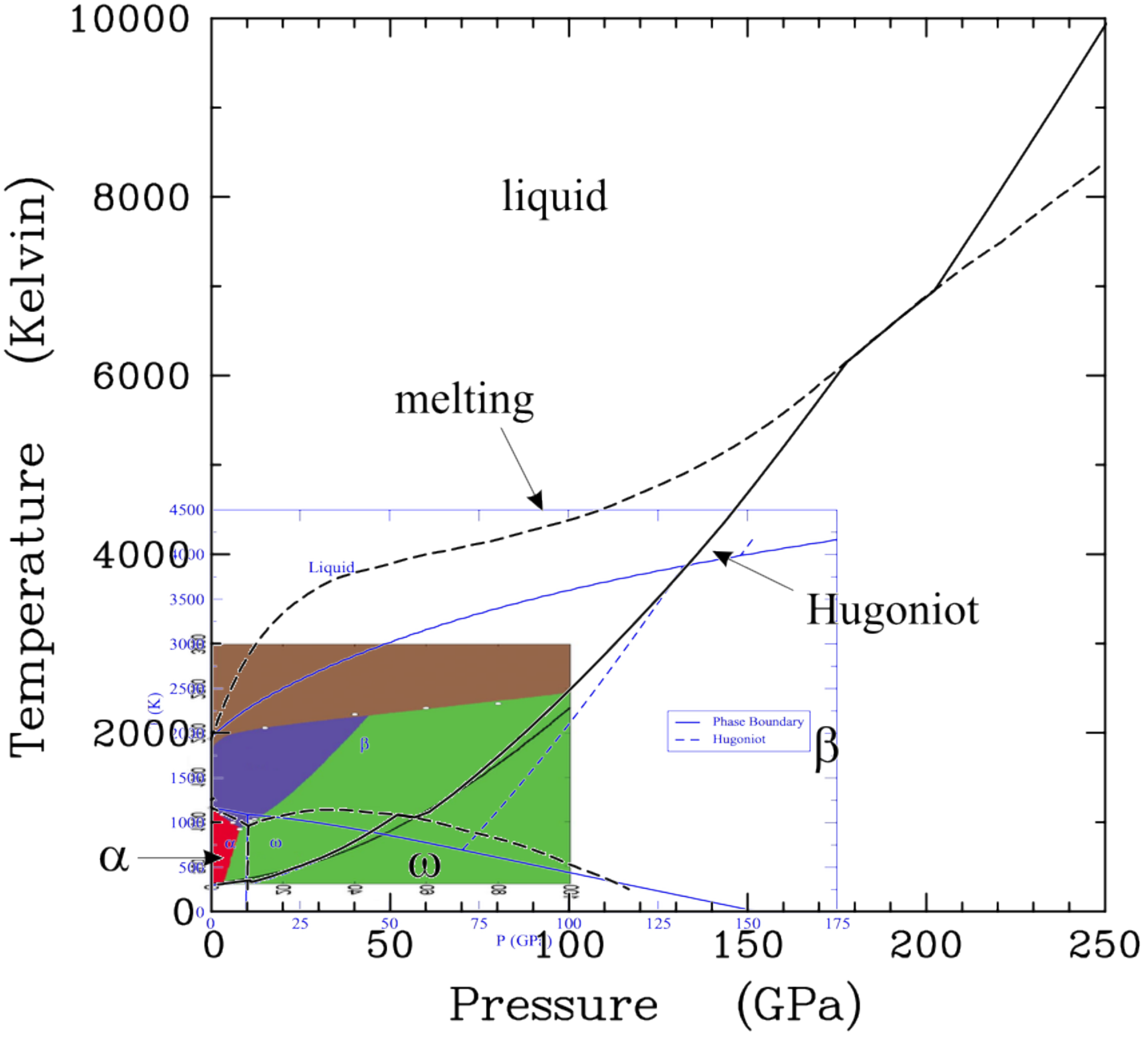

Figure 4.2. The phase diagrams for pure Ti in Figures 2.1, 3.2, and 3.3 overlaid in the same plot to accentuate the differences between them.

In Figure 4.2 we have combined the three phase diagrams in Figures 2.1, 3.2, and 3.3, in one and the same diagram. The most disturbing difference is in the melt lines. If the melt line data[13] is discarded as faulty, no experimental data is available since the Hugoniot crossing is not very well determined either. On the other hand, Cox's very different Hugoniot crossing of the $\alpha \rightarrow \omega$ phase boundary does indeed show up as a less accurate fit to the experimental Hugoniot data. As is seen, available data for Ti do not constrain the phase diagrams very well. The situation is even less satisfying for the alloy Ti64.

Titanium alloy, Ti64: The situation regarding the EOS data for Ti64 is even less satisfactory than for pure Ti. It seems the main experimental effort for this material has been on strength properties, perhaps as a reflection of the main interest in this alloy as a strong and light material.

Chapter 5

Suggestions

Minimal solution or first step

We can use only the data given in the references in this report. The current status of our uncertainty quantification (UQ) enabled EOS capability would allow us to construct a multiphase EOS containing one solid and one liquid phase. This would allow us to investigate how large an effect the existing data have on the melt line. This can be done for both Ti and Ti64. The resulting EOSs would probably not be as good as the existing EOSs by Kerley but would provide a quantitative opinion on the data used by Kerley.

Intermediate solution or second step

Multiple solid phases

In the next step we should include many solid phases and still use only the available data. This will allow us to determine how large an effect the different solid phases have on various types of calculations compared to if the solid phase is treated as only one. Here it needs to be decided how many phases to include and how to treat the alloy that in fact has different phases in the grains (α) and in between grains (β). Questions to investigate are:

- Should a normal distribution of defects be included in the EOS?
- How do we properly describe a heterogeneous material such as an alloy?
- How do we deal with the large amount of hysteresis present at solid-solid phase transitions?

Multi-solid-phase UQ enabled EOSs would at least provide a quantitative opinion on what can be achieved with currently available data. These EOSs might even provide a superior interpretation of the data compared to Kerley's EOSs.

Melt line data

For a guaranteed improvement over Kerley's EOSs we need more data. We can calculate melt lines for both Ti and Ti64 by using the *ab initio* DFT-MD technique. DFT-MD is molecular dynamics (MD) where the forces that determine the movement of ions are calculated with the use of DFT,[20,24] see Figure 5.1. This is a very accurate but computationally expensive technique that is increasingly used for providing data in parts of the phase space where experiments are impossible, dangerous, and/or expensive to perform.

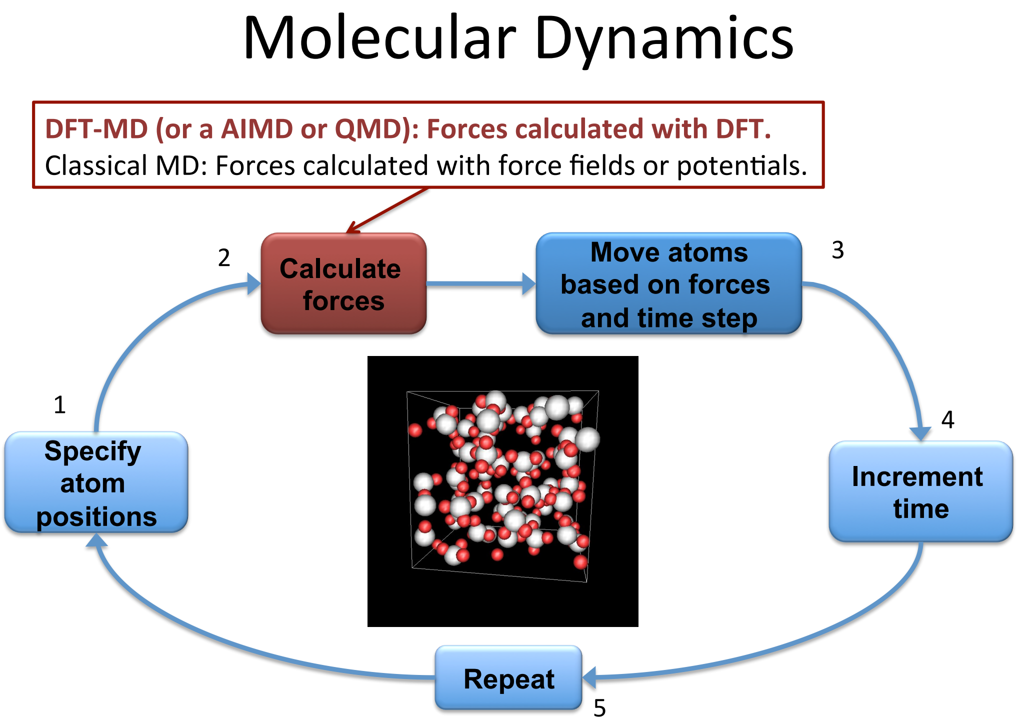

Figure 5.1. The loop followed while doing a molecular dynamics calculation. The forces necessary for updating the atomic positions can be calculated from material and configuration specific classical force fields or potentials, or by DFT-MD which is a general technique without material specific input, only the atomic number, Z, of included ions is needed. Thus the water DFT-MD simulation represented by the snapshot in the center of the loop only needed the specification that the simulation cell contained 64 oxygen (Z=8) and 128 hydrogen (Z=1) atoms.

The accuracy of the DFT technique used for calculating forces in a DFT-MD scheme is embedded in the material independent *exchange-correlation functional* (often abbreviated to only *functional*). There exists a *divine functional*[35] that would give the exactly correct forces for all possible and impossible materials. However, since this functional is of unknown form, approximations need to be used in practical calculations. Existing approximations (functionals) are very accurate for most materials, which is at the foundation of the success of DFT-MD as a technique to provide data for EOS construction and for understanding materials in general.

Unfortunately there are a few types of materials where existing functionals do not provide as high accuracy, and Ti is in one of these categories. We will discuss this more thoroughly in the next section. The calculations should be performed with several of the existing functionals in order to be able to estimate the magnitude of this functional error. Other error sources need to be controlled as well and the calculations of the melt lines should be complemented with assessments of the quality of the DFT calculations by comparison between calculations performed with the all-electron RSPt and pseudo-potential VASP codes, in particular at higher compression and of electronic states populated at higher temperatures.

There are several well established methods available to determine melt lines from DFT-MD simulations. We will probably use the one that starts with a simulation cell with half liquid (disordered state) and half solid (in the β phase) and that evolves to a single solid or liquid phase depending on temperature. The melting temperature is the temperature above which the start configuration evolves to the liquid phase and below which it evolves to the solid phase.

For the melt line, the alloy can probably be modeled by the simulation cell of 54 atoms with well separated impurity (Al and V) atoms used in several of the references above. However, additional calculations should be done to probe the influence of this approximation. Perhaps a larger cell (108 atoms) should also be tested.

Final solution or third step

Development of DFT for *d*-electron materials

Electrons are *fermions*, a type of quantum particle that obeys Fermi-Dirac (FD) statistics as opposed to the boson quantum particles with their Bose-Einstein distribution and classical particles with their Boltzman distribution. A particle's statistics determines the distribution of energies the particle can have at a specific temperature. The main consequence of the FD statistics is that two fermions cannot occupy the same quantum state, effectively creating a repulsive force between them. Electrons around a positive charge, an ion, can only occupy certain states, each state or *orbital* having a well defined spatial symmetry. The two electrons, one with spin state "up" and one with spin state "down", closest to the ion are in an orbital with spherical symmetry, a so called *s*-state[i]. The next *shell* contains 2 more *s*-electrons with a 2*s* orbital that on average is further out from the ion than the one the 1*s* electrons occupy, and 6 *p*-electrons, 2 each in orbitals with axial symmetries along the spatial x, y, and z directions. The third shell, contains 2 each of 3*s* and $3p_x$, $3p_y$, and $3p_z$ electrons. In total we now have *s* and *p* states sufficient for 18 electrons, that is, for the element with $Z = 18$, which is argon. We saw that the first shell had *s* states only, the second shell had *s* and *p* electrons, so the third shell should have yet an extra type of symmetry, and indeed there are states available for 10 3*d* electrons. However, these states do not start to be populated until after the 4*s* state has been populated with two electrons, and the first element with *d*-electrons is scandium with $Z = 21$. The second element with *d*-electrons is Ti $(Z = 22)$. The two alloying elements in Ti64 are aluminum $(Z = 13)$, with only *s* and *p* electrons, and vanadium $(Z = 23)$ which has one more *d*-electron than Ti.

The outermost electrons in an atom are the ones that feel the effect of, and can interact with, other electrons from nearby atoms. These *valence electrons* can form bonds which hold the atoms together in different types of structures. The types of bonds and the types of structures formed are dependent on the symmetry of the electrons involved, this should be evident from Figure 5.2. The *s* electrons tend to join other *s* electrons from other ions and create a "sea" of electrons that extend all over the structure which then is a metal. All these electrons have approximately the same potential and differentiate among themselves by their kinetic energy. The paradigm system for understanding metallic bonding of this type is the *uniform*, or *free electron gas*, a model system that is at the core of most DFT exchange-correlation functionals used for solid state applications.

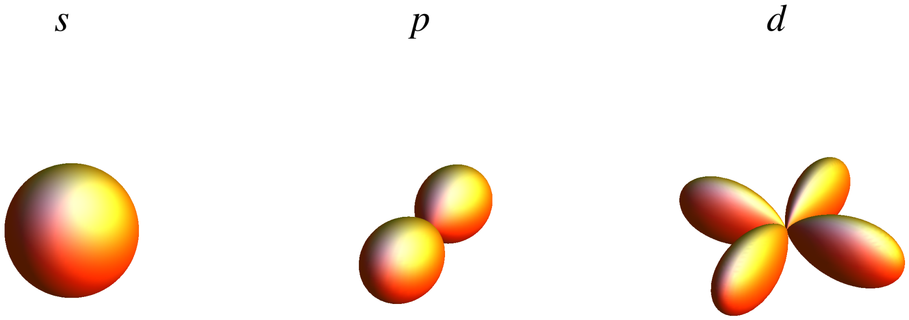

Figure 5.2. Magnitude of the electron density in different directions around the ion, for electron densities formed by one *s*, *p*, or *d* electron, respectively.

Adding in some *p* electrons can have very different effects. Aluminum has one *p* electron

---

[i] The electron orbitals are named from spectroscopic lines, *s*harp, *p*rincipal, *d*iffuse, and *f*undamental. Higher states go in alphabetical order from *g*, omitting *j*.

and, in fact, is considered the prototype free electron metal. Silicon has one more p electron and here the effect is profoundly different. In silicon the s and p electrons from adjacent ions create new states, they *hybridize*, and form strong *covalent* bonds that tend to keep ions together in tetrahedrons. The prototype for this structure is diamond, which have the same electron structure with 2 each of s and p electrons in the valence but only 2 other electrons (of s type) that can weaken the bond (silicon has 10 other electrons). Both silicon and diamond are *insulators* since the electrons are tied up in the strong bonds and cannot easily move within the material structure; the electrons are *localized*. We note that covalent bonds are prevalent in chemistry but we restrict ourselves here to condensed matter.

The strength of bonds in materials tend to range between the metallic s/free electron metal and the insulator covalent diamond bond with localized electrons. The 4 valence electrons in Ti are 2 each of $4s$ and $3d$. Titanium is a metal but it is easy to understand that the presence of d electrons provide opportunity for hybridization. As seen in Figure 5.2, d electrons have more and narrower lobes than p electrons have. This give rise to a multitude of different possible structures/ionic arrangements to allow for differences in temperature and pressure. For Ti this is evident in the many different solid phases present in the phase diagram, see Figure 2.1. Even more pronounced is the situation in Ti alloys, where the addition of alloying elements provide for yet more opportunities to enhance or suppress localization of electrons. The transition from the hcp (α) phase at room temperature to the bcc (β) phase at higher temperature in Ti, is attributed to enhanced population of the d-electron states with temperature.[ii] Replacing some of the Ti atoms with Al, takes away d-electron states and the α phase is *stabilized*. On the contrary, the addition of d-electron states by replacing Ti atoms with vanadium atoms instead stabilizes the β phase.

DFT exchange-correlation functionals are available to treat materials that are either metal like or insulator like, but there is no single functional developed that can give a good accuracy for materials, such as Ti, W, V and similar materials, that exhibit both the free electron like character of metals and the localized electron character of insulators. While available functionals probably are good enough to give accurate melt lines where more distinct changes in electronic structure are present, they are probably not accurate enough for describing the solid-solid phase transitions and alloying effects well, where the intricate competition between localized and delocalized electrons is dominating the physics.

Over the last several years, Ann Mattsson and her collaborators have studied ingredients that are needed to create a functional with equal accuracy for localized and delocalized electronic structures. The two main ingredients they have studied are the *harmonic oscillator gas* (HO gas) model system and the *electron localization function* (ELF). The HO system is a caricature of a real system exhibiting the mixture of localized and delocalized electrons but in a simplified setting suitable for analytical and numerical studies. The ELF is a tool to find regions in space where localized or delocalized electrons exist. They plan to combine these

---

[ii] In fact, increased pressure similarly (initially) enhance the localization of electrons with a transition from the α phase to a less metallic ω phase. The pressure at room temperature of this transition was initially established by resistivity measurements (see Reference 49), probing this change in the metallic nature due to the localization of d-electrons.

two ingredients into a functional according to the *subsystem functional* scheme invented by Ann and her collaborators, and test the resulting functional for accuracy in systems like the one present in Ti.

Development of method for martensitic phase transitions

While there are well-tested methods for calculating melting transitions, the situation is far less developed for solid-solid phase transitions such as in Ti. The difficultly lies in describing the entropy difference between two solid phases, which is not directly calculated for ions in DFT-MD. Recently a DFT-MD technique has been developed[42] to calculate this entropy difference for one class of reversible solid-solid transitions, the martensitic transition. We would leverage and further refine this prototype DFT-MD technique and use it to calculate the phase boundaries between the solid phases in Ti, all these phase transitions being martensitic. We would also look into the more general question to determine the entropy difference for all classes of solid-solid transitions. We would have two thrusts. First, we aim to discover new techniques to directly calculate the needed entropy, and thus entropy difference, using DFT-MD and other first principle methods. Second, we propose to transform the current semi-empirical model description of the entropy into a first principle method by investigating ways to use DFT calculations, such as phonon spectra, to inform and improve those models. The method of using DFT determined phonon spectra has already been used in some of the DFT references described above but we would further develop these kinds of schemes and formalize them for more straightforward use.

Development of constitutive models

This is particularly important for alloys since they very often are (experimentally) developed with a certain property, such as strength, in mind and thus need a correct constitutive model to properly describe this property in codes. For this project collaborations are needed beyond the current expertise in our EOS group, see upper path in Figure 5.3. Indeed, connecting our EOS expertise with expertise in constitutive modeling would be very valuable for the future and enhance both fields.

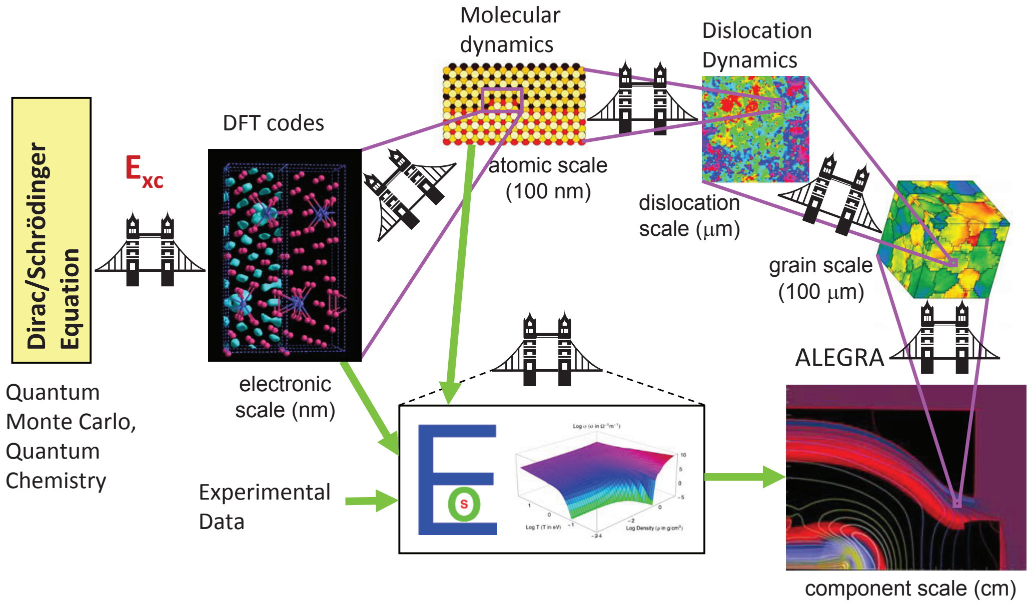

Figure 5.3. The foundation of Science Based Engineering is to build bridges from the fundamental Laws of Nature up to the Engineering codes, bridging several length and time scales. In this figure two different paths are depicted. The upper one is quite complicated and illustrates the general problem of bridging several different scales. The lower path is already in use at Sandia. For Equation of State construction, data provided by Density Functional Theory based calculations are used in addition to experimental data. The DFT calculations are used in two ways, either directly or as a provider of forces in a Molecular Dynamics scheme. From SAND2011-9457.

Appendix A

A Study of Cloud Formation of Ti6Al4V in Hydrodynamic and Solid Dynamic Simulations with ALEGRA

A.1 Introduction

The multi-physics computational tool, ALEGRA,[46] is commonly used for simulations of impact and penetration events. These simulations incorporate the interaction of multiple materials for hydrodynamic and solid dynamic problems in physics, for which the use of an appropriate equation of state for a material is critical. One issue that has been encountered by ALEGRA users for such applications is the apparent formation of vapor clouds from initially solid material. This occurrence, also referred to as "spitting", is typically associated with small fragments of material which have separated from one or more larger bodies as a result of an impact, and which utilize tabular equations of state. As a consequence of cloud formation, the computed time step is drastically decreased, slowing or even killing the simulation. The cloud formation event, whether physical or not, is an unwelcome feature for users, which is usually of little or no importance to the problem of interest. The source of this problem is commonly thought to be an inadequate equation of state. A number of cloud formation occurrences have been observed when using the SESAME tabular equation of state for the titanium alloy, Ti6Al4V.[23] Is an inappropriate equation of state for Ti6Al4V causing cloud formation? Is the observed cloud formation physical? Can it be prevented? The objective of the study in this appendix is to answer these questions.

In order to address the cloud formation issue, a baseline ALEGRA simulation is studied for which a cloud is produced. Analysis of the simulation results, which utilizes ParaView, includes visualization of the thermodynamic path data on the equation of state surface. This type of analysis utilizes the Prism plugin tool in ParaView. Variations of the baseline problem are then simulated by changing various ALEGRA algorithmic options in order to study their effect on the cloud formation results. The baseline problem is defined and analyzed in Section A.2. Section A.3 presents the study of the effect of variations to the baseline ALEGRA simulation. Conclusions and recommendations for future work are then summarized in Section A.4.

A.2 Demonstration of Cloud Formation: The Baseline Problem

Nonphysical formation of a cloud in a Eulerian hydrodynamic ALEGRA simulation is demonstrated by the 2D axisymmetric problem of the impact of a Ti6Al4V sphere with a 4340 steel plate. Sesame EOS tables are used for both materials with the KEOS Sesame model used as the interpreter (Sesame table 4061 for Ti6Al4V and Sesame table 2150 for 4340 steel). Details of the problem are provided in the ALEGRA input in Section B.2. Figure A.1a displays the initial configuration of the problem. Shortly after impact, mixed-material fragments of Ti6Al4V and steel are ejected and dispersed away from the impact location (Figures A.1b and c). One of these fragments forms a low density cloud of Ti6Al4V at a later time (Figure A.1d). This sphere impact problem follows from the experiments performed by Grady and Kipp,[14] and will be referred to as the baseline problem. The ALEGRA input for the baseline problem is found in Section B.2 of the appendix.

A closer look at the history of thermodynamic states for Ti6Al4V in this problem is provided in Figures A.2-A.7. Configurations of the problem and the corresponding thermodynamic state of the Ti6Al4V are plotted side by side. Both the problem configuration and EOS pressure surface are colored according to pressure. All units are expressed in SI. The initial state of the Ti6Al4V sphere is actually in the tension (negative pressure) region (Figure A.2). Once the projectile material experiences shock loading some material is heated to very high temperature (Figure A.3). Upon pressure release, one of the resulting mixed-material fragments is in a mixed liquid-gas state once it separates (Figure A.4). As the particle advects through the grid it experiences a significant increase in pressure (Figure A.5) into a plasma state followed by a significant increase in temperature (Figure A.6). A rapid decrease in pressure, temperature and density then results in the formation of a cloud of Ti6Al4V gas (Figure A.7). Although this ultimate observable state seems unphysical, the path of thermodynamic states of the separated particle material appears to be incorrect well before the cloud formation event.

An even closer look at time history of thermodynamic states for the material in question is presented in Figures A.8 and A.9 for Ti6Al4V and 4340 steel respectively. This history data was extracted from high time resolution exodus output for the sphere impact problem using ParaView with the Prism plugin. The data represents states of the material that eventually forms the cloud of gas. Continuity of the thermodynamic state of the material in time is first assumed. The state data visualization in prism provides the connectivity to the material location, allowing for the physical trajectory of the material to be traced backwards in time from cloud formation to its initial state and position. The plots in Figures A.8 and A.9 reflect the average material quantities for several elements at a given time. Although this method of data extraction is tedious, it proved to be more reliable than Lagrangian tracer history which failed to provide a complete picture of the thermodynamic state path leading to cloud formation. This is the case even when the trajectory of the material is known after the fact and tracers are placed at the initial positions of material that eventually forms a cloud. It is noted that the initial position of this material is located on the projectile at the projectile-target interface. The procedure for the data extraction technique described above is outlined in Section B.1 of the appendix.

The red vertical lines in the plots in Figures A.8 and A.9 indicate the point in time when the material separates into a particle. The corresponding thermodynamic state will be referred to here as the separation state. In the baseline case separation occurs at about $1.75\mu s$. The unphysical thermodynamic state path is easily noticeable for both materials at about $7\mu s$ when the temperature and energy dramatically increases and decreases for Ti6Al4V and 4340 steel respectively. The temperature of the steel is forced to the lower limit of $1K$ while the Ti6Al4V is heated to about $14000K$. Once a certain state is attained by the mixed-material particle, the energy balance is sustained, but at the expense of pushing each material into very extreme and unphysical states. Plots of thermodynamic state history after particle separation are also plotted for Ti6Al4V and 4340 steel in Figures A.10 and A.11 respectively. It should be noted that the mixed-material particle consists of Ti6Al4V in a compressive state and 4340 steel in a tensile state.

During this study it proved useful to perform simulations of the fragment material only, in order to isolate the effects of changes to the initial separation state of material. This was accomplished by exporting the ALEGRA miniexodous solution output of the particle material once it separates, and subsequently importing that solution as an initial state for an Eulerian problem of a particle moving through the same grid. Figures A.12-A.15 display a comparison of results for a single particle analysis for which the initial thermodynamic state is that of the mixed-material particle at the time of separation ($\approx 2\mu s$). As expected, the isolated particle simulation corresponding to the baseline problem yields the same cloud formation result observed previously (Figures A.12a-A.15a). However, different thermodynamic state paths for the particle are realized when its separation state is altered from the baseline case. The most revealing cases correspond to that of the static particle simulations, which simply impose zero velocity for a separated particle at a given thermodynamic state (Figures A.12b-A.15b). Static particle calculations initiated in the mixed liquid-vapor state result in the same outcome; the density of the Ti alloy decreases at roughly constant temperature and pressure across the vapor dome until it becomes gas, at which point, the gas expands rapidly. This is the expected behavior of the particle given its initial thermodynamic state, and while this particle-to-cloud formation may be undesirable in applications, this behavior is physical. The static particle simulation reveals that the motion (initial velocity) is the critical factor that determines whether or not the thermodynamic state path of the particle material is physical or not. The issue is actually not the formation of the cloud, but the preceding thermodynamic states encountered.

If copper is used as the spherical projectile material in the baseline calculation, a cloud of copper is also produced (Figure A.16). The thermodynamic states of copper at several instances in time are displayed in Figures A.17-A.20. Although the path of the states leading up to cloud formation are different for Ti6Al4V and copper, it should be noted that the separation states of the particle materials from which the cloud originates reside in the mixed liquid-vapor state of their respective thermodynamic space. However, the expected physical behavior is observed for the case of copper.

Should a fragment resulting from the sphere impact problem be in the mixed liquid-vapor state upon separation? The baseline case for the sphere impact problem certainly predicts this outcome for both Ti6Al4V and copper. Given the high speed impact of projectile, a phase change of some material is quite possible. It may be that the observed behavior is consistent with the equation of state models, but the models may not accurately reflect physics due to assumptions made for their development and implementation.

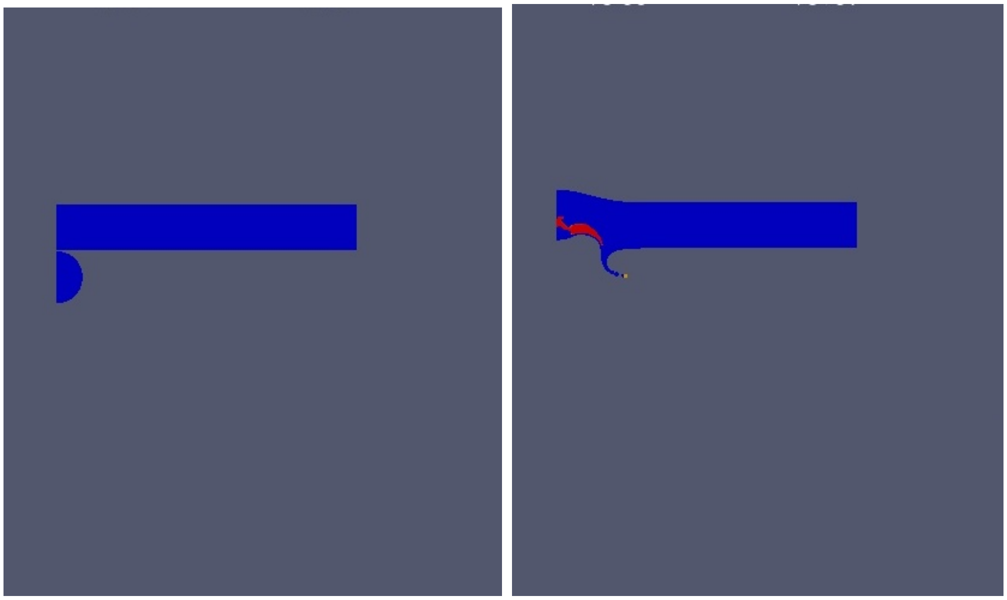

(a) initial configuration

(b) t = 2 μs

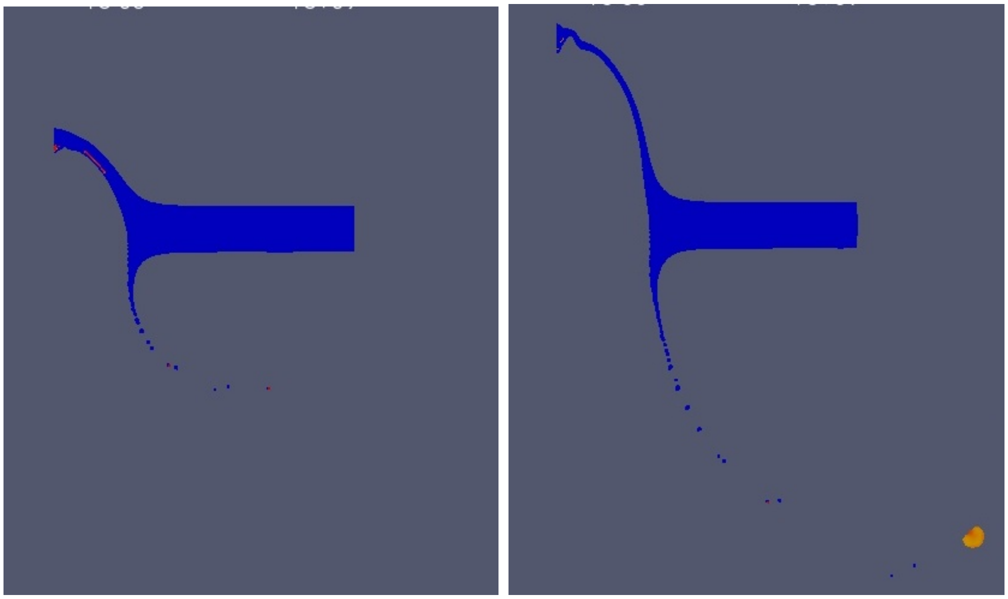

(c) t = 7.5 μs

(d) t = 15 μs

Figure A.1. Baseline problems: Impact of a Ti6Al4V sphere on a 4340 steel plate resulting in a Ti6Al4V cloud formation

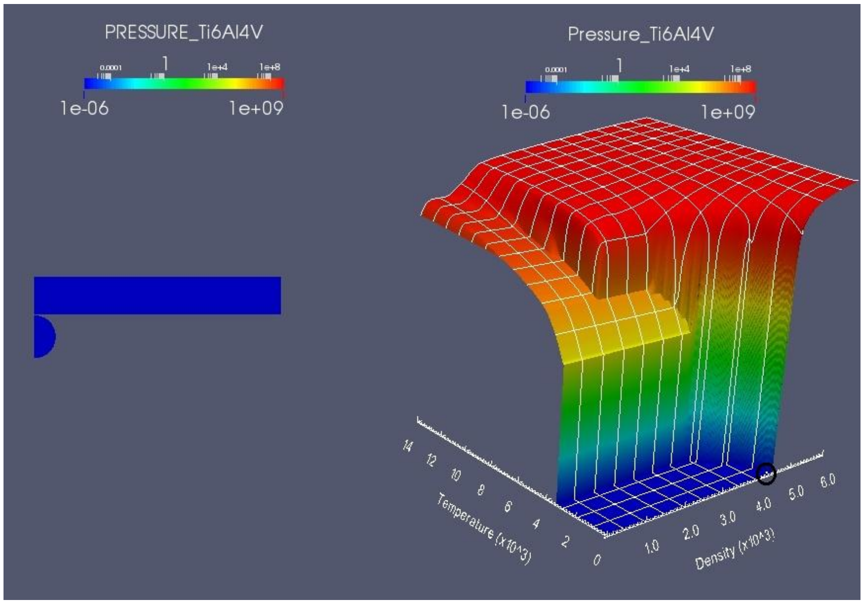

Figure A.2. Initial configuration & thermodynamic state

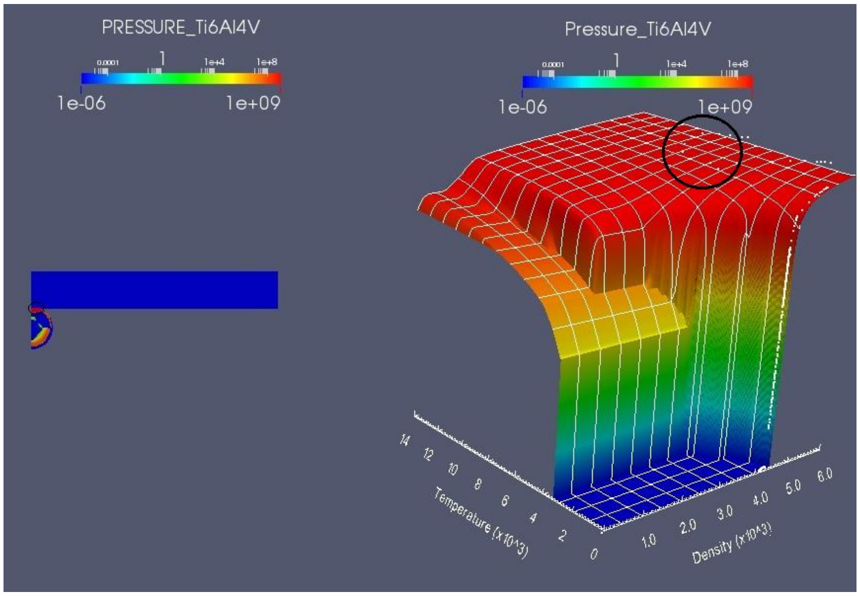

Figure A.3. $t = 0.01\mu s$: Shock compression of sphere

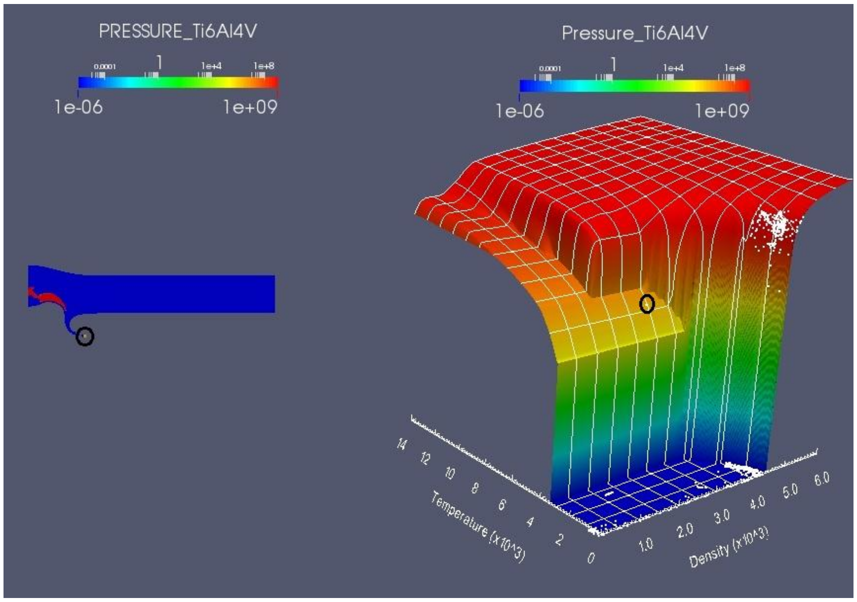

Figure A.4. $t = 2\mu s$: Separation of high pressure fragment

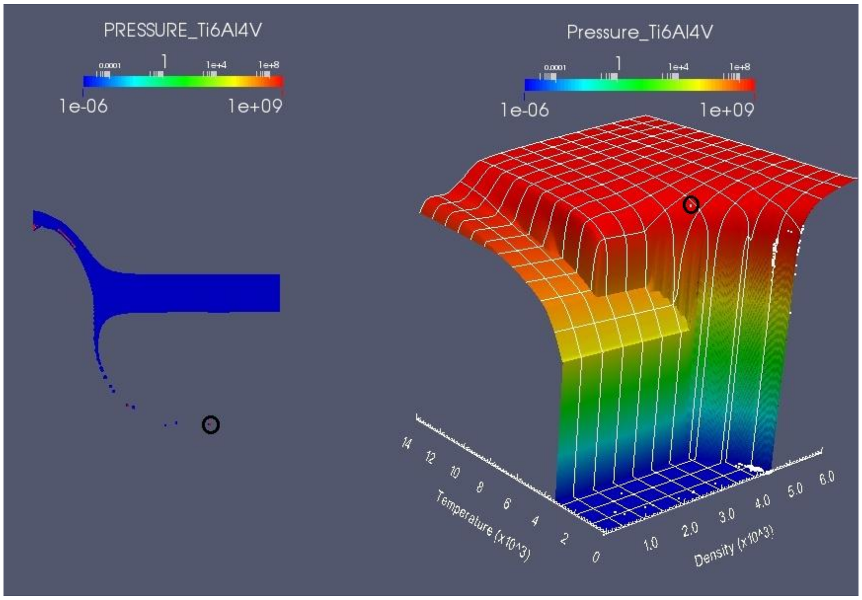

Figure A.5. $t = 7.5\mu s$: Increased pressure of fragment

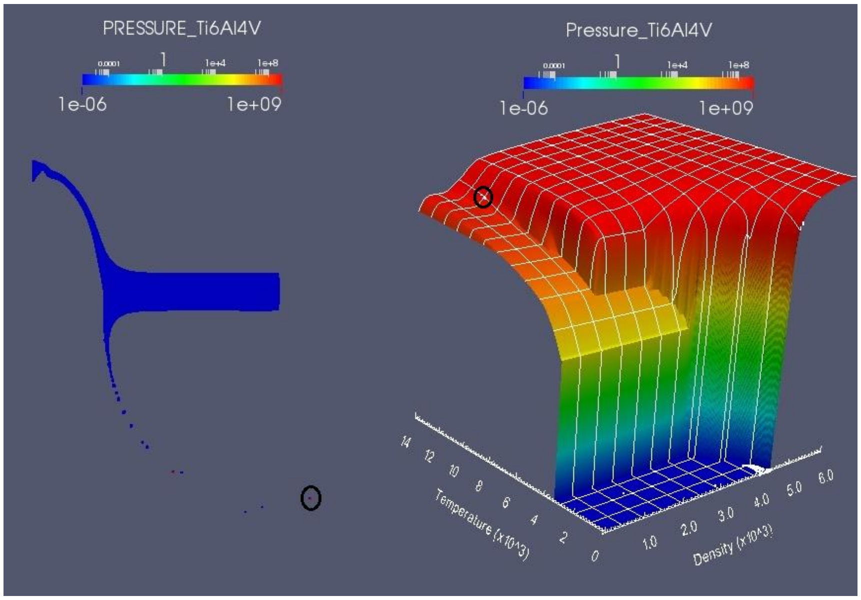

Figure A.6. $t = 12\mu s$: Increased temperature of fragment

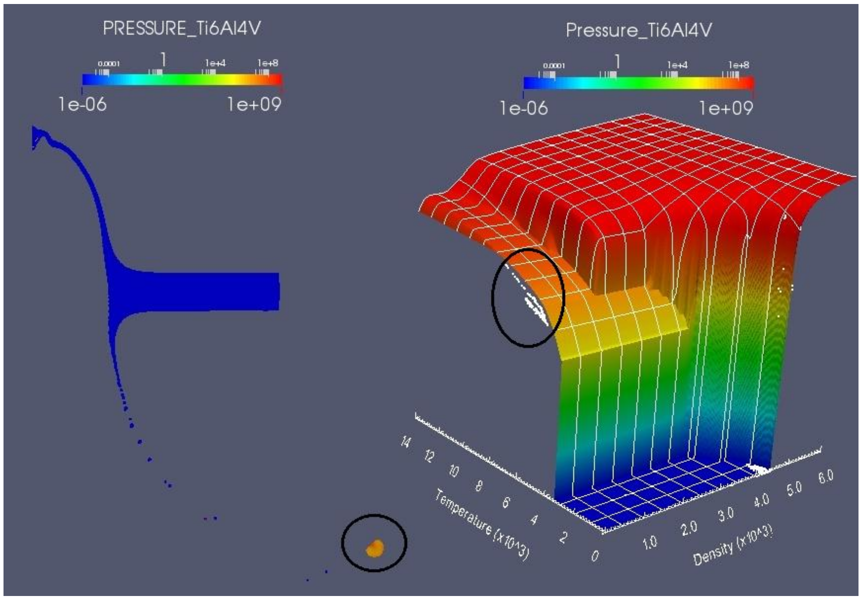

Figure A.7. $t = 15\mu s$: Rapid decrease in density & cloud formation

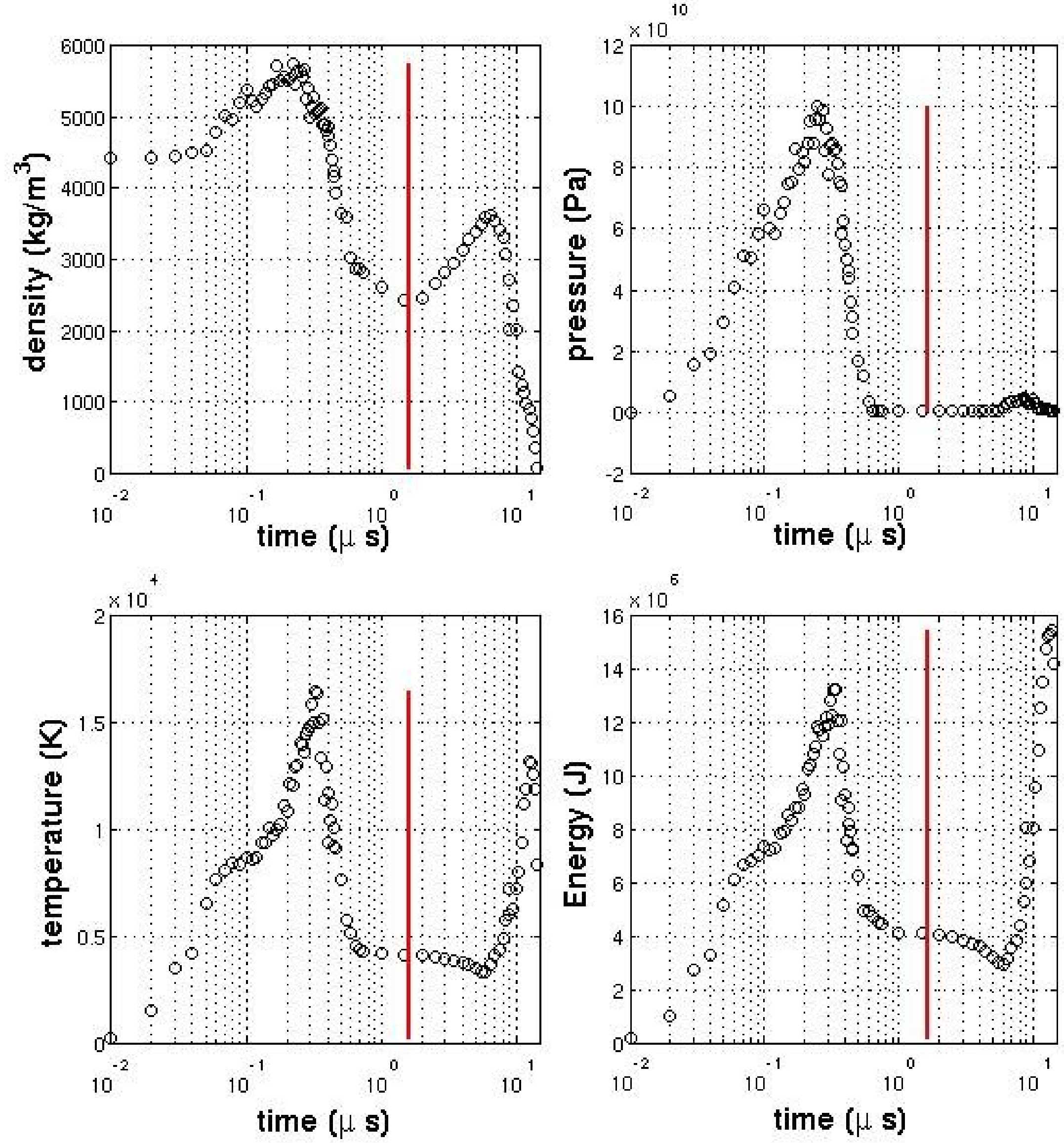

Figure A.8. Baseline: History of thermodynamic states of Ti6Al4V

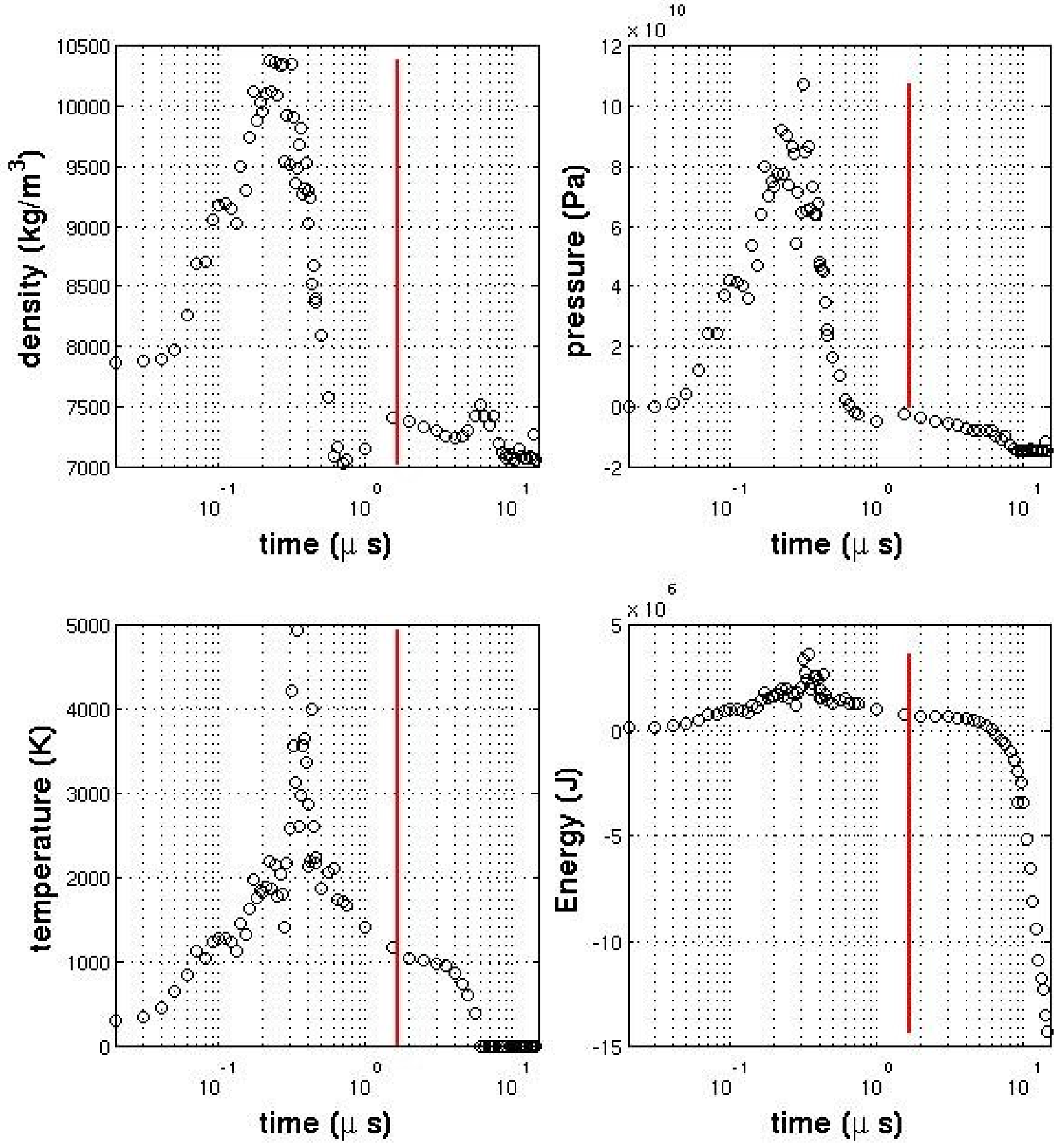

Figure A.9. Baseline: History of thermodynamic states of 4340 steel

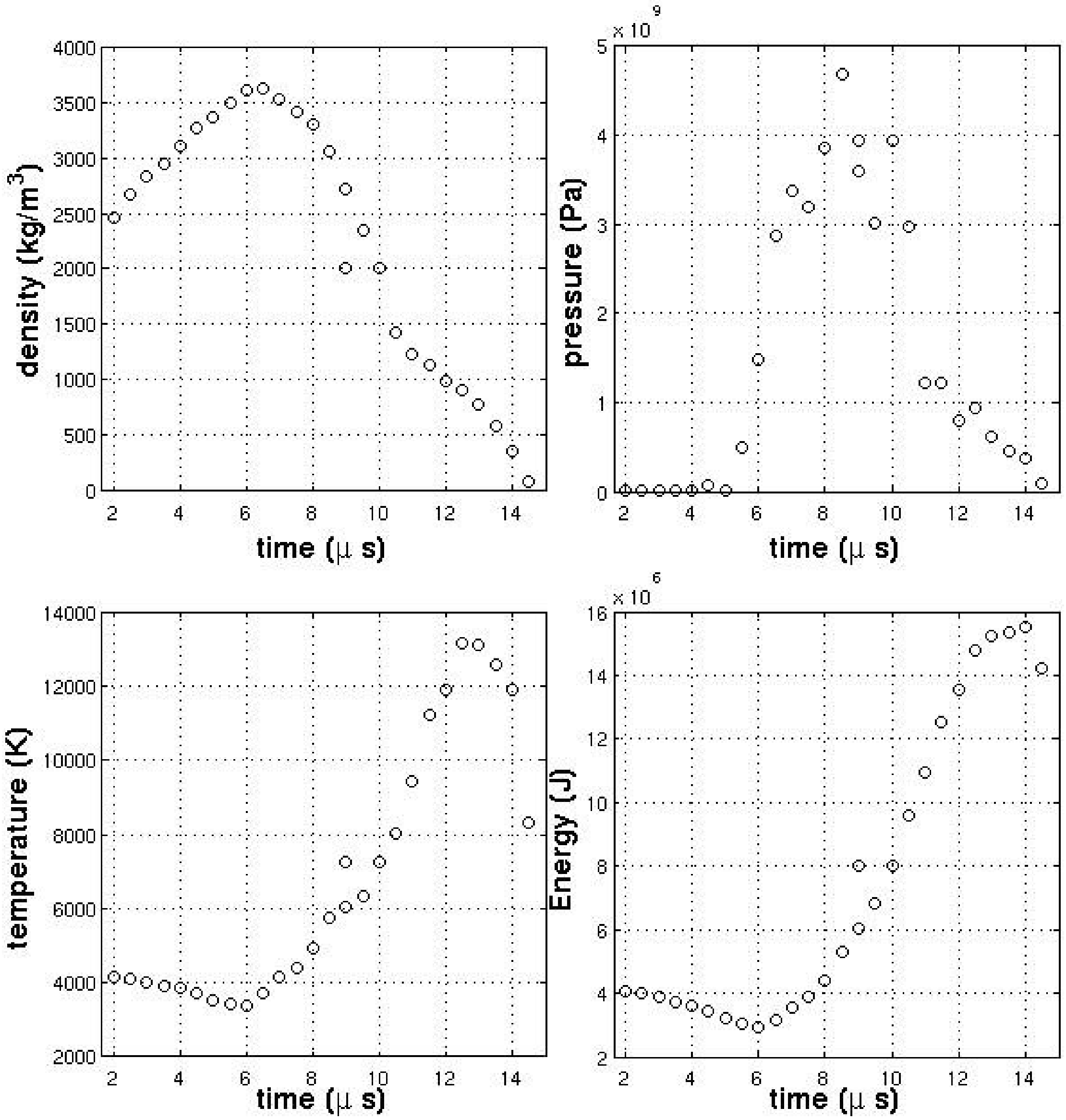

Figure A.10. Baseline: History of thermodynamic states of Ti6Al4V for separated particle

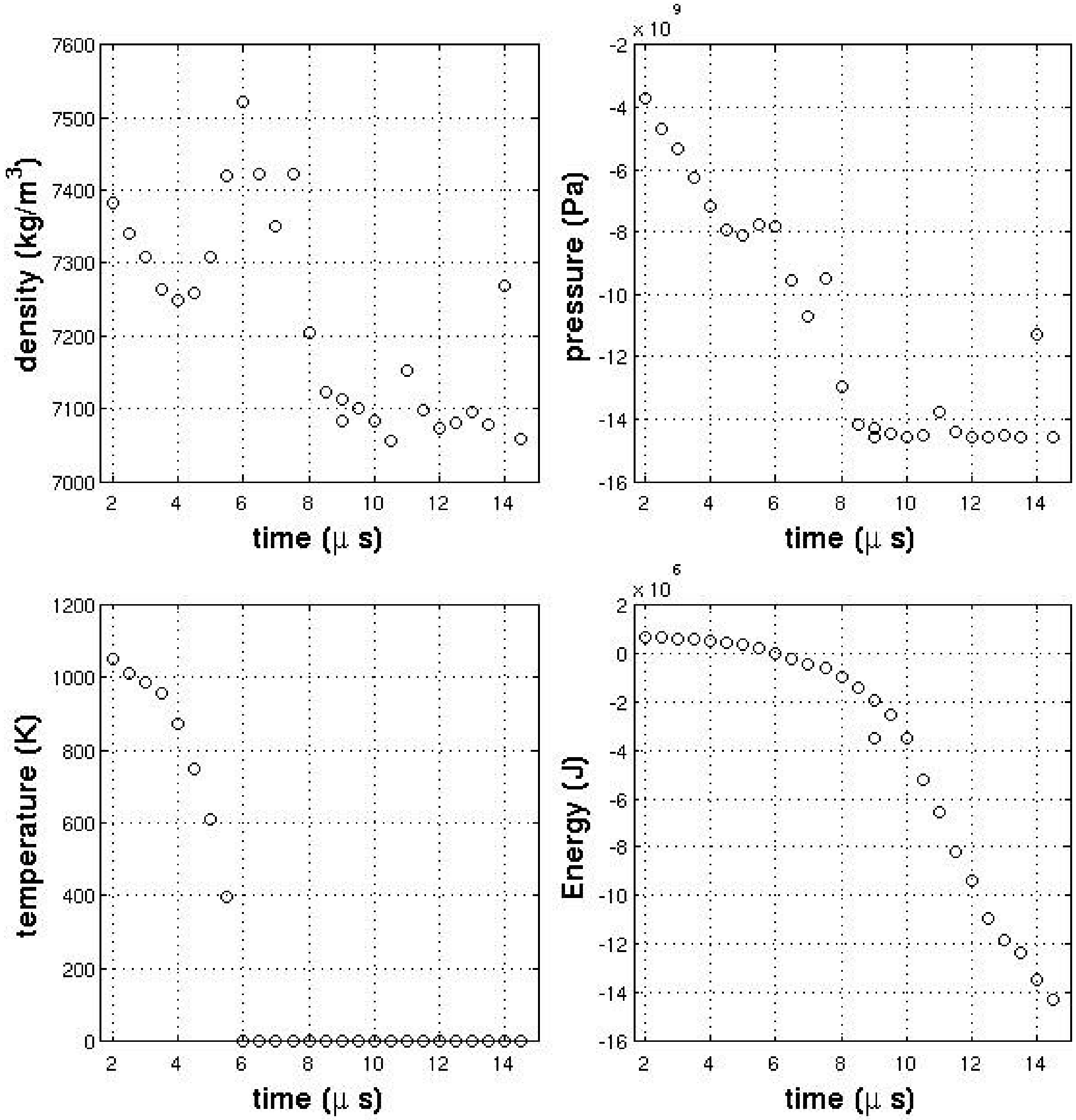

Figure A.11. Baseline particle separation: History of thermodynamic states of 4340 steel for separated particle

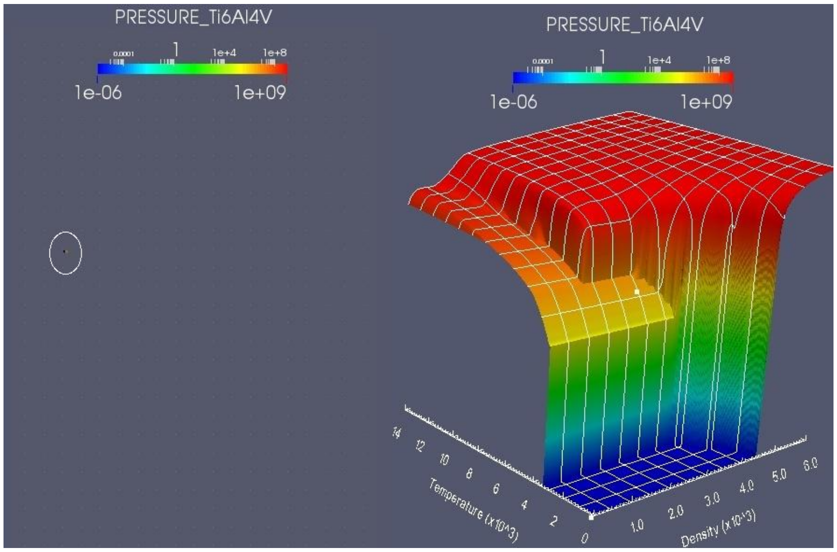

(a) moving particle

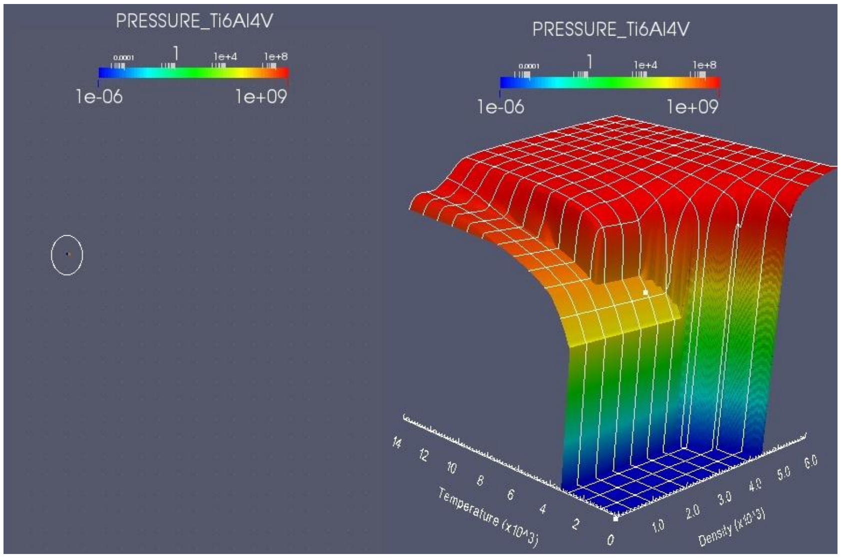

(b) static particle

Figure A.12. Baseline problem analysis of particle with initial thermodynamic state at separation: Comparison of results for static and moving particles at $2\mu s$

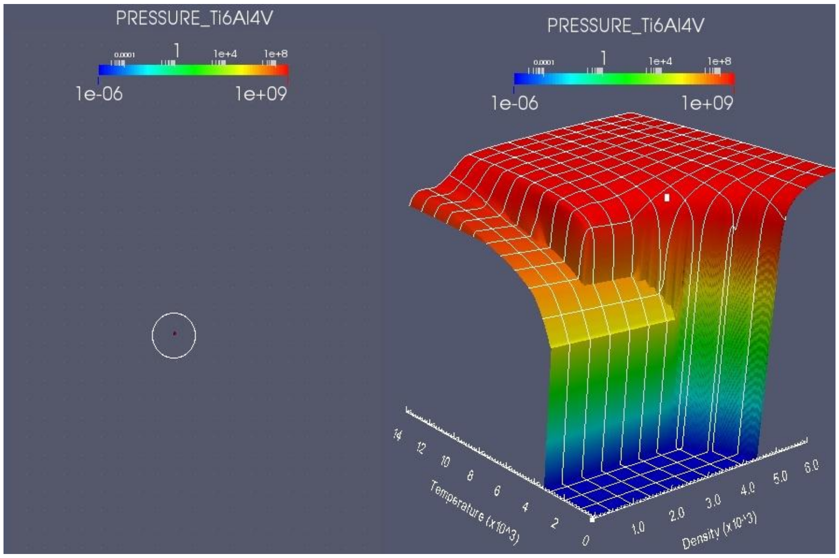

(a) moving particle

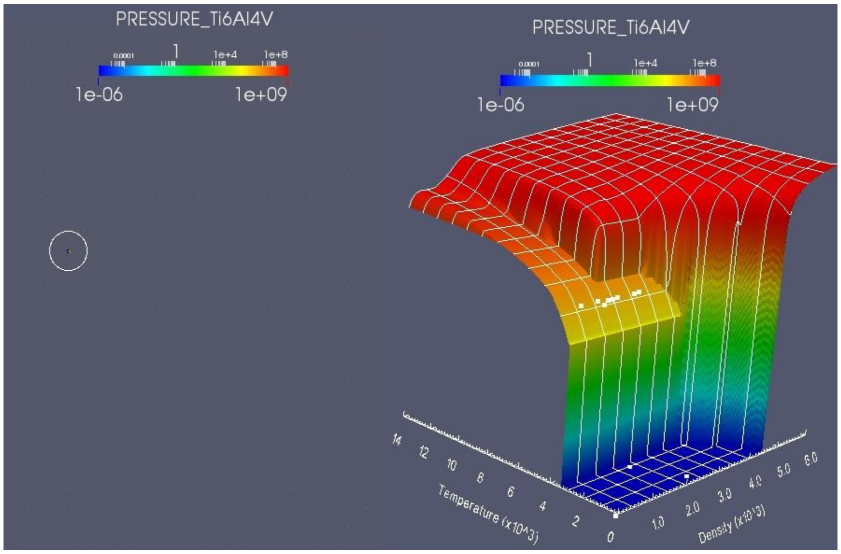

(b) static particle

Figure A.13. Baseline problem analysis of particle with initial thermodynamic state at separation: Comparison of results for static and moving particles at $7\mu s$

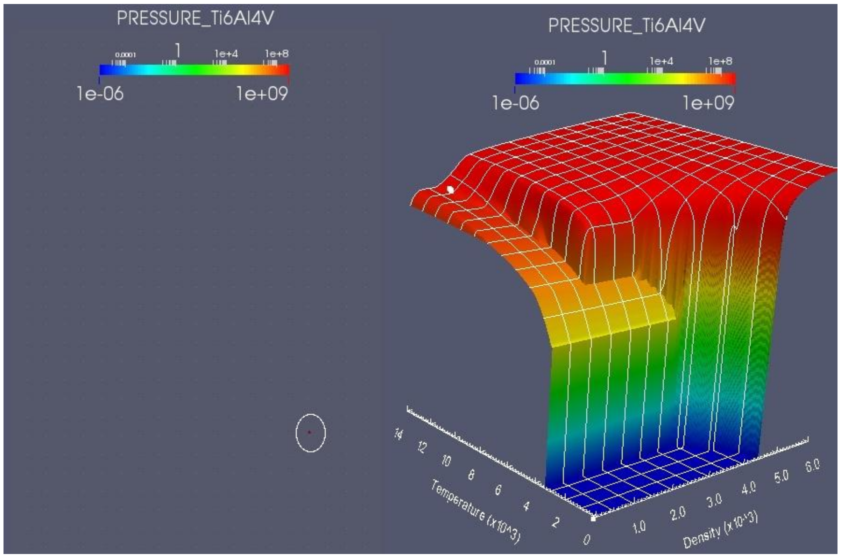

(a) moving particle

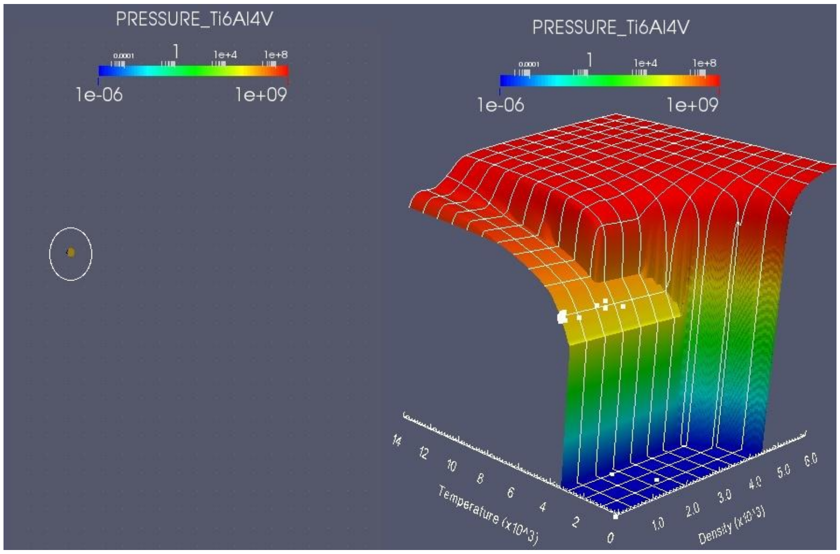

(b) static particle

Figure A.14. Baseline problem analysis of particle with initial thermodynamic state at separation: Comparison of results for static and moving particles at $13\mu s$

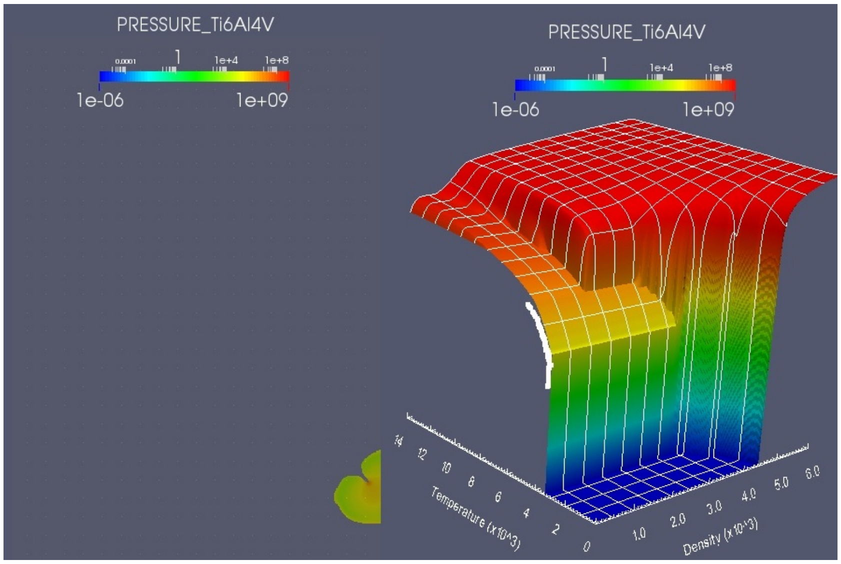

(a) moving particle

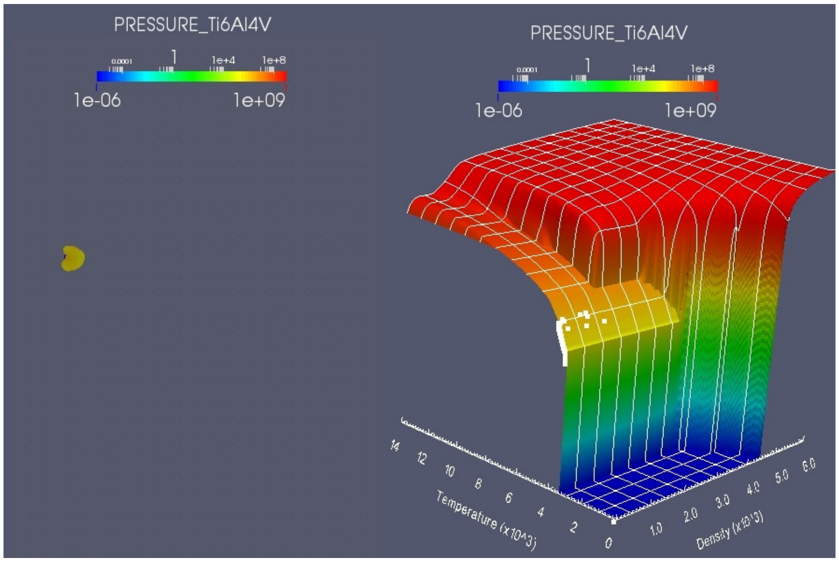

(b) static particle

Figure A.15. Baseline problem analysis of particle with initial thermodynamic state at separation: Comparison of results for static and moving particles at $16\mu s$

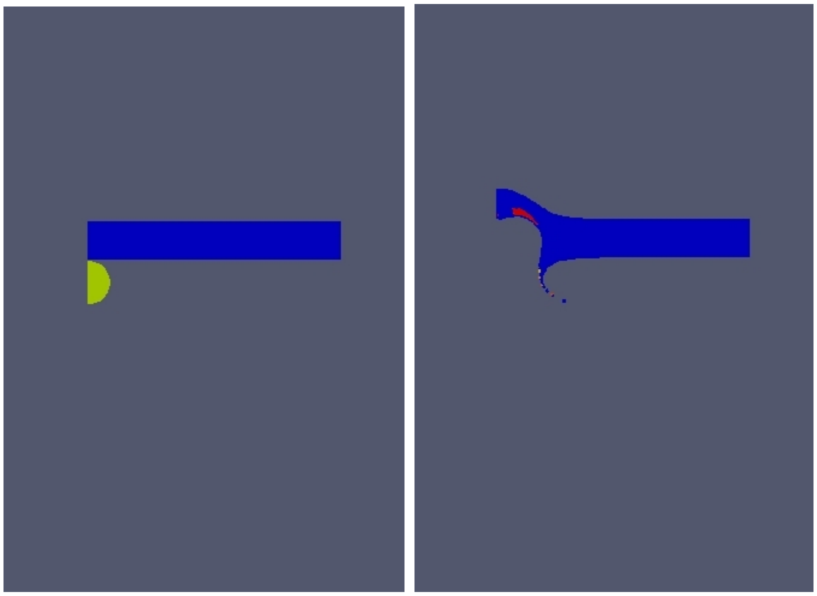

(a) initial configuration **(b)** t = 3 μs

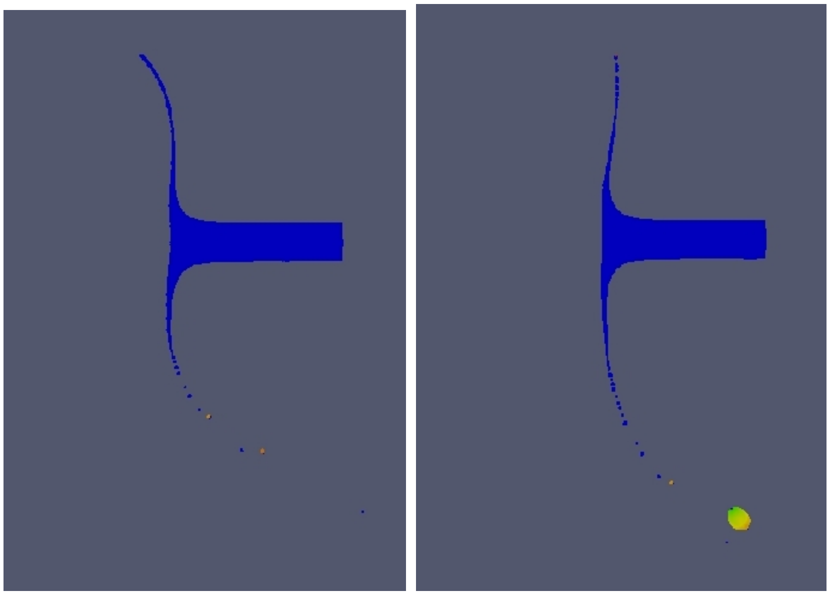

(c) t = 12.5 μs **(d)** t = 17.5 μs

Figure A.16. Baseline problems: Impact of a Copper sphere on a 4340 steel plate resulting in a Copper cloud formation

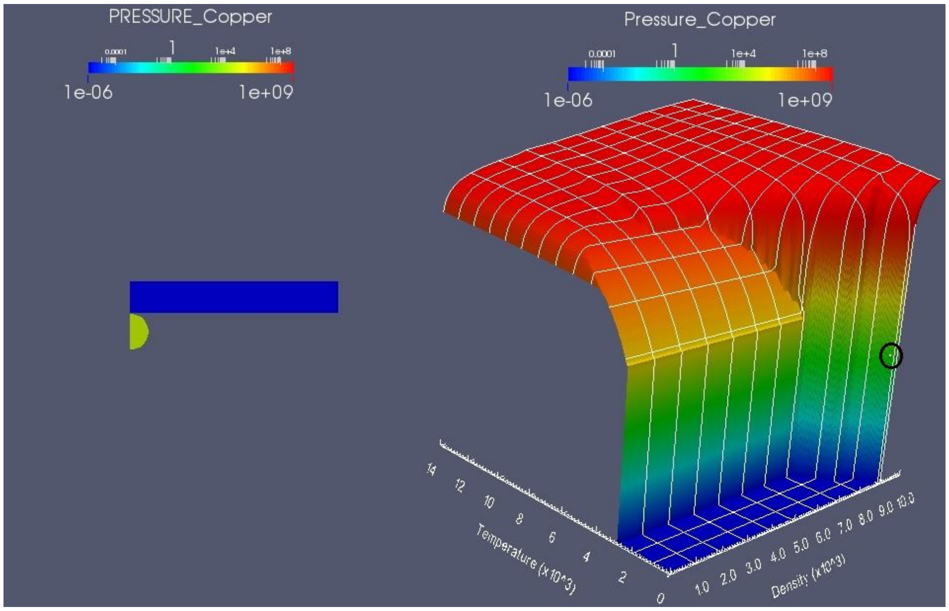

Figure A.17. Initial configuration & thermodynamic state

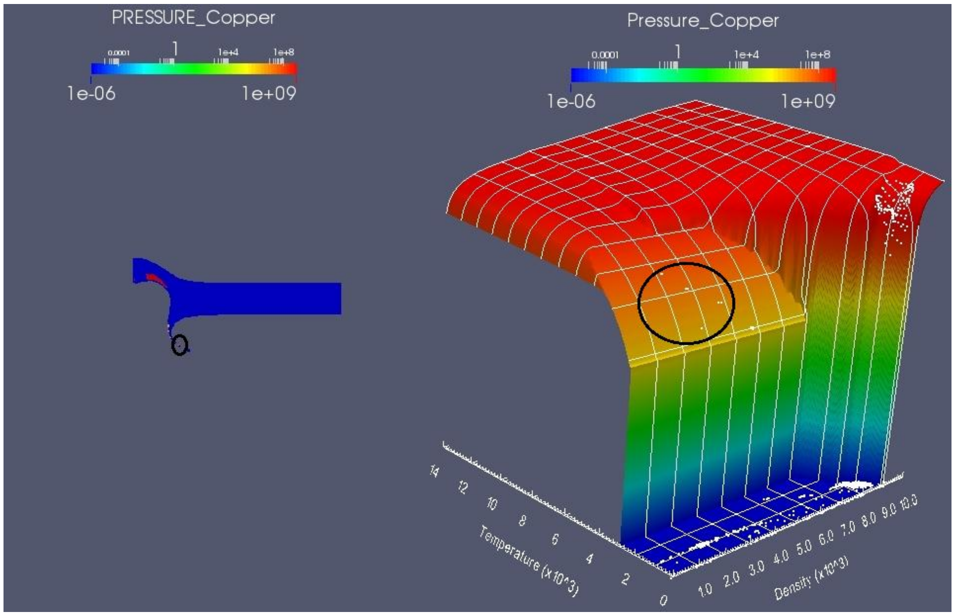

Figure A.18. $t = 2\mu s$: Separation of high pressure fragment

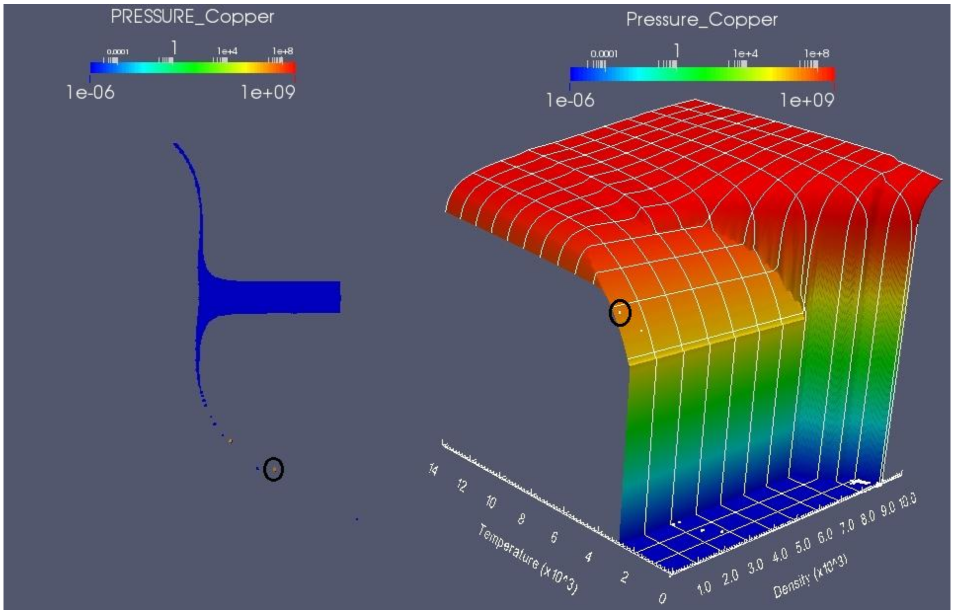

Figure A.19. $t = 12.5\mu s$: Rapid decrease in density

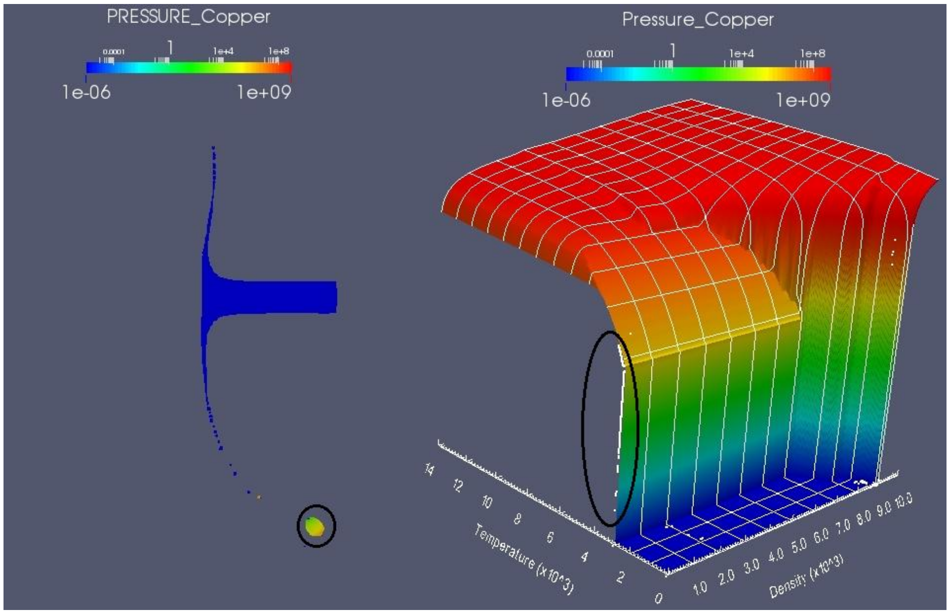

Figure A.20. $t = 17.5\mu s$: Rapid decrease in pressure & cloud formation

A.3 The Effect of Several Algorithmic ALEGRA Options on Cloud Formation

The effectiveness of several algorithmic options in ALEGRA for precluding the formation of clouds is explored. The options were chosen based on the past experience of developers, analysts and users of ALEGRA who encountered a cloud formation event and used one or more input options to prevent its occurrence. The goals of this study are to understand why the use of one or a combination of several ALEGRA input options prevents cloud formation. The algorithmic options considered in this study include the specification of r_{min} for tabular equations of state, the suppression of void compression for multi-material cell treatment of volume fraction computation, and forcing a material to fracture by insertion of void into an element once a lower material density bound is attained.

A.3.1 Specifying a Minimum Density Threshold for the Tension Regions of Tabular Equations of State, (Setting r_{min})

Tabular equations of state that consider regions of tension (negative pressure) in solid materials are commonly used. The treatment of a tensile state is intimately tied to the parameter, r_{min}, defined as the lower bound of material density in the tensile region below which pressure is set to a zero value. The value of r_{min} can be specified for a material by the user within a tabular equation of state input statement. If r_{min} is not specified, an r_{min} value of 80% of the solid material density value is used as default. It is important to note that r_{min} only applies to the tensile region of the tabular equation of state.

Figure A.21 displays the tabular equation of state surface for 4340 steel with the default r_{min} value and a prescribed $r_{min} = 7089.1 Kg/cm^3$. The difference between the resulting tension regions is very noticeable. The equation of state associated with the default r_{min} allows for lower density tensile states of material than that of the equation of state with a prescribed r_{min}. Recall that the baseline problem results in a mixed-material particle with Ti6Al4V in compression and 4340 steel in tension. Since only the steel contribution obtains a tensile state, the sphere impact problem is analyzed by setting r_{min} for steel only.

Figure A.22 displays the separation of the mixed-material particle and its corresponding thermodynamic state. Like the baseline case, the Ti6Al4V particle material is in a mixed liquid-vapor state. However, instead of the formation of a vapor cloud, the Ti6Al4V experiences a rapid pressure drop to zero at a later time (Figure A.23). Thermodynamic state histories for both Ti6Al4V and steel are displayed in Figures A.24-A.27. Separated particle histories in Figures A.26 and A.27 show the sudden pressure drop for the Ti6Al4V particle material and the zero pressure state of the 4340 steel. The modified value of r_{min} for steel results in a completely different thermodynamic state path for which Ti6Al4V cloud formation does not occur.

Although cloud formation is avoided, the result is unphysical given the state of Ti6Al4V material in the separated particle. In this case a clould should form. This is demonstrated by a static particle analysis of the problem with initial thermodynamic state corresponding to Figure A.22. The Ti6Al4V material in the motionless fragment naturally expands into vapor. Again, the interaction of the two materials due to motion is responsible for the unphysical path observed, only this time, a cloud does not form.

Results for a copper sphere projectile and $r_{min} = 7089.1Kg/cm^3$ for steel are displayed in Figures A.28 and A.29. The state of the copper material of the separated particle lies in the liquid-vapor region (Figure A.28). However, a cloud of copper eventually forms, as expected (Figure A.29). The use of a user prescribed r_{min} does not guarantee that clouds of vapor will not appear.

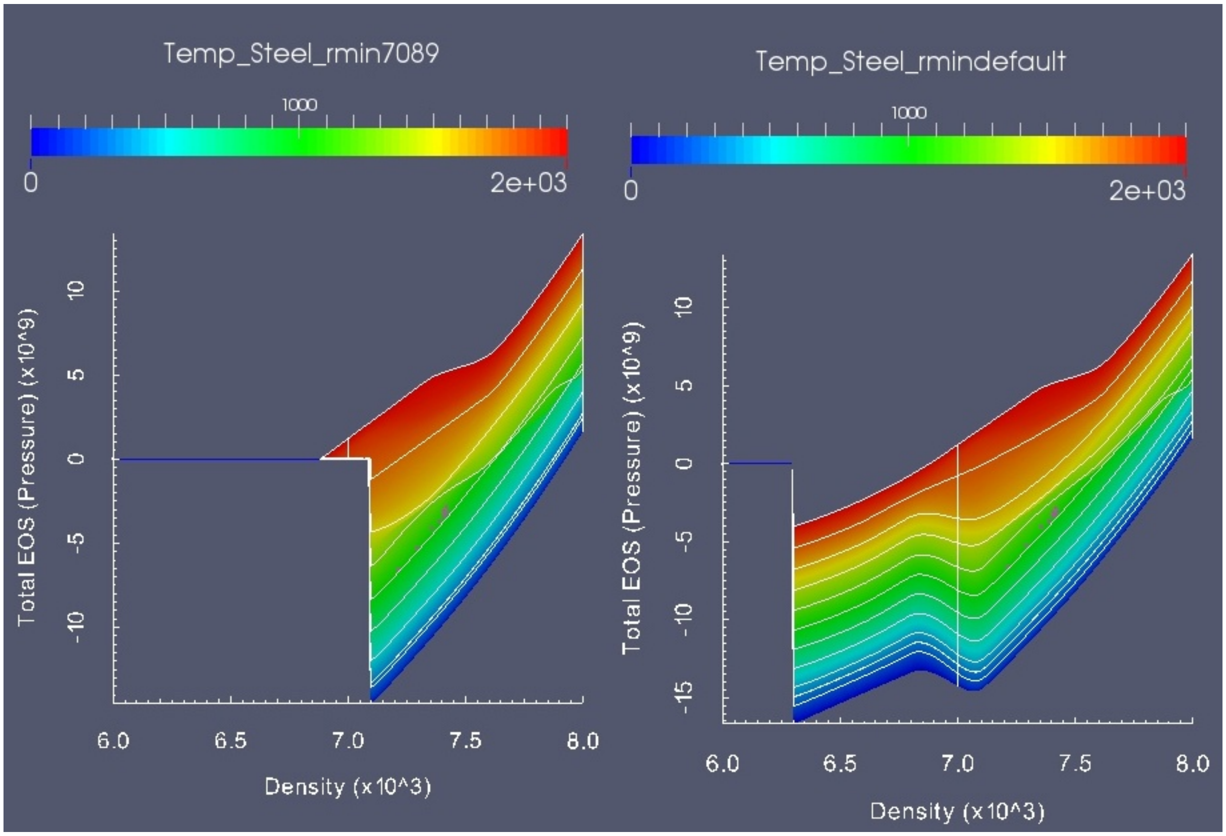

Figure A.21. 4340 steel EOS for default (right) and prescribed (left) r_{min}

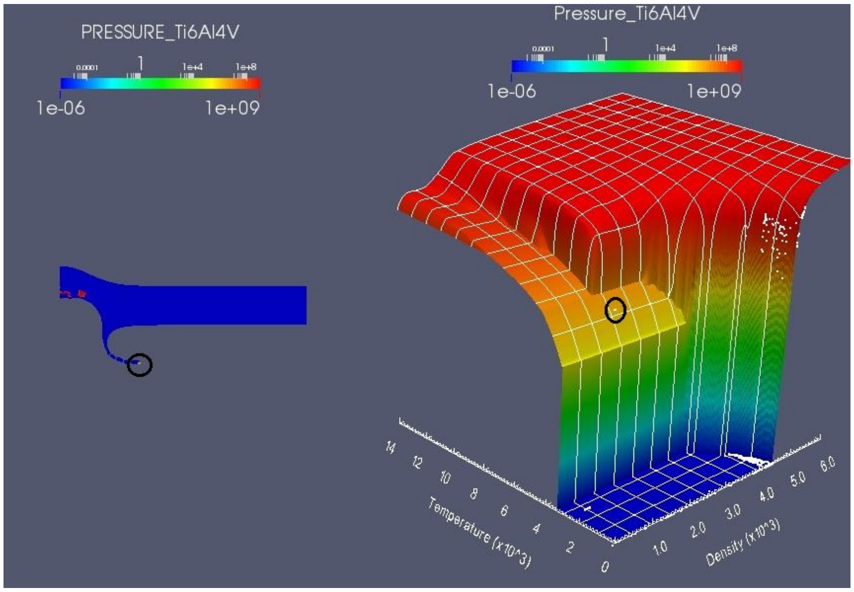

Figure A.22. $t = 3\mu s$: Separation of high pressure fragment

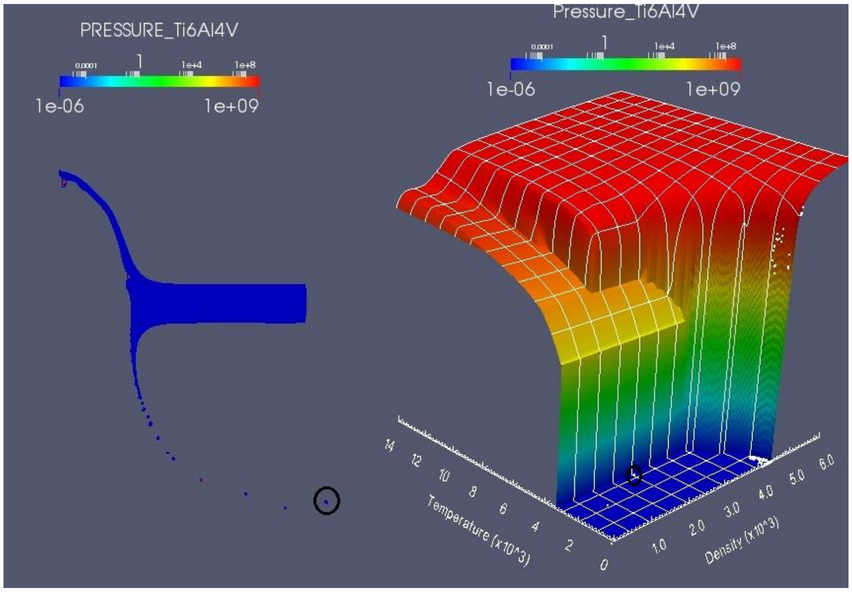

Figure A.23. $t = 12\mu s$: Rapid decrease in pressure

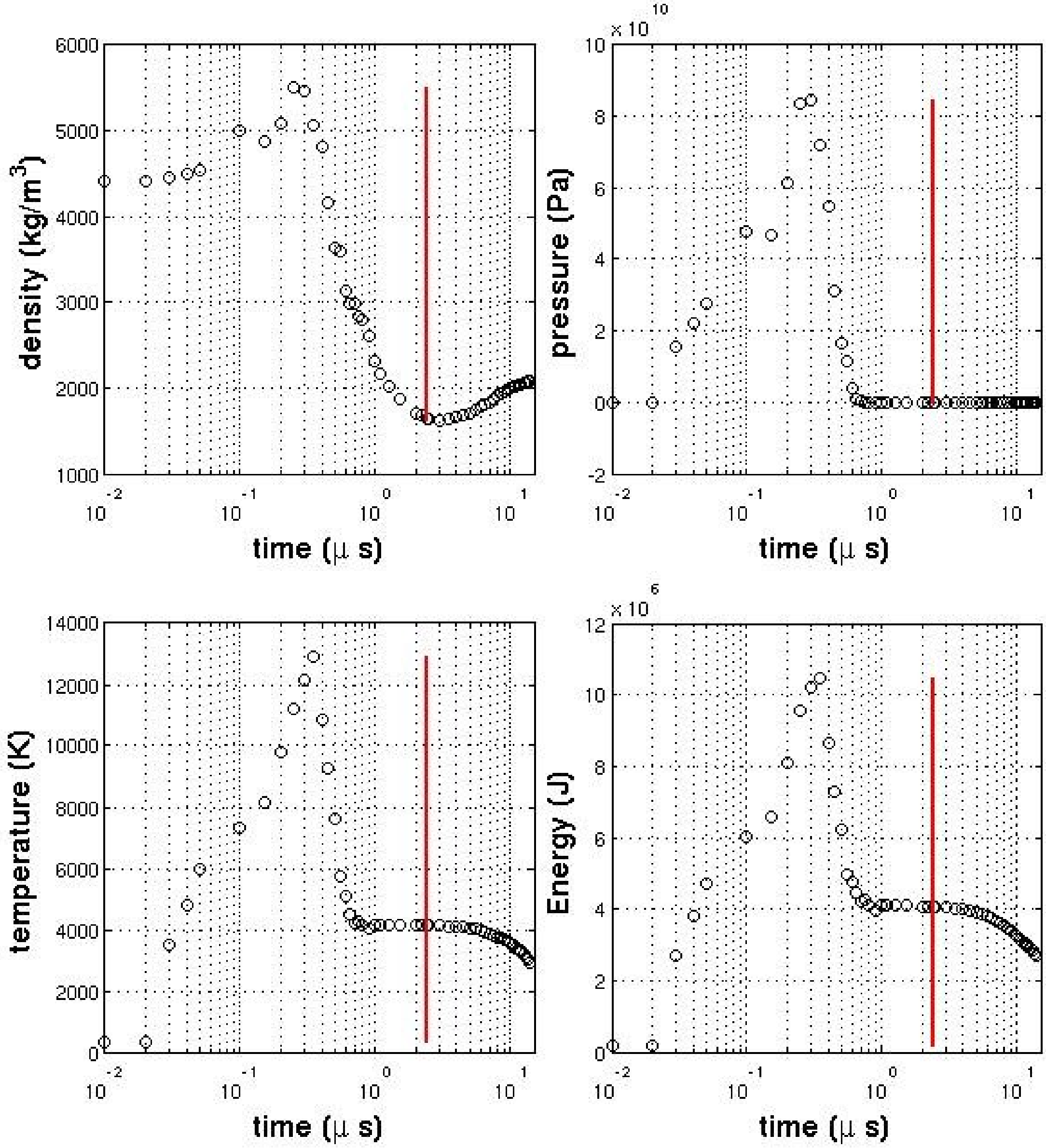

Figure A.24. 4340 steel r_{min}: History of thermodynamic states of Ti6Al4V

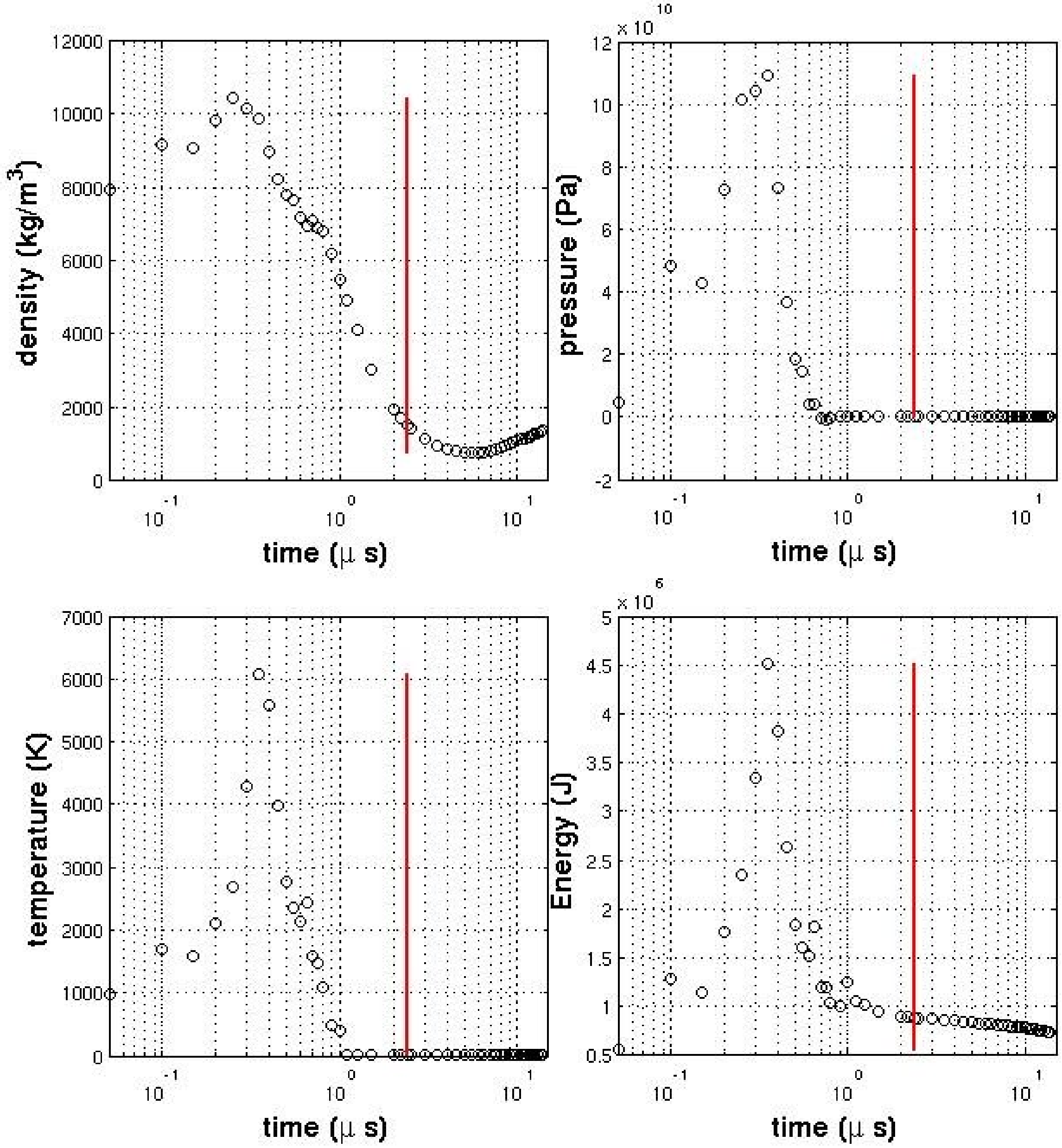

Figure A.25. 4340 steel r_{min}: History of thermodynamic states of 4340 steel

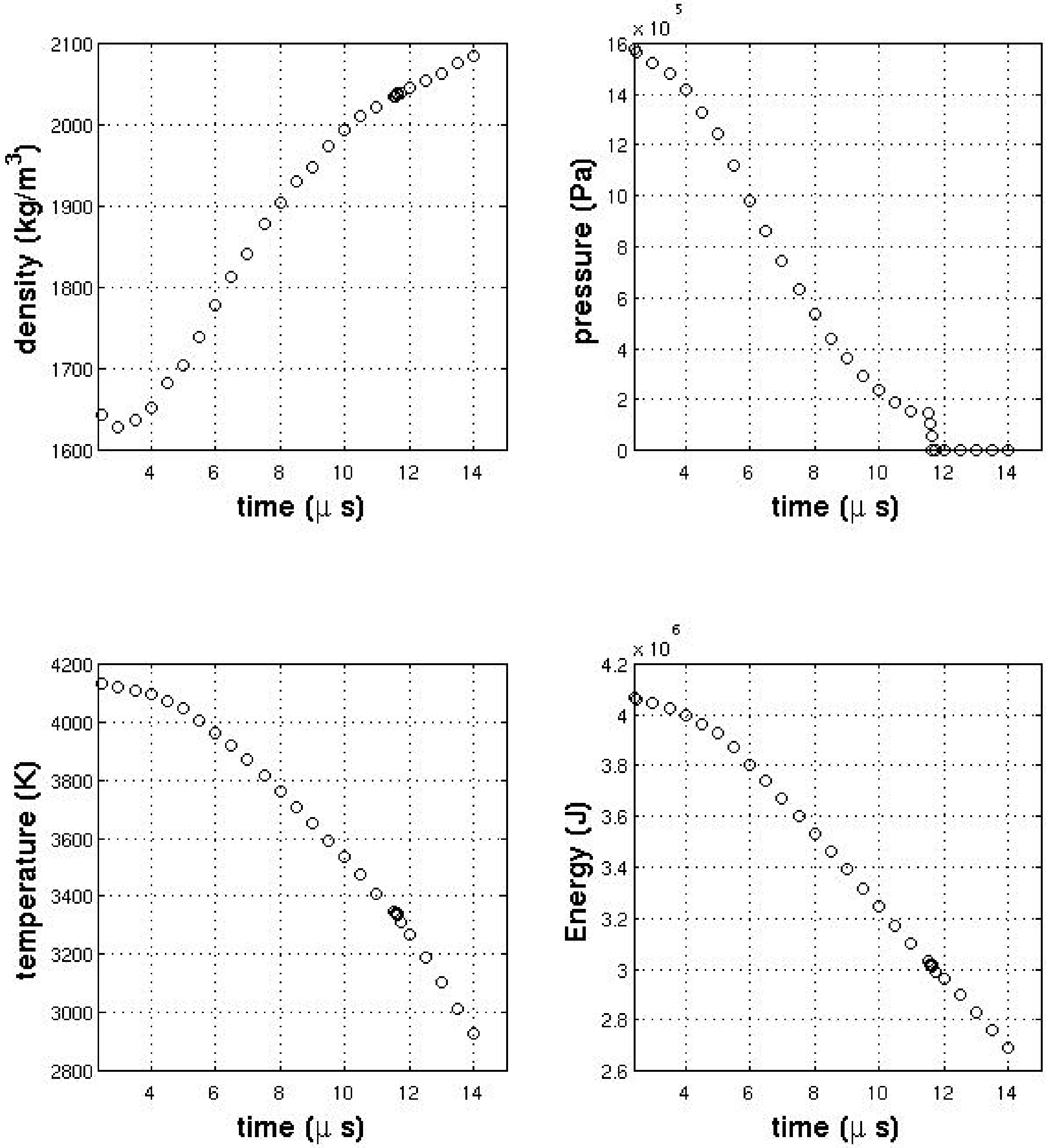

Figure A.26. 4340 steel r_{min}: History of thermodynamic states of Ti6Al4V for separated particle

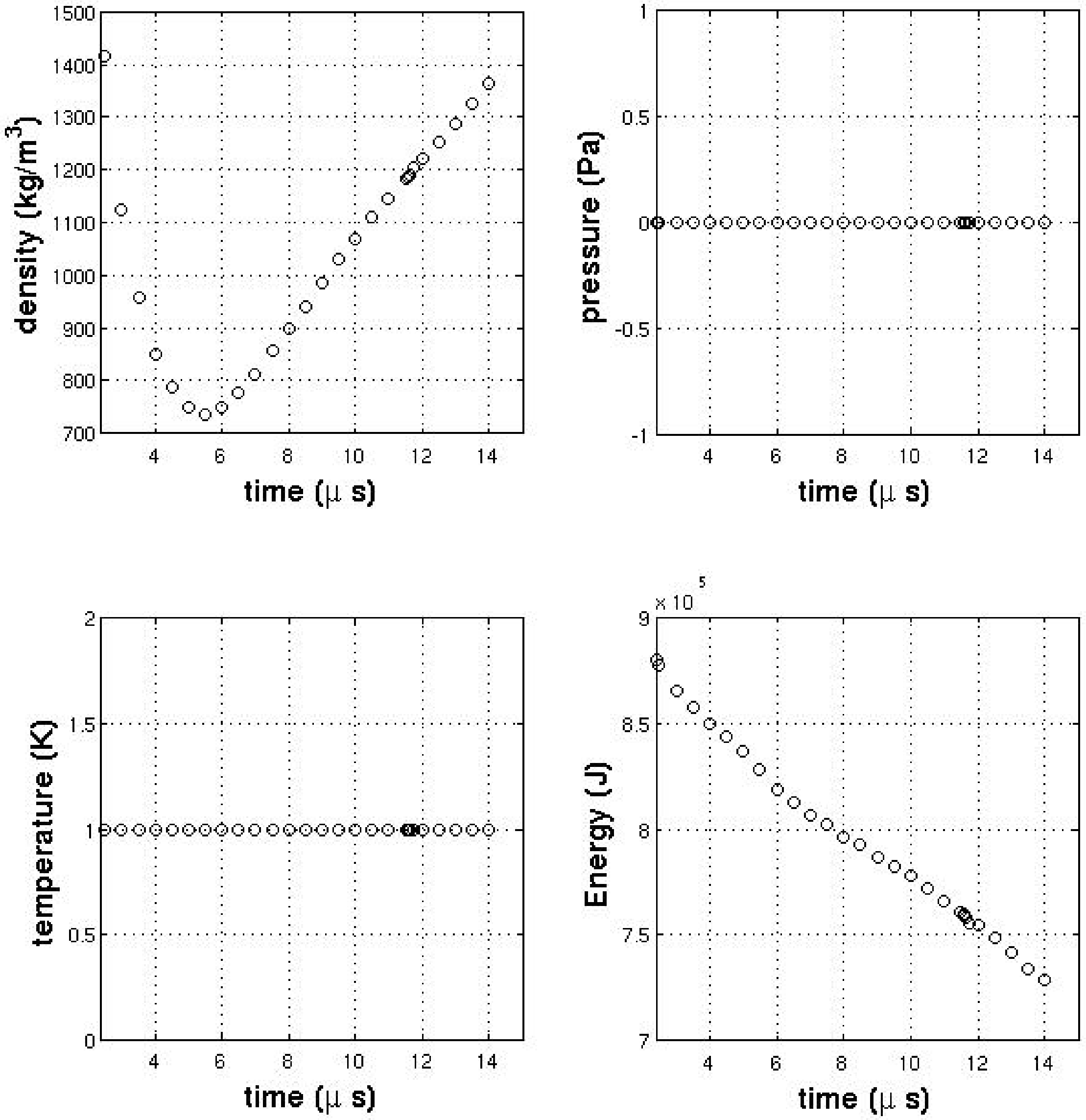

Figure A.27. 4340 steel r_{min}: History of thermodynamic states of 4340 steel for separated particle

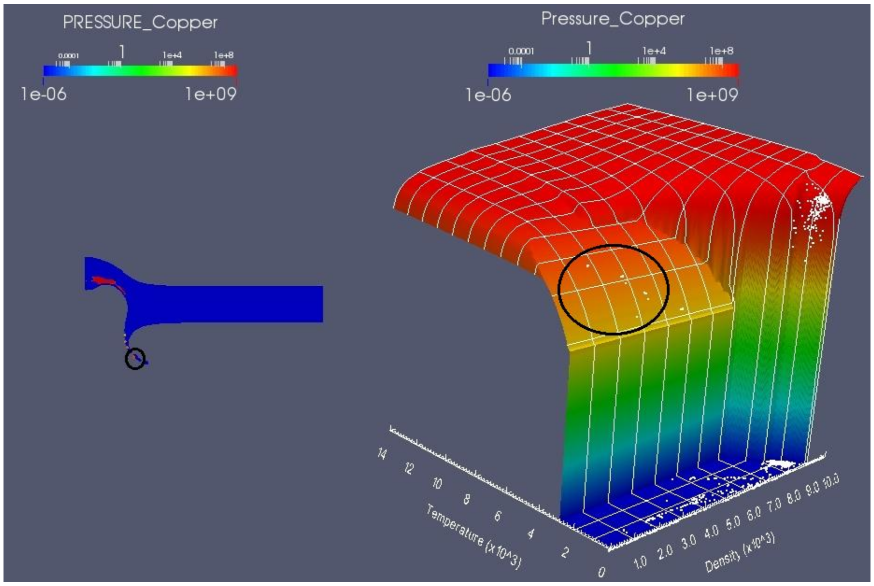

Figure A.28. $t = 3\mu s$: Separation of high pressure fragment

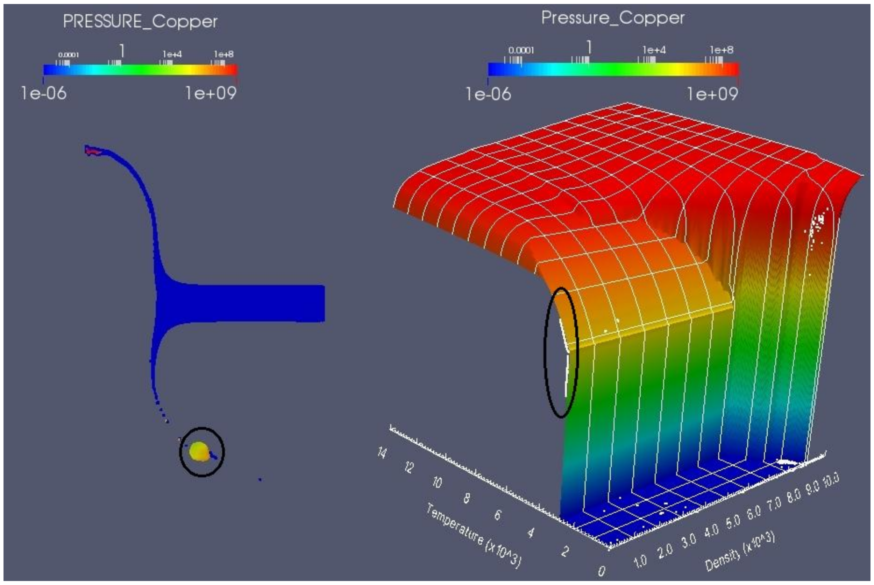

Figure A.29. $t = 10\mu s$: Rapid decrease in pressure & cloud formation

A.3.2 Suppression of Void Compression for Multi-material Treatment

The isentropic multi-material volume fraction update algorithm is used to treat multiple material cells in ALEGRA. The algorithm adjusts the volume fractions of material within a cell by accounting for the relative compressibility of each material. In addition, the algorithm treats void separately before computing volume fractions of real materials. If compression of an element is detected the void within that element is partially or completely compressed before the compression of the actual materials is addressed. This effectively increases the volume fractions of real material. The void compression feature is intended mostly for applications of multi-body impact that occur within an element, for which the void between two bodies must be compressed prior to impact. For many problems, void compression provides a proper physical treatment. However, for some problems this treatment of void has been known to produce unphysical results, and since the sphere impact problem involves mixed-material particles moving through void, it is only natural to study the effect of void compression. Currently, there is no option to turn off void compression when using the default isentropic multi-material volume fraction update algorithm. In order to perform this part of the study, the sphere impact problem was simulated using a custom built version of ALEGRA for which void compression is bypassed.

Figure A.30 displays the thermodynamic state of the Ti6Al4V component of the particle upon separation. The zero pressure state does not lie in a mixed liquid-vapor phase for which a natural expansion would occur. As the particle travels through space, the solid Ti6Al4V material experiences an unexpected drastic pressure increase (Figure A.31) and remains at this high pressure state throughout the remainder of the simulation (Figure A.32). Results for the sphere impact problem with a copper projectile display a different behavior. The copper in the separated particle is a mixed liquid-vapor state (Figure A.33). Instead of expanding, a sudden pressure drop occurs (Figure A.34) similar to that observed in Figures A.22-A.23 for the case of Ti6Al4V with a prescribed r_{min} for steel. Elimination of void compression effects failed to produce physical results for both Ti6Al4V and copper spherical projectile fragments.

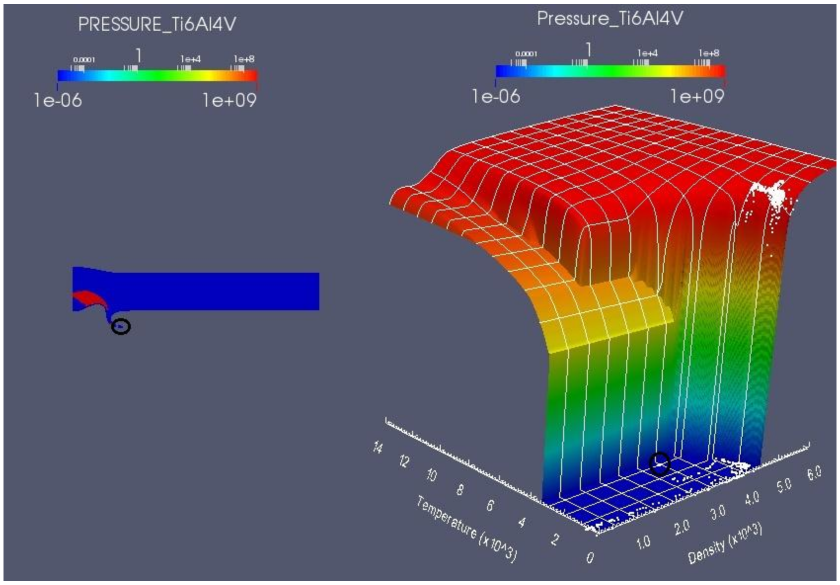

Figure A.30. $t = 1.6\mu s$: Separation of low pressure fragment

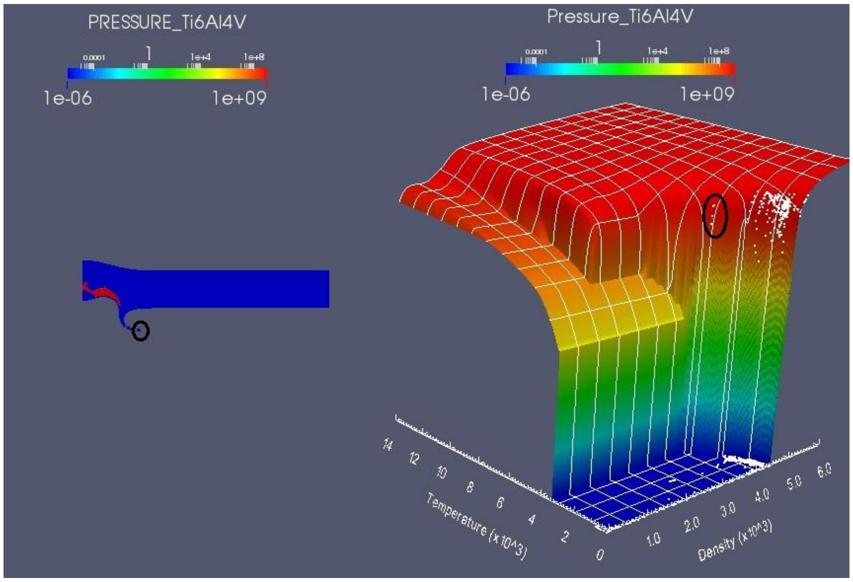

Figure A.31. $t = 2\mu s$: Rapid increase in fragment pressure

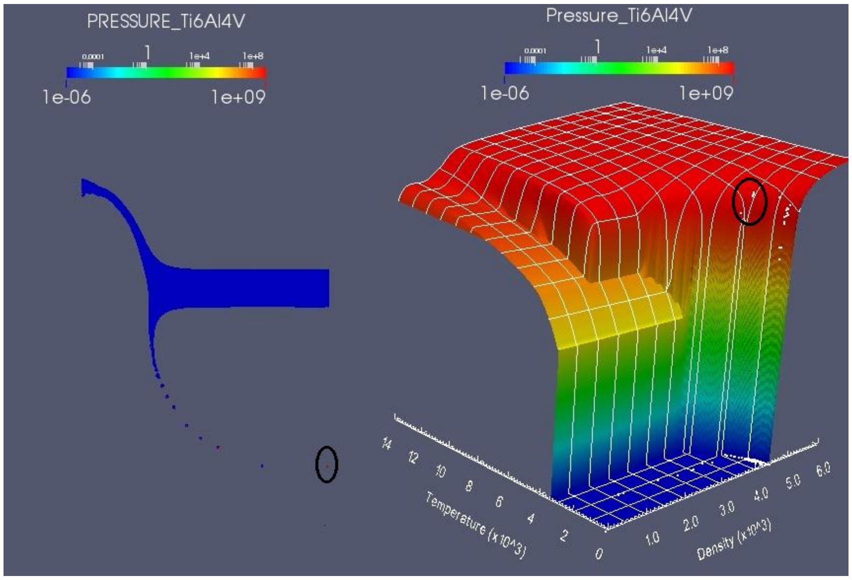

Figure A.32. $t = 10\mu s$: Stable pressure of fragment

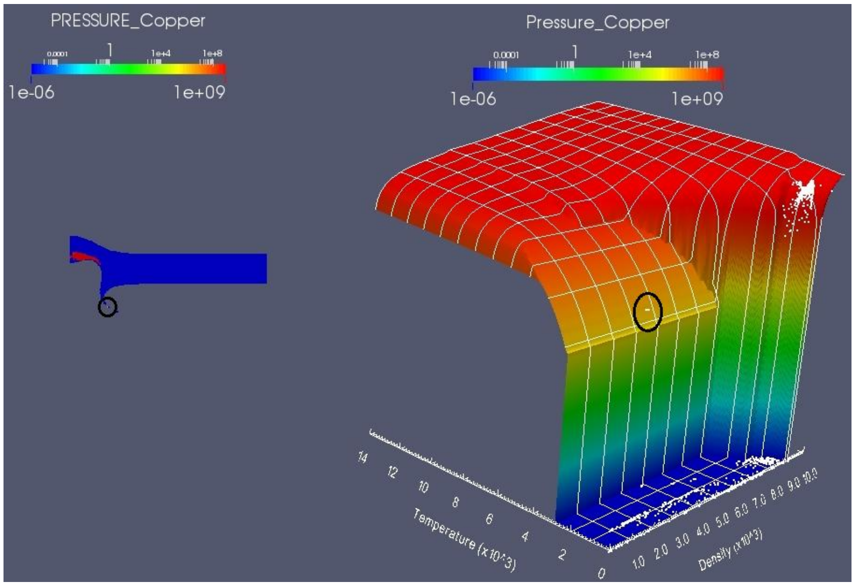

Figure A.33. $t = 2.5\mu s$: Separation of low pressure fragment

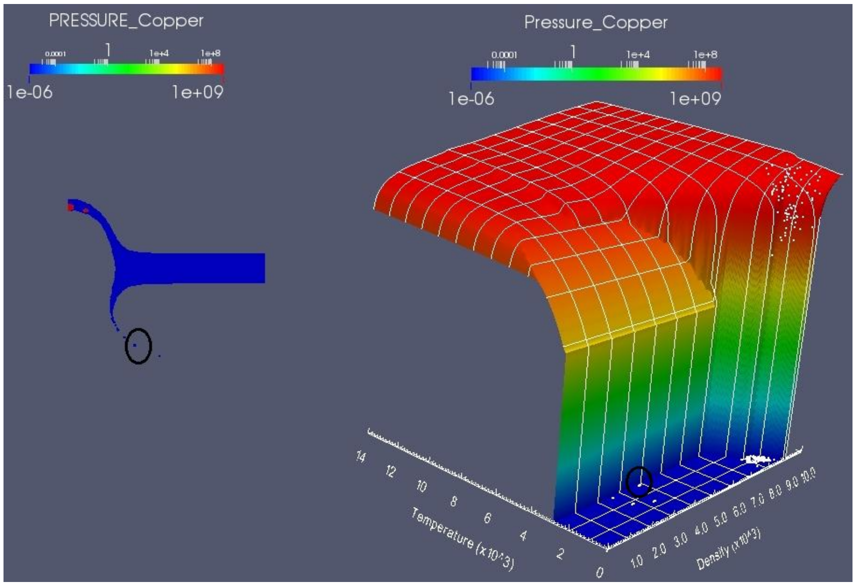

Figure A.34. $t = 5.5\mu s$: Rapid decrease in fragment pressure

A.3.3 Simulation of Material Failure Using Void Insertion with a Material Density Lower Bound (Force Fracture)

The simulation of mode I (tensile) failure of solid material in ALEGRA is performed using the void insertion feature. Solid dynamics problems that incorporate material failure rely on a fracture pressure (ultimate tensile strength) criterion for the initiation of void insertion. Once the material in an element reaches the prescribed value of fracture pressure, void material is inserted into the cell in order to relax the pressure to a zero value. During this process the volume fraction of the material is reduced due to the introduced void volume, effectively increasing the material density. One void insertion option is to provide a minimum material density criterion in addition to the fracture pressure. This is done by specifying the force fracture option. A minimum density value can be prescribed or a value of r_{min} for the tabular equation of state is used by default. Once the material in a cell reaches the lower bound density value, void is inserted in order to sustain the minimum density.

Simulation results incorporating void insertion with the force fracture option for the sphere impact problem are displayed in Figures A.35-A.36 and Figures A.37-A.38 for Ti6Al4V and copper projectiles respectively. At no time does either material enter the mixed liquid-vapor state that leads to cloud formation. The phase change is simply disallowed by the lower density bound imposed by the force fracture option. The comparison of these results with the baseline case for Ti6Al4V is displayed in Figures A.39-A.41. Upon release from the initial shock loading, the separating material undergoes a thermodynamic state path of decreasing density and temperature (Figure A.39). The material is released into a liquid-vapor phase in the baseline case (Figure A.40a), while the minimum density limit of $\approx 3500 km/m^3$ is reached for the case of void insertion with force fracture (Figure A.40b), preventing a phase change from the solid state. This same behavior is also observed for the case of a copper projectile (Figures A.42-A.44). Use of void insertion with the force fracture option will completely preclude cloud formation, however the thermodynamic state path is altered by an arbitrary minimum value of density, for which there is no physical basis. Both KEOS and KANDC tabular equation of state interpreters were utilized for this part of the study; yielding nearly identical results.

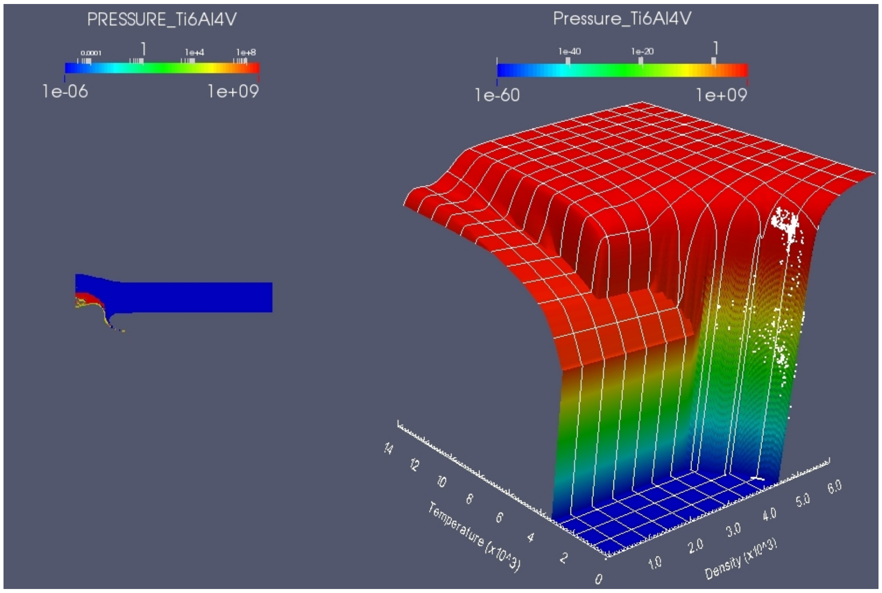

Figure A.35. $t = 2\mu s$: Separation of fragment

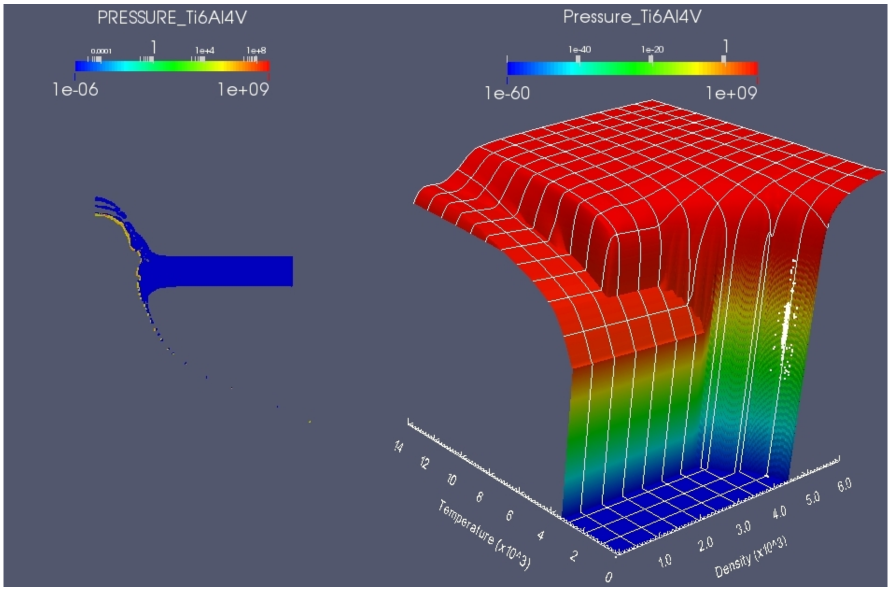

Figure A.36. $t = 8\mu s$: Debris Cloud of Solid Fragments

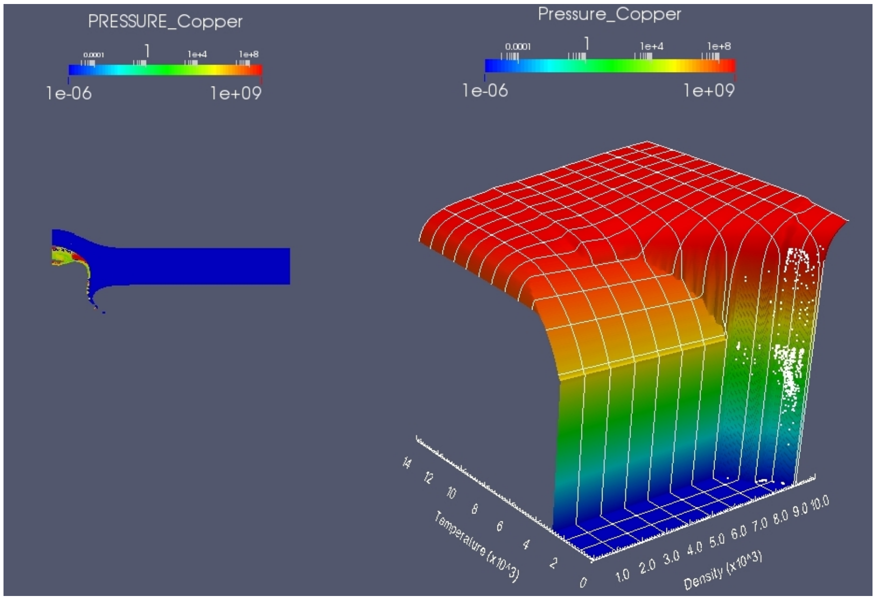

Figure A.37. $t = 2.25\mu s$: Separation of fragment

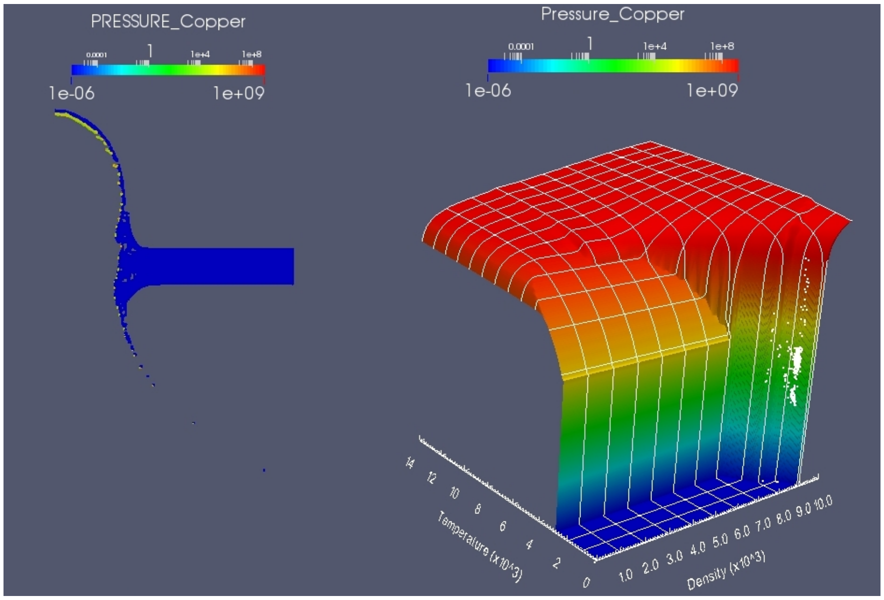

Figure A.38. $t = 10\mu s$: Debris Cloud of Solid Fragments

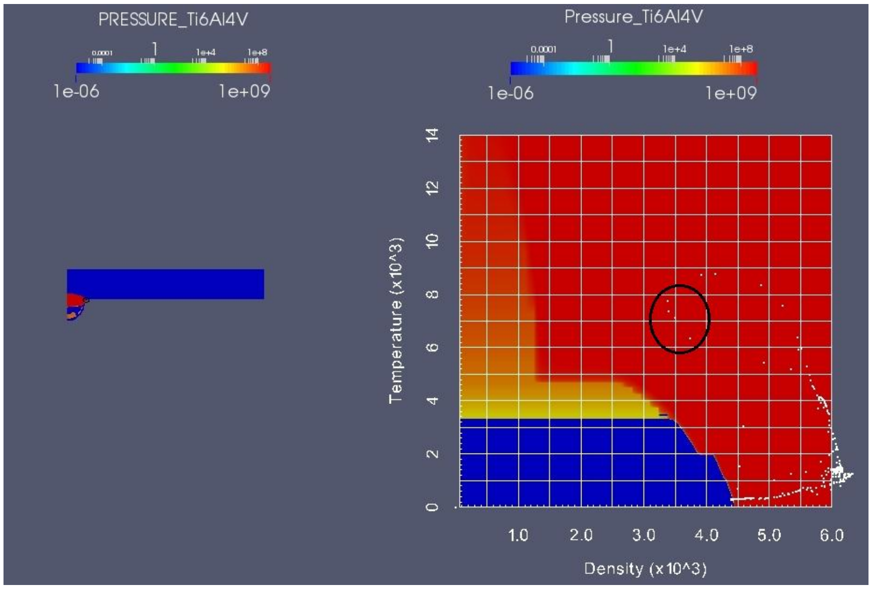

(a) baseline

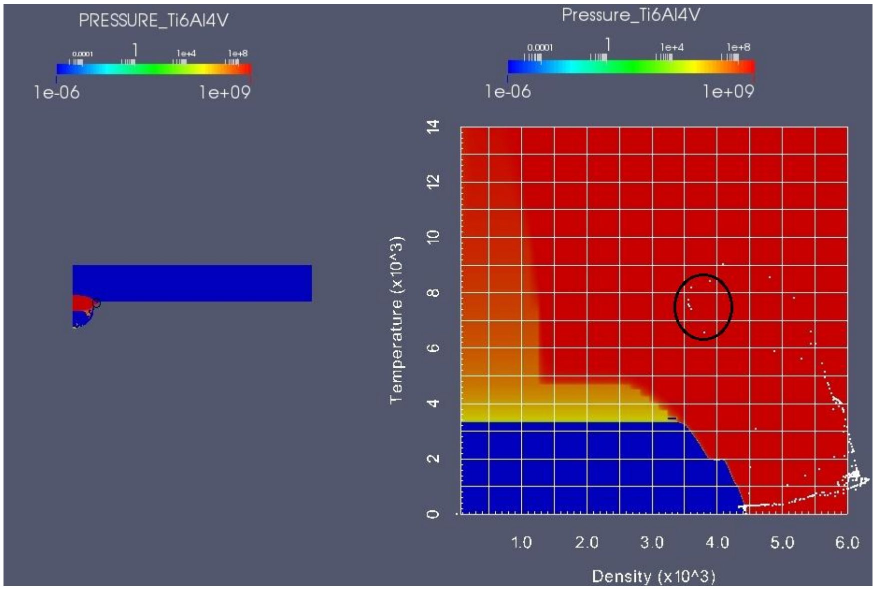

(b) force fracture

Figure A.39. Comparison: t = 0.5 μs

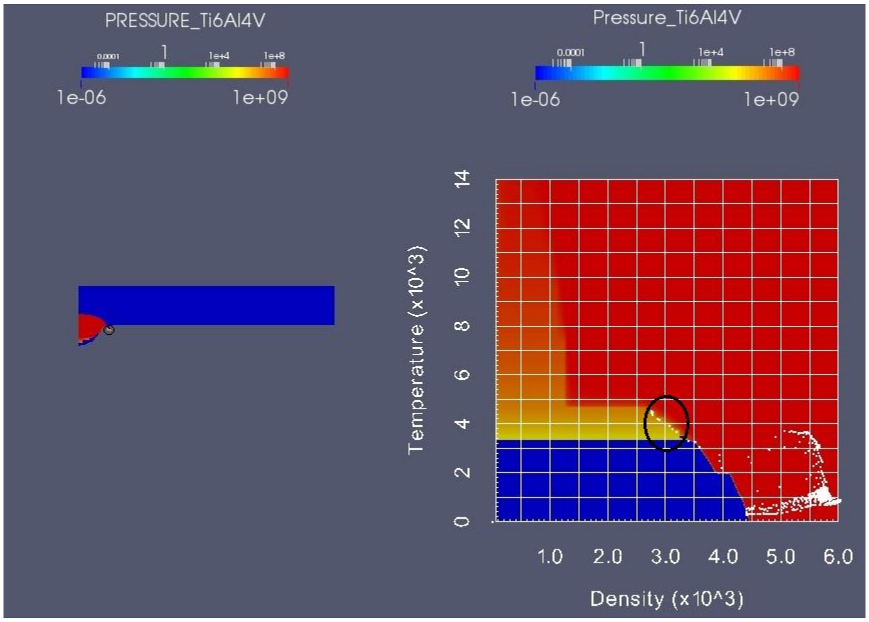

(a) baseline

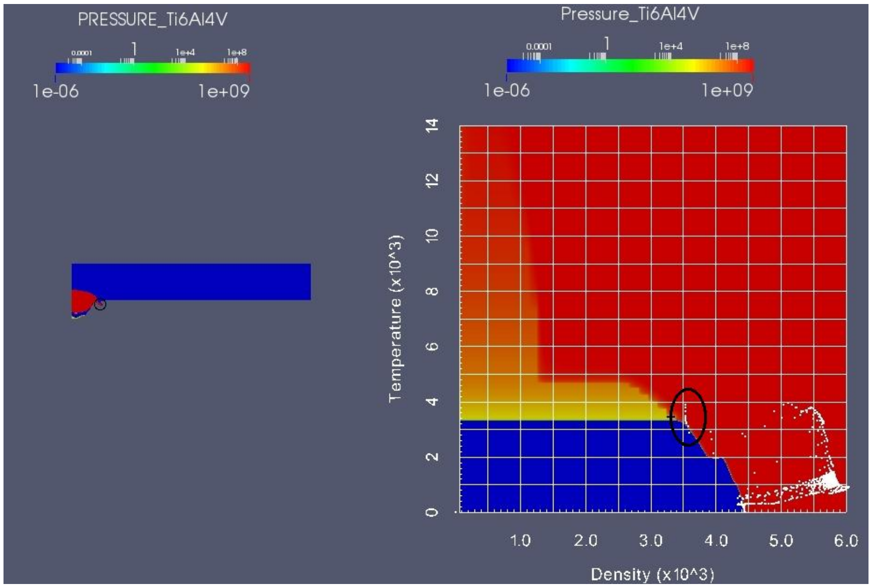

(b) force fracture

Figure A.40. Comparison: t = 0.75 μs

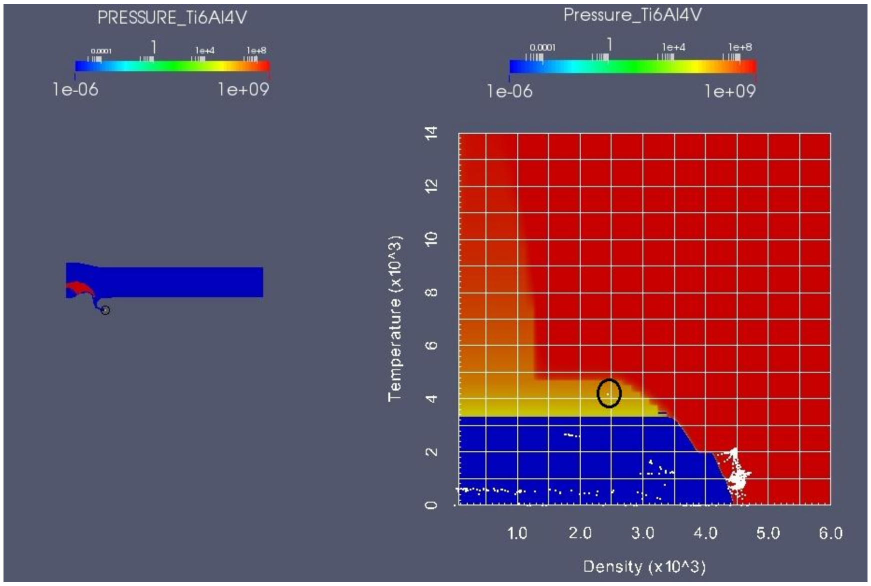

(a) baseline

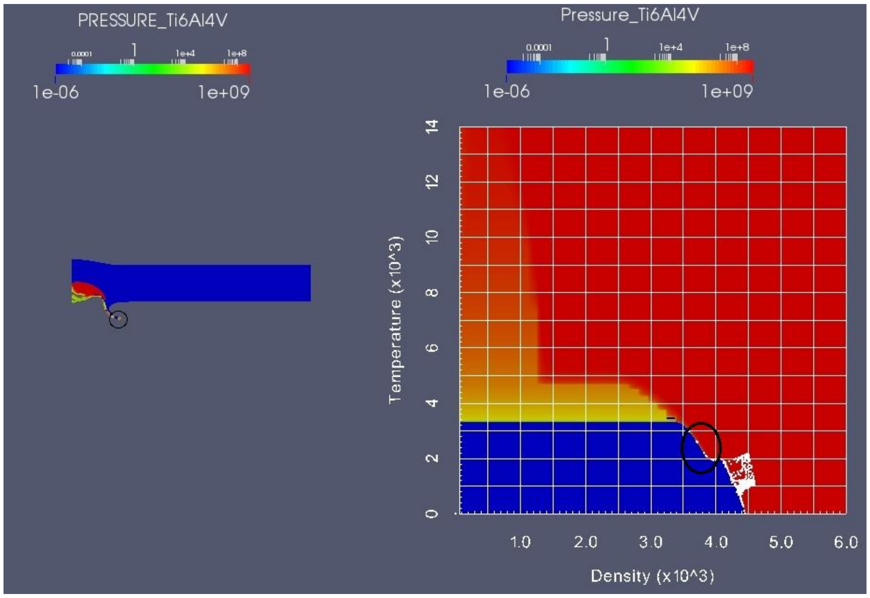

(b) force fracture

Figure A.41. Comparison: t = 1.6 μs

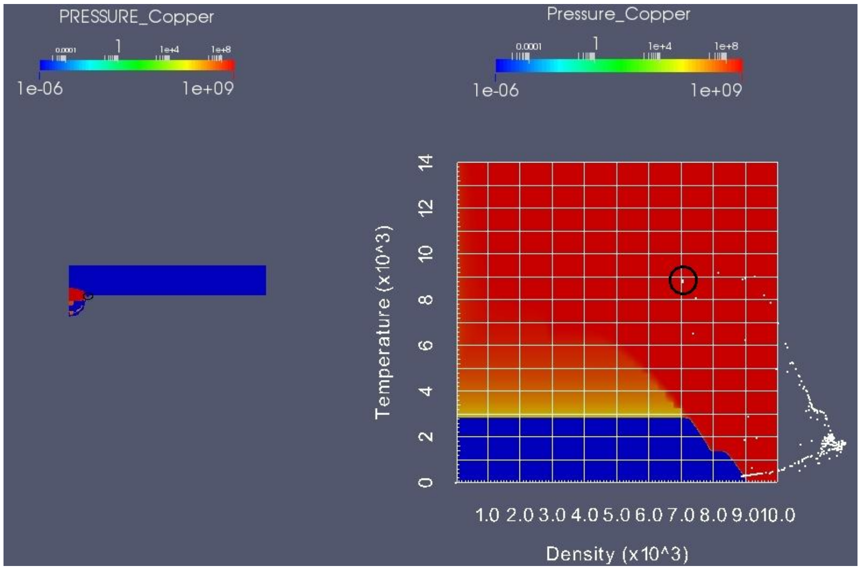

(a) baseline

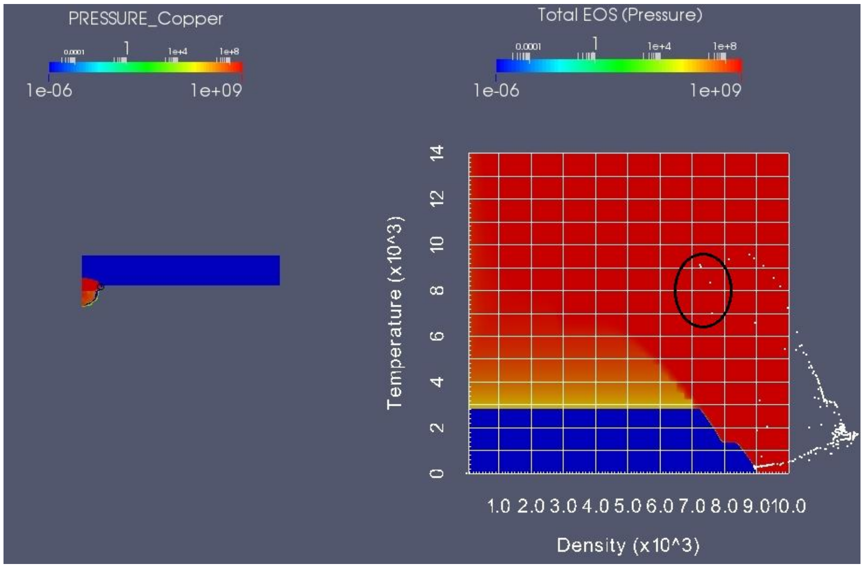

(b) force fracture

Figure A.42. Comparison: t = 0.5 μs

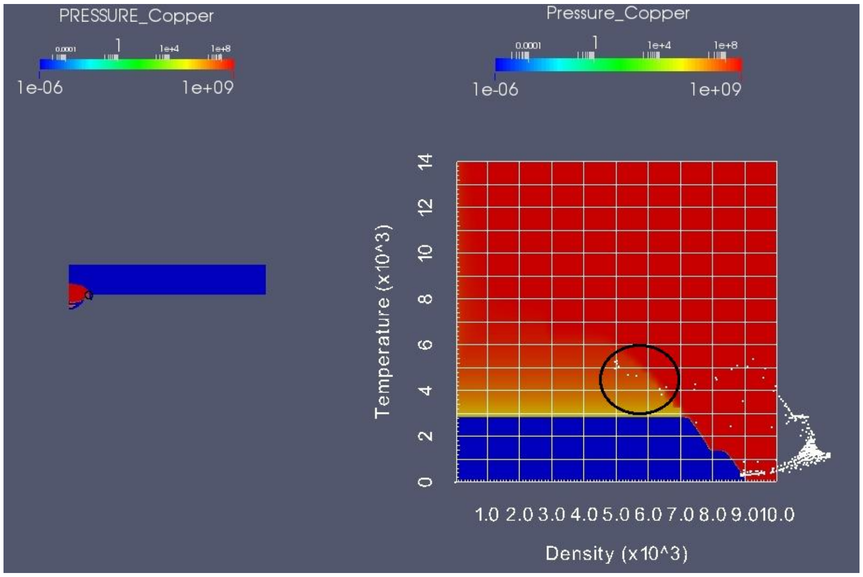

(a) baseline

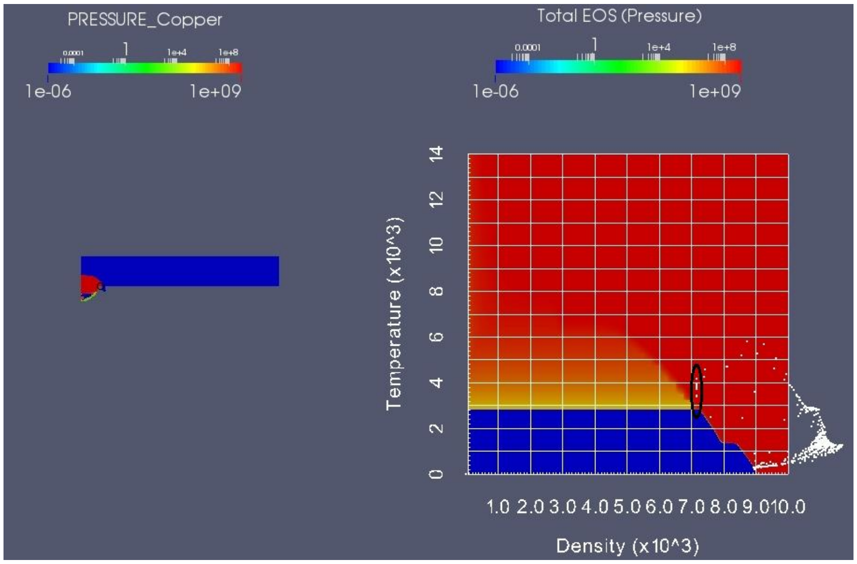

(b) force fracture

Figure A.43. Comparison: t = 0.75 μs

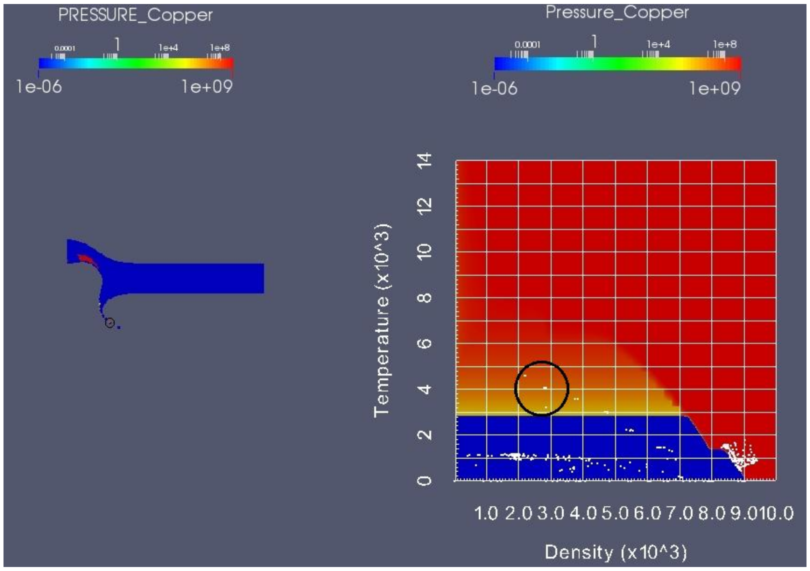

(a) baseline

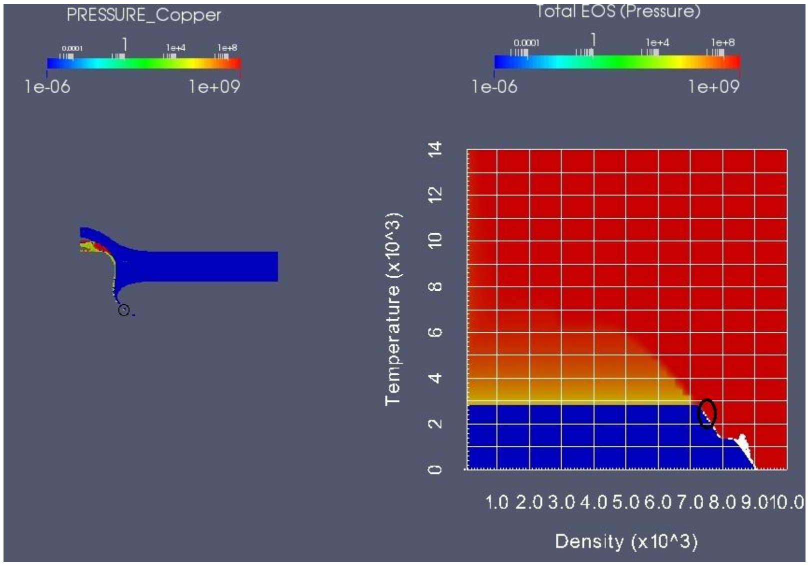

(b) force fracture

Figure A.44. Comparison: t = 3 μs

A.4 Conclusions and Recommendations

An investigation of the observed cloud formation of Ti6Al4V material in ALEGRA simulations has been performed using the 2D axisymmetric sphere impact problem. An analysis of the baseline problem, which exhibits cloud formation, was presented. A study of three algorithmic options, known to effect cloud formation, was also included. Based on the findings, several definite conclusions were reached.

The formation of clouds encountered in the sphere impact problem is a physical result that is not due to a problem with the tabular equation of state for Ti6Al4V or copper. Once a material fragment achieves a mixed liquid-vapor state and separates into a zero pressure medium (void), it will naturally expand into a gas. Although undesirable from a computational standpoint, the melting and vaporization of projectile material is perfectly reasonable given the high velocity impact condition. The occurrence of vaporization is difficult to detect experimentally for this problem, at least by radiographic means. It should be understood that any improvements made to the Ti6Al4V model will not prevent cloud formation. During the course of this study, cloud formation was observed even for the improved tabular equation of state model for copper (3325).

The use of void insertion with a minimum density threshold (force fracture option) to model mode I failure of solid materials will prevent cloud formation. Since a lower bound of density is set, the phase transition from solid to liquid-vapor will not occur, and the material will not expand into a gas. The other two options explored, prescribing an appropriate minimum density for the tabular equation of state tensile region and disallowing the use of void compression for mixed material cells, do not guarantee that cloud formation will not occur. It was observed for the use of both of these options that separated material fragments could be in a mixed liquid-vapor state which naturally leads to the formation of a cloud. Although the use of void insertion with force fracture precludes cloud formation, the user should understand that setting a lower bound for density is completely unphysical at high temperatures. Force fracture is a computational feature used to treat the failure of solid material in tension in a way that is consistent with hypoelastic material behavior.

Some issues identified during the study led to recommendations for future work to improve the general robustness of ALEGRA. Throughout the study a variety of unphysical thermodynamic state paths were exhibited by a separated fragment of mixed material simply moving through the grid. The cases include the opposing divergence of internal energies (temperatures) of the two component materials prior to cloud formation (Figures A.8 and A.9), a sudden pressure drop in one material component (Figures A.22-A.23 and A.26) and a sudden increase in pressure of one material component from a zero pressure state (Figures A.30 and A.31). All these cases evolve from a mixed-material particle for which the Ti6Al4V (or copper) component is in a mixed liquid-vapor state upon separation. For each case a static particle analysis resulted in a thermodynamic path of decreasing density and relatively constant temperature and pressure that led to cloud formation. This analysis indicates that the unphysical paths that may or may not lead to the natural result of cloud formation are completely due to the interaction of the two materials caused by the motion imparted on the particle upon separation. It is recommended that the multi-material treatment for these cases be studied more closely to determine the cause of unphysical behavior.

Unexpected behavior was observed using the KANDC tabular equation of state interpreter. As mentioned earlier, the KANDC interpreter was also used for simulation of the sphere impact problem variation that incorporated void insertion with a force fracture option, and results were nearly identical to that which utilized the KEOS interpreter. This behavior is very unexpected because the KANDC interpreter is supposed to allow density to decrease below the lower density bound imposed by the force fracture option at high temperatures in order to apply the algorithm in a more physically realistic manner. This feature did not work, and it is recommended that the interaction between the KANDC interpreter and the void insertion force fracture algorithm be investigated and modified to function as intended.

Although formation of a cloud is a physical result, the associated time step decrease remains an important issue to be addressed. The exact cause is undetermined and requires further investigation. The use of air instead of void to fill the remaining spatial domain of the problem was not addressed in this study, but should be examined. Void represents a vacuum. Allowing air to fill the void provides an ambient pressure that could preclude cloud formation and the accompanying time step decrease. In this case the user would incur an additional run time penalty.

Some recommendations arise from the analysis method used for this study and address ways to facilitate future analysis of this nature. Obtaining complete history data for the material that separates and eventually forms a cloud of vapor was problematic for the Eulerian sphere impact simulation in ALEGRA. The history data collection method described in Section A.2 provided good information but is very time consuming and tedious. The use of Lagrangian tracers to acquire history data for the material of interest proved to be unreliable for this study even when the material's physical trajectory is known after the fact. It is recommended that the use of an "advection tracer" be examined as an additional diagnostic tool in ALEGRA. The coordinates of such a tracer would be transported by the remapping algorithm used for element quantities such as density, internal energy and stress. Since the advection tracers would experience the same transport mechanism as the other element variables, it is hypothesized that these tracers would follow the material trajectory more closely than Lagrangian tracers for some problems, and ultimately provide higher quality history data.

Prism is an excellent tool for visualizing the thermodynamic state history of material in ALEGRA simulations, and this study would not have been possible without such a tool. Suggested improvements for Prism address formatting issues only. Fixing the known issue of correct logarithmic scale labeling of equation of state surfaces would be of great value for both analysis and presentation of results.

Appendix B

B.1 Time History Data Extraction Procedure for Eulerian Simulations in ALEGRA

1. Open ParaView. From the Tools menu, select manage plugins. In plugin manager window, select PrismPlugin and click “load selected” button.
2. Begin a ParaView session with an exodus (.exo) or VTK (.vtk) output file loaded into the pipeline browser and apply all desired filters and formatting to the data.
3. Load the tabular equation of state visualization file (.301) using the Prism filter.
4. Activate the appropriate simulation data to be visualized on the equation of state surface and apply all desired filters and formatting
5. Select the pane view containing the problem visualization, split the pane horizontally and select the spreadsheet view
6. In the “showing” menu, select the filter of choice, and in the “attribute” menu select cell data. Toggle the “show only selected elements button”.
7. Select the problem visualization pane. Toggle the“select cells on” button, hold left mouse button and drag cross hair over desired material selection. Data from selected cells will appear in the spreadsheet view pane and the thermodynamic state data for the selection will be highlighted in the equation of state visualization pane.
8. Correct the selection in the problem visualization pane as needed. To deselect cells, toggle the “select cells on” button, hold left mouse button and drag cross hair over area with no cells.
9. Once the desired selection is obtained, select the desired filter in the pipeline browser and apply the extract selection filter. Only the selected data will be displayed in the problem visualization pane.
10. Select save data from the file menu to save the selected cell data as a spreadsheet (.cvs file for Linux). Name the file and click ok. In the field association menu of the configure writer window, select cells and click ok.
11. Consolidate the cell data saved in a spreadsheet with previously saved data.

12. Delete the extract selection filter from the pipeline browser
13. Deselect the cell data in the problem visualization pane.
14. Advance or step back to a different configuration in time and repeat steps 7-14 until desired amount of history data has been collected.
15. Once all data has been collected it can be plotted. For this study, the data was saved in a .dat file and plotted using Matlab.

B.2 Sphere Impact Problem ALEGRA Input

```
$ vim: set syn=alegra :
$---------------------------------BEGIN_QA---------------------------------
$ ID:         sphereimpact
$ Title:      impact problem
$ Category:
$ Physics:    hydrodynamics
$ Dimension:  2D axisymmetric
$ Owner:      your name
$
$ Description:
$       Copper sphere vs. steel plate, normal impact
$
$ Materials: Ti6Al4V, with keos sesame.
$           steel, with keos sesame.
$
$ Init. Cond.:  ti alloy sphere incident on circular plate at
$                user-defined velocity
$
$ References: D.E. Grady and M.E. Kipp, Int. J. Impact.
$                Engng. 15(5): 645-660, 1994.
$ Tags:
$ CVS:
$----------------------------------END_QA----------------------------------

units, si

$ ---------------  Aprepro -----------------------

$ {_FORMAT="%.10g"}

$ mm2m:             {mm2m       = 1.00e-3}
$ CELL_SIZE:        {CELL_SIZE  = 0.15*mm2m}  $ Element dimension
$ plotint:          {plotint    = 1.e-8}      $ Time interval for plotting

$ -------------  Plate details  --------------
$ Pt1:              {Pt1        = 5.61*mm2m} $ Plate thickness (m)
$ Pd1:              {Pd1        = 75.*mm2m}  $ Plate dimension (m)
$ phi:              {phi        = 0.}        $ Plate angle wrt vertical (deg)

$ -------------  Spherical projectile  ---------------
$ Vsph:          {Vsph    = 4960.0}        $ Sphere velocity (m/s)
$ Rsph:          {Rsph    = 0.5*6.36*mm2m} $ Sphere radius (m)

$ --------------  Mesh  -----------------
$ front:            {front      = 1.5*CELL_SIZE}  $ Initial length of space ahead of plate 1 (m)
$ back:             {back       = 50.*mm2m}       $ Initial length of space behind sph (m)
$ dz:               {dz         = 25*mm2m}        $ Gap separating back of plate & mesh edge (m)
$ rsize:            {rsize      = 1.5*Pd1/2.}     $ Lateral extent of mesh (m)
$ zsize:            {zsize      = back+2.*Rsph+front+Pt1+dz} $ z extent of mesh (m)
$ Nz:               {Nz         = int(zsize/CELL_SIZE)}
$ Nr:               {Nr         = int(rsize/CELL_SIZE)}
$ NUM_CELLS:        {NUM_CELLS  = Nr*Nz}
$ a:                {a          = 0.00525}
$ b:                {b          = -0.00150657}

$ ---------------------------------------

title: Spherical projectile vs slab

termination time, 15.0e-6

$ --- PHYSICS ---

hydrodynamics
```

```
cylindrical

$ --- MESH ---
mesh, inline
  rectilinear
    bx = 1
    by = 1
    nx = {Nr}
    ny = {Nz}
    gmin = 0.0 {-front-2.*Rsph-back}
    gmax = { rsize} { Pt1+dz }
  end
  set assign
    nodeset,ilo,30
    nodeset,ihi,10
    nodeset,jlo,40
    nodeset,jhi,20
    sideset,ilo,30
    sideset,ihi,10
    sideset,jlo,40
    sideset,jhi,20
  end
end

$ --- Q ---
pronto artificial viscosity
  hyperviscosity = 1.0
  limiter = on
  linear 1.0
  quadratic 1.0
  expansion linear = on
end

$ --- BC's ---
no displacement, nodeset 30, r


block 1
  eulerian mesh
  add diatom input
end

$ --- MATERIAL INSERTION ---
diatom

  package 'SPHERE'
    material 1
    mvelocity 0. {Vsph}
    insert sphere
      center      0.0   {-front-Rsph}
      radius     {Rsph}
    endi
  endp

   package 'PLATE 1'
     material 2
     insert box
       p1 0.0        0.0
       p2 { Pd1/2.} {Pt1}
     endi
   endp

enddiatom

tracer points

  lagrangian tracer 1 r {a + CELL_SIZE/6}    z {b + CELL_SIZE/6}
  lagrangian tracer 2 r {a + CELL_SIZE/2}    z {b + CELL_SIZE/6}
```

```
lagrangian tracer 3 r {a + CELL_SIZE*5/6}  z {b + CELL_SIZE/6}
lagrangian tracer 4 r {a + CELL_SIZE/6}    z {b + CELL_SIZE/2}
lagrangian tracer 5 r {a + CELL_SIZE/2}    z {b + CELL_SIZE/2}
lagrangian tracer 6 r {a + CELL_SIZE*5/6}  z {b + CELL_SIZE/2}
lagrangian tracer 7 r {a + CELL_SIZE/6}    z {b + CELL_SIZE*5/6}
lagrangian tracer 8 r {a + CELL_SIZE/2}    z {b + CELL_SIZE*5/6}
lagrangian tracer 9 r {a + CELL_SIZE*5/6}  z {b + CELL_SIZE*5/6}

lagrangian tracer 10 r {a + CELL_SIZE*(1+1/6)}    z {b + CELL_SIZE/6}
lagrangian tracer 11 r {a + CELL_SIZE*(1+1/2)}    z {b + CELL_SIZE/6}
lagrangian tracer 12 r {a + CELL_SIZE*(1+5/6)}    z {b + CELL_SIZE/6}
lagrangian tracer 13 r {a + CELL_SIZE*(1+1/6)}    z {b + CELL_SIZE/2}
lagrangian tracer 14 r {a + CELL_SIZE*(1+1/2)}    z {b + CELL_SIZE/2}
lagrangian tracer 15 r {a + CELL_SIZE*(1+5/6)}    z {b + CELL_SIZE/2}
lagrangian tracer 16 r {a + CELL_SIZE*(1+1/6)}    z {b + CELL_SIZE*5/6}
lagrangian tracer 17 r {a + CELL_SIZE*(1+1/2)}    z {b + CELL_SIZE*5/6}
lagrangian tracer 18 r {a + CELL_SIZE*(1+5/6)}    z {b + CELL_SIZE*5/6}

lagrangian tracer 19 r {a + CELL_SIZE*(2+1/6)}    z {b + CELL_SIZE/6}
lagrangian tracer 20 r {a + CELL_SIZE*(2+1/2)}    z {b + CELL_SIZE/6}
lagrangian tracer 21 r {a + CELL_SIZE*(2+5/6)}    z {b + CELL_SIZE/6}
lagrangian tracer 22 r {a + CELL_SIZE*(2+1/6)}    z {b + CELL_SIZE/2}
lagrangian tracer 23 r {a + CELL_SIZE*(2+1/2)}    z {b + CELL_SIZE/2}
lagrangian tracer 24 r {a + CELL_SIZE*(2+5/6)}    z {b + CELL_SIZE/2}
lagrangian tracer 25 r {a + CELL_SIZE*(2+1/6)}    z {b + CELL_SIZE*5/6}
lagrangian tracer 26 r {a + CELL_SIZE*(2+1/2)}    z {b + CELL_SIZE*5/6}
lagrangian tracer 27 r {a + CELL_SIZE*(2+5/6)}    z {b + CELL_SIZE*5/6}

lagrangian tracer 28 r {a + CELL_SIZE/6}    z {b + CELL_SIZE*(1+1/6)}
lagrangian tracer 29 r {a + CELL_SIZE/2}    z {b + CELL_SIZE*(1+1/6)}
lagrangian tracer 30 r {a + CELL_SIZE*5/6}  z {b + CELL_SIZE*(1+1/6)}
lagrangian tracer 31 r {a + CELL_SIZE/6}    z {b + CELL_SIZE*(1+1/2)}
lagrangian tracer 32 r {a + CELL_SIZE/2}    z {b + CELL_SIZE*(1+1/2)}
lagrangian tracer 33 r {a + CELL_SIZE*5/6}  z {b + CELL_SIZE*(1+1/2)}
lagrangian tracer 34 r {a + CELL_SIZE/6}    z {b + CELL_SIZE*(1+5/6)}
lagrangian tracer 35 r {a + CELL_SIZE/2}    z {b + CELL_SIZE*(1+5/6)}
lagrangian tracer 36 r {a + CELL_SIZE*5/6}  z {b + CELL_SIZE*(1+5/6)}

lagrangian tracer 37 r {a + CELL_SIZE*(1+1/6)}    z {b + CELL_SIZE*(1+1/6)}
lagrangian tracer 38 r {a + CELL_SIZE*(1+1/2)}    z {b + CELL_SIZE*(1+1/6)}
lagrangian tracer 39 r {a + CELL_SIZE*(1+5/6)}    z {b + CELL_SIZE*(1+1/6)}
lagrangian tracer 40 r {a + CELL_SIZE*(1+1/6)}    z {b + CELL_SIZE*(1+1/2)}
lagrangian tracer 41 r {a + CELL_SIZE*(1+1/2)}    z {b + CELL_SIZE*(1+1/2)}
lagrangian tracer 42 r {a + CELL_SIZE*(1+5/6)}    z {b + CELL_SIZE*(1+1/2)}
lagrangian tracer 43 r {a + CELL_SIZE*(1+1/6)}    z {b + CELL_SIZE*(1+5/6)}
lagrangian tracer 44 r {a + CELL_SIZE*(1+1/2)}    z {b + CELL_SIZE*(1+5/6)}
lagrangian tracer 45 r {a + CELL_SIZE*(1+5/6)}    z {b + CELL_SIZE*(1+5/6)}

lagrangian tracer 46 r {a + CELL_SIZE*(2+1/6)}    z {b + CELL_SIZE*(1+1/6)}
lagrangian tracer 47 r {a + CELL_SIZE*(2+1/2)}    z {b + CELL_SIZE*(1+1/6)}
lagrangian tracer 48 r {a + CELL_SIZE*(2+5/6)}    z {b + CELL_SIZE*(1+1/6)}
lagrangian tracer 49 r {a + CELL_SIZE*(2+1/6)}    z {b + CELL_SIZE*(1+1/2)}
lagrangian tracer 50 r {a + CELL_SIZE*(2+1/2)}    z {b + CELL_SIZE*(1+1/2)}
lagrangian tracer 51 r {a + CELL_SIZE*(2+5/6)}    z {b + CELL_SIZE*(1+1/2)}
lagrangian tracer 52 r {a + CELL_SIZE*(2+1/6)}    z {b + CELL_SIZE*(1+5/6)}
lagrangian tracer 53 r {a + CELL_SIZE*(2+1/2)}    z {b + CELL_SIZE*(1+5/6)}
lagrangian tracer 54 r {a + CELL_SIZE*(2+5/6)}    z {b + CELL_SIZE*(1+5/6)}

lagrangian tracer 55 r {a + CELL_SIZE/6}    z {b + CELL_SIZE*(2+1/6)}
lagrangian tracer 56 r {a + CELL_SIZE/2}    z {b + CELL_SIZE*(2+1/6)}
lagrangian tracer 57 r {a + CELL_SIZE*5/6}  z {b + CELL_SIZE*(2+1/6)}
lagrangian tracer 58 r {a + CELL_SIZE/6}    z {b + CELL_SIZE*(2+1/2)}
lagrangian tracer 59 r {a + CELL_SIZE/2}    z {b + CELL_SIZE*(2+1/2)}
lagrangian tracer 60 r {a + CELL_SIZE*5/6}  z {b + CELL_SIZE*(2+1/2)}
lagrangian tracer 61 r {a + CELL_SIZE/6}    z {b + CELL_SIZE*(2+5/6)}
lagrangian tracer 62 r {a + CELL_SIZE/2}    z {b + CELL_SIZE*(2+5/6)}
lagrangian tracer 63 r {a + CELL_SIZE*5/6}  z {b + CELL_SIZE*(2+5/6)}
```

```
    lagrangian tracer 64 r {a + CELL_SIZE*(1+1/6)}    z {b + CELL_SIZE*(2+1/6)}
    lagrangian tracer 65 r {a + CELL_SIZE*(1+1/2)}    z {b + CELL_SIZE*(2+1/6)}
    lagrangian tracer 66 r {a + CELL_SIZE*(1+5/6)}    z {b + CELL_SIZE*(2+1/6)}
    lagrangian tracer 67 r {a + CELL_SIZE*(1+1/6)}    z {b + CELL_SIZE*(2+1/2)}
    lagrangian tracer 68 r {a + CELL_SIZE*(1+1/2)}    z {b + CELL_SIZE*(2+1/2)}
    lagrangian tracer 69 r {a + CELL_SIZE*(1+5/6)}    z {b + CELL_SIZE*(2+1/2)}
    lagrangian tracer 70 r {a + CELL_SIZE*(1+1/6)}    z {b + CELL_SIZE*(2+5/6)}
    lagrangian tracer 71 r {a + CELL_SIZE*(1+1/2)}    z {b + CELL_SIZE*(2+5/6)}
    lagrangian tracer 72 r {a + CELL_SIZE*(1+5/6)}    z {b + CELL_SIZE*(2+5/6)}

    lagrangian tracer 73 r {a + CELL_SIZE*(2+1/6)}    z {b + CELL_SIZE*(2+1/6)}
    lagrangian tracer 74 r {a + CELL_SIZE*(2+1/2)}    z {b + CELL_SIZE*(2+1/6)}
    lagrangian tracer 75 r {a + CELL_SIZE*(2+5/6)}    z {b + CELL_SIZE*(2+1/6)}
    lagrangian tracer 76 r {a + CELL_SIZE*(2+1/6)}    z {b + CELL_SIZE*(2+1/2)}
    lagrangian tracer 77 r {a + CELL_SIZE*(2+1/2)}    z {b + CELL_SIZE*(2+1/2)}
    lagrangian tracer 78 r {a + CELL_SIZE*(2+5/6)}    z {b + CELL_SIZE*(2+1/2)}
    lagrangian tracer 79 r {a + CELL_SIZE*(2+1/6)}    z {b + CELL_SIZE*(2+5/6)}
    lagrangian tracer 80 r {a + CELL_SIZE*(2+1/2)}    z {b + CELL_SIZE*(2+5/6)}
    lagrangian tracer 81 r {a + CELL_SIZE*(2+5/6)}    z {b + CELL_SIZE*(2+5/6)}

  end

  plot, exotracer
    file = 'tracer.exo'
  end

  plot, sesame file
    filename="Ti6Al4V.ses"
    extra variable, "DPDRHO"
    extra variable, "SOUND_SPEED"
    material=1
    temperature bounds
      linear  0.0 [K] to 14000 [K] by 1000
    end
    density bounds
      linear  60 [kg/m^3] to 6000 [kg/m^3] by 1000
    end
  end

  plot, sesame file
    filename="4340Steel.ses"
    extra variable, "DPDRHO"
    extra variable, "SOUND_SPEED"
    material=2
    temperature bounds
      linear  0.0 [K] to 14000 [K] by 1000
    end
    density bounds
      linear  60 [kg/m^3] to 10000 [kg/m^3] by 1000
    end
  end

end

$--- PLOTTING ---
emit plot, time interval={plotint}
emit plot, exact time interval=11.6e-6
emit hisplt, cycle interval=5
emit screen, cycle interval=1

plot variables
  velocity
  density
  temperature
  pressure
  energy
  density: avg
  temperature: avg
```

```
  pressure: avg
  energy: avg
  volfrac_beta
  sound speed
  dpdrho
  vorticity
  div_v
end

spy
  variable SPY_COUNT;
  SPY_COUNT = 0;
  define EndImage (VALUE_IN) \{
    if (IN_IMAGE == FALSE) \{
      spy_error("\n\nEndImage command encountered when expecting Image\n\n");
      return;
    \}
    IN_IMAGE = FALSE;
    if (getNeedToRestore() > 0) \{
      restore_spy_file();
    \}
    variable TMP_NAME=IMAGE_NAME+sprintf("%06d",VALUE_IN);
    pop_matrix();
    render_image(OUTPUT_TYPE, TMP_NAME);
  \}

  PlotTime(0,1.e-6);
  XLimits({-rsize},{rsize});
  ImageFormat(640,480);
  define main ()
    \{
    pprintf(" PLOT: Cycle=%d, Time=%e\n",CYCLE,TIME);
    Image("SphereImpact",WHITE,BLACK);
      SMOOTH_SHADING=OFF;
      Label(sprintf("Materials and DENSITY at %6.2e seconds",TIME));
      ULabel("r (m)");
      VLabel("z (m)");
      XBMirror(ON);
      MatColors(BLUE,ORANGE);
      Plot2DMats(0.3);
      XBMirror(OFF);
      HotMap;
      ColorMapRange(1.e-3,1.e4,LOG_MAP);
      DrawColorMap("DENSITY (kg/m^3^)",0.05,0.3,0.2,0.8);
      Plot2D("DENSITY");
     %DrawTracers(2);
    EndImage(SPY_COUNT);
    SPY_COUNT = SPY_COUNT + 1;
  \}
endspy


$ --- MATERIAL DEFINITIONS ---

$ - Ti6Al4V -

material 1 ’Ti6Al4V sphere’
  model = 102
  Density = 4418.00382
  Temperature = 298.0
end

model 102 keos sesame
  neos = 4061
end

$ - STEEL -
```

```
material 2 'Steel Plate'
  model 202
  density = 7872.37978
  Temperature = 298
end

model 202 keos sesame
  matlabel = 'STEEL_4340'
end


exit
```

References

[1] The RSPt code. See http://fplmto-rspt.org.

[2] Rajeev Ahuja, John M. Wills, Börje Johansson, and Olle Eriksson. Crystal structures of Ti, Zr, and Hf under compression: Theory. *Phys. Rev. B*, 48:16269–16279, Dec 1993.

[3] Yuichi Akahama, Haruki Kawamura, and Tristan Le Bihan. New δ (distorted-bcc) titanium to 220 GPa. *Phys. Rev. Lett.*, 87:275503, Dec 2001.

[4] P. Andriot, P. Lalle, and J. P. Dejean. Quasielastic behavior of pure titanium and TA6V4 titanium alloy at high pressure. *AIP Conference Proceedings*, 309(1):1009–1012, 1994.

[5] P. E. Blöchl. Projector augmented-wave method. *Phys. Rev .B*, 50:17953, 1994.

[6] N.K. Bourne, J.C.F. Millett, and III Gray, G.T. On the shock compression of polycrystalline metals. *Journal of Materials Science*, 44(13):3319–3343, 2009.

[7] E. Cerreta, G. T. Gray, III, A. C. Lawson, T. A. Mason, and C. E. Morris. The influence of oxygen content on the alpha to omega phase transformation and shock hardening of titanium. *Journal of Applied Physics*, 100(1):013530, 2006.

[8] Gary N. Chesnut, Nenad Velisavljevic, and Lilliana Sanchez. Static high pressure x-ray diffraction of Ti-6Al-4V. *AIP Conference Proceedings*, 955(1):27–30, 2007.

[9] Geoffrey Cox. An equation of state for titanium. *Journal of Physics: Conference Series*, 286(1):012043, 2011. A poster is available as supplementary data at `http://stacks.iop.org/1742-6596/286/1/012043`.

[10] Geoffrey Cox. An equation of state for Ti-6Al-4V. *AIP Conference Proceedings*, 1426(1):1559–1562, 2012.

[11] Dattatraya P. Dandekar and Stephen V. Spletzer. Shock response of Ti-6Al-4V. *AIP Conference Proceedings*, 505(1):427–430, 2000.

[12] Daniel Errandonea, Y. Meng, M. Somayazulu, and D. Husermann. Pressure-induced transition in titanium metal: a systematic study of the effects of uniaxial stress. *Physica B: Condensed Matter*, 355(14):116 – 125, 2005.

[13] Daniel Errandonea, Beate Schwager, Reiner Ditz, Christine Gessmann, Reinhard Boehler, and Marvin Ross. Systematics of transition-metal melting. *Phys. Rev. B*, 63:132104, Mar 2001.

[14] D.E. Grady and M.E. Kipp. Experimental and computational simulation of the high velocity impact of copper spheres on steel plates. *International Journal of Impact Engineering*, 15(5):645 – 660, 1994.

[15] C. W. Greeff, D. R. Trinkle, and R. C. Albers. Shock-induced alpha–omega transition in titanium. *Journal of Applied Physics*, 90(5):2221–2226, 2001.

[16] I Halevy, G Zamir, M Winterrose, G Sanjit, Carlos Roberto Grandini, and Ariel Moreno-Gobbi. Crystallographic structure of Ti-6Al-4V, Ti-HP and Ti-CP under high-pressure. *Journal of Physics: Conference Series*, 215(1):012013, 2010.

[17] Yan-Jun Hao, Lin Zhang, Xiang-Rong Chen, Ying-Hua Li, and Hong-Liang He. First-principles phase transition and equation of state of titanium. *Solid State Communications*, 146(34):105 – 109, 2008.

[18] F.H. Hayes. The Al-Ti-V (aluminum-titanium-vanadium) system. *Journal of Phase Equilibria*, 16(2):163–176, 1995.

[19] R. G. Hennig, T. J. Lenosky, D. R. Trinkle, S. P. Rudin, and J. W. Wilkins. Classical potential describes martensitic phase transformations between the α, β, and ω titanium phases. *Phys. Rev. B*, 78:054121, Aug 2008.

[20] P. Hohenberg and W. Kohn. Inhomogeneous electron gas. *Phys. Rev.*, 136:B864–B871, Nov 1964.

[21] Cui-E Hu, Zhao-Yi Zeng, Lin Zhang, Xiang-Rong Chen, Ling-Cang Cai, and Dario Alfe. Theoretical investigation of the high pressure structure, lattice dynamics, phase transition, and thermal equation of state of titanium metal. *Journal of Applied Physics*, 107(9):093509, 2010.

[22] S. Kar, T. Searles, E. Lee, G.B. Viswanathan, H.L. Fraser, J. Tiley, and R. Banerjee. Modeling the tensile properties in β-processed α/β Ti alloys. *Metallurgical and Materials Transactions A*, 37(3):559–566, 2006.

[23] Gerald I. Kerley. Equations of state for titanium and Ti6A14V alloy. Technical report SAND2003-3785, Sandia National Laboratories, Albuquerque, New Mexico 87185 and Livermore, California 94550, October 2003.

[24] W. Kohn and L. J. Sham. Self-consistent equations including exchange and correlation effects. *Phys. Rev.*, 140:A1133–A1138, Nov 1965.

[25] G. Kresse and J. Furthmüller. Efficient iterative schemes for ab initio total-energy calculations using a plane-wave basis set. *Phys. Rev. B*, 54:11169, 1996.

[26] G. Kresse and J. Hafner. Ab initio molecular dynamics for liquid metals. *Phys. Rev. B*, 47:R558, 1993.

[27] G. Kresse and J. Hafner. Ab initio molecular-dynamics simulation of the liquid-metal-amorphous-semiconductor transition in germanium. *Phys. Rev. B*, 49:14251, 1994.

[28] G. Kresse and D. Joubert. From ultrasoft pseudopotentials to the projector augmented-wave method. *Phys. Rev. B*, 59:1758, 1999.

[29] A. L. Kutepov and S. G. Kutepova. Crystal structures of ti under high pressure: Theory. *Phys. Rev. B*, 67:132102, Apr 2003.

[30] Woei-Shyan Lee and Chi-Feng Lin. High-temperature deformation behaviour of Ti6Al4V alloy evaluated by high strain-rate compression tests. *Journal of Materials Processing Technology*, 75(13):127 – 136, 1998.

[31] Woei-Shyan Lee and Chi-Feng Lin. Plastic deformation and fracture behaviour of Ti-6Al-4V alloy loaded with high strain rate under various temperatures. *Materials Science and Engineering: A*, 241(12):48 – 59, 1998.

[32] Stanford P. Lyon and James D. Johnson. Sesame: the Los Alamos National Laboratory equation of state database. Technical report LA-UR-92-3407, Los Alamos National Laboratory, Los Alamos, NM 87545, 1992.

[33] S. G. MacLeod, B. E. Tegner, H. Cynn, W. J. Evans, J. E. Proctor, M. I. McMahon, and G. J. Ackland. Experimental and theoretical study of Ti-6Al-4V to 220 GPa. *Phys. Rev. B*, 85:224202, Jun 2012.

[34] A Majorell, S Srivatsa, and R.C Picu. Mechanical behavior of Ti-6Al-4V at high and moderate temperatures – Part I: Experimental results. *Materials Science and Engineering: A*, 326(2):297 – 305, 2002.

[35] Ann E. Mattsson. In pursuit of the "divine" functional. *Science*, 298(5594):759–760, 2002.

[36] Zhi-Gang Mei, Shun-Li Shang, Yi Wang, and Zi-Kui Liu. Density-functional study of the thermodynamic properties and the pressure-temperature phase diagram of Ti. *Phys. Rev. B*, 80:104116, Sep 2009.

[37] Yuri I. Mescheryako and Alexandre K. Divakov. Affect of shock-induced phase transformations on dynamic strength of titanium alloys. *International Journal of Impact Engineering*, 26(110):497 – 508, 2001.

[38] J. C. F. Millett, G. Whiteman, N. K. Bourne, G. T. Gray, and III. The role of anisotropy in the response of the titanium alloy Ti-6Al-4V to shock loading. *Journal of Applied Physics*, 104(7):073531, 2008.

[39] C.E. Morris, M.A. Winkler, and A.C. Mitchell. Ti-6%Al-4%V alloy wave profile measurements in the shadow region. In S.C. Schmidt and N.C. Holmes, editors, *Shock Waves in Condensed Matter - 1987*, pages 265–268. Elsevier, Amsterdam, 1988.

[40] Sia Nemat-Nasser, Wei-Guo Guo, Vitali F. Nesterenko, S.S. Indrakanti, and Ya-Bei Gu. Dynamic response of conventional and hot isostatically pressed Ti-6Al-4V alloys: experiments and modeling. *Mechanics of Materials*, 33(8):425 – 439, 2001.

[41] Yong Niu, Miaoquan Li, Hongliang Hou, Yaoqi Wang, and Yingying Lin. High-temperature deformation behavior of Ti-6Al-4V alloy without and with hydrogenation content of 0.27 wt.%. *Journal of Materials Engineering and Performance*, 19(1):59–63, 2010.

[42] V. Ozolins. First-principles calculations of free energies of unstable phases: The case of fcc W. *Phys. Rev. Lett.*, 102:065702, Feb 2009.

[43] S. Pecker, S. Eliezer, D. Fisher, Z. Henis, and Z. Zinamon. A multiphase equation of state of three solid phases, liquid, and gas for titanium. *Journal of Applied Physics*, 98(4):043516, 2005.

[44] R.C. Picu and A. Majorell. Mechanical behavior of Ti-6Al-4V at high and moderate temperatures–Part II: constitutive modeling. *Materials Science and Engineering: A*, 326(2):306 – 316, 2002.

[45] William D. Reinhart, Lalit C. Chhabildas, Daniel E. Carroll, Thomas K. Bergstresser, Tom F. Thornhill, and Nancy A. Winfree. Equation of state measurements of materials using a three-stage gun to impact velocities of 11 km/s. *International Journal of Impact Engineering*, 26(110):625 – 637, 2001.

[46] A. C. Robinson and *et al.* Alegra user manual. Technical report SAND2013-2194, Sandia National Laboratories (SNL), Albuquerque, NM, March 2013.

[47] Z. Rosenberg, Y. Meybar, and D. Yaziv. Measurement of the hugoniot curve of Ti-6Al-4V with commercial manganin gauges. *Journal of Physics D: Applied Physics*, 14(2):261, 1981.

[48] Songwon Seo, Oakkey Min, and Hyunmo Yang. Constitutive equation for Ti-6Al-4V at high temperatures measured using the SHPB technique. *International Journal of Impact Engineering*, 31(6):735 – 754, 2005.

[49] S.K. Sikka, Y.K. Vohra, and R. Chidambaram. Omega phase in materials. *Progress in Materials Science*, 27(34):245 – 310, 1982.

[50] B. E. Tegner, S. G. Macleod, H. CYNN, J. Proctor, W. J. Evans, M. I. McMahon, and G. J. Ackland. An experimental and theoretical multi-mbar study of Ti-6Al-4V. Technical report LLNL-PROC-481057, Lawrence Livermore National Laboratory (LLNL), Livermore, CA, April 2011.

[51] Bengt E. Tegner, Simon G. MacLeod, Hyunchae Cynn, John Proctor, William J. Evans, Malcolm I. McMahon, and Graeme J. Ackland. An experimental and theoretical multi-mbar study of Ti-6Al-4V. *MRS Proceedings*, 1369, 1 2011.

[52] Nenad Velisavljevic, Simon MacLeod, and Hyunchae Cynn. Titanium alloys at extreme pressure conditions. In A.K.M. Nurul Amin, editor, *Titanium Alloys - Towards Achieving Enhanced Properties for Diversified Applications*. InTech, March

2012. Available from: http://www.intechopen.com/books/titanium-alloys-towards-achieving-enhanced-properties-for-diversified-applications/titanium-alloys-at-extreme-pressure-conditions.

[53] A. K. Verma, P. Modak, R. S. Rao, B. K. Godwal, and R. Jeanloz. High-pressure phases of titanium: First-principles calculations. *Phys. Rev. B*, 75:014109, Jan 2007.

[54] Yogesh K. Vohra and Philemon T. Spencer. Novel γ-phase of titanium metal at megabar pressures. *Phys. Rev. Lett.*, 86:3068–3071, Apr 2001.

[55] J. M. Wills, O. Eriksson, M. Alouani, and D. L. Price. Full potential LMTO: Total energy and force calculations. In H. Dreysse, editor, *Electronic Structure and Physical Properties of Solids: The Uses of the LMTO Method*, volume 535 of *Lecture Notes in Physics*. Springer-Verlag, Berlin, 2000.

[56] N. A. Winfree, L. C. Chhabildas, W. D. Reinhart, D. E. Carroll, and G. I. Kerley. EOS data of Ti-6Al-4V to impact velocities of 10.4 km/s on a three-stage gun. *AIP Conference Proceedings*, 620(1):75–78, 2002.

[57] Jianzhong Zhang, Yusheng Zhao, Robert S. Hixson, George T. Gray, Liping Wang, Wataru Utsumi, Saito Hiroyuki, and Hattori Takanori. Thermal equations of state for titanium obtained by high pressure-temperature diffraction studies. *Phys. Rev. B*, 78:054119, Aug 2008.

[58] Jianzhong Zhang, Yusheng Zhao, Robert S. Hixson, George T. Gray III, Liping Wang, Wataru Utsumi, Saito Hiroyuki, and Hattori Takanori. Experimental constraints on the phase diagram of titanium metal. *Journal of Physics and Chemistry of Solids*, 69(10):2559 – 2563, 2008.

[59] Sergey Zherebtsov, Gennady Salishchev, Rafail Galeyev, and Katsuhiro Maekawa. Mechanical properties of Ti-6Al-4V titanium alloy with submicrocrystalline structure produced by severe plastic deformation. *Materials Transactions*, 46(9):2020–2025, 2005.

DISTRIBUTION:

1 R. B. Leavy
U.S. Army Research Laboratory
ATTN: RDRL-WMP-C
Aberdeen Proving Grounds, MD 21005
(electronic copy)

1 R. L. Doney
U.S. Army Research Laboratory
ATTN: RDRL-WMP-D
Aberdeen Proving Grounds, MD 21005
(electronic copy)

1 A. J. Porwitzky
U.S. Army Research Laboratory
ATTN: RDRL-WMP-A
Aberdeen Proving Grounds, MD 21005
(electronic copy)

1 J. R. Houskamp
U.S. Army Research Laboratory
ATTN: RDRL-WMP-D
Aberdeen Proving Grounds, MD 21005
(electronic copy)

1 M. J. Coppinger
U.S. Army Research Laboratory
ATTN: RDRL-WMP-A
Aberdeen Proving Grounds, MD 21005
(electronic copy)

1	MS 1320	Scott S. Collis, 01440 (electronic copy)
1	MS 1321	Glen Hansen, 01443 (electronic copy)
1	MS 1321	Veena Tikare, 01444 (electronic copy)
1	MS 1321	Randall M. Summers, 01446 (electronic copy)
1	MS 1322	Ann E. Mattsson, 01444 (electronic copy)
1	MS 1323	Erik O. Strack, 01220 (electronic copy)
1	MS 1323	Sharon Petney, 01443 (electronic copy)
1	MS 1323	Jason Sanchez, 01443 (electronic copy)
1	MS 1323	John Niederhaus, 01446 (electronic copy)
1	MS 0899	Technical Library, 9536 (electronic copy)

Sandia National Laboratories